

---

# Site U1339<sup>1</sup>

---

Expedition 323 Scientists<sup>2</sup>

## Chapter contents

Background and objectives	1
Operations	2
Lithostratigraphy	3
Biostratigraphy	5
Paleomagnetism	9
Geochemistry and microbiology	10
Physical properties	11
Stratigraphic correlation	13
Downhole measurements	14
References	15
Figures	18
Tables	58

## Background and objectives

The primary objective of drilling at Integrated Ocean Drilling Program (IODP) Site U1339 (proposed Site UMK-4D; Takahashi et al., 2009) was to study high-resolution paleoceanography in the easternmost part of the Bering Sea, a marginal sea expected to exhibit large variations during times of global climate change. Umnak Plateau is located off Bristol Bay (Figs. F1, F2, F3) and is well situated to study past changes in surface water conditions (Fig. F4), sea ice extent, and associated biological productivity. Today, parts of the relatively warm Alaskan Stream surface water flow into the Bering Sea through Umnak and Amukta passes, and hence sea ice is not formed in this region. However, substantial sea ice coverage during the Last Glacial Maximum (LGM), when sea level was ~100 m lower than today, has been noted. This indicates that the influence of relatively warm water from the distal end of the Alaskan Stream was reduced, perhaps because water entering the Bering Sea from the Pacific Ocean through Umnak and Amukta passes was at least partially restricted when sea level dropped; warm Pacific water could have more easily passed through deeper passes, such as Amchitka Strait, in the central and western Aleutians (Katsuki and Takahashi, 2005). Thus, examining past environmental conditions at Umnak Plateau can shed light on the impact of changes in water exchange between the Pacific Ocean and the Bering Sea. Because these eastern passes are fairly shallow (~50 and 430 m), little intermediate or deep water flows out to the Pacific in this region. As such, Umnak Plateau should provide different information than the western sites, which are closer to deep passes where surface water flow may not have been strongly inhibited by sea level changes and where dense water exchange with the Pacific Ocean is more likely to occur (Tanaka and Takahashi, 2005). To make this west–east comparison, records from Site U1339 (water depth = 1870 m) on Umnak Plateau can be compared to those of IODP Site U1341 (water depth = 2177 m).

Site U1339 can also be used to study the impact of seafloor microbes on biogeochemical fluxes in the highest surface-ocean productivity areas of the drill sites in the Bering Sea. Organic-fueled seafloor respiration and its impact on biogeochemistry in such a highly productive region have not previously been quantified. To do this, sediments drilled at Umnak Plateau were used to determine seafloor cell abundances and investigate the link between the mass and characteristics of seafloor microbes and

<sup>1</sup>Expedition 323 Scientists, 2011. Site U1339. In Takahashi, K., Ravelo, A.C., Alvarez Zarikian, C.A., and the Expedition 323 Scientists, *Proc. IODP, 323*: Tokyo (Integrated Ocean Drilling Program Management International, Inc.).  
doi:10.2204/iodp.proc.323.103.2011

<sup>2</sup>Expedition 323 Scientists' addresses.



the extent of export productivity from the surface ocean.

Scholl and Creager (1973) found Pleistocene diatomaceous sediments with ash layers in the uppermost 120 m, followed by Pliocene diatomaceous sediments below, at Deep Sea Drilling Project (DSDP) Sites 184 and 185, both drilled at Umnak Plateau. They reported sedimentation rates of ~67 m/m.y. and indicated that the diatomaceous sediments include neritic components, which are probably an influence from the Bristol Bay region. A piston core study from the same general region provided a sedimentation rate of 262 m/m.y. (Takahashi, 2005). Thus, before drilling, the predicted ages for the bottom of Site U1339 at ~200 meters below seafloor (mbsf) ranged from mid-Pleistocene to Pliocene.

## Operations

We arrived at Site U1339 early on 16 July 2009 after a 6.5 day, 1782 nmi transit from Victoria, British Columbia, Canada, and operations officially began. The coring summary for this site is provided in Table T1.

One relatively shallow and three relatively deep holes were drilled and cored using the advanced piston corer (APC) at a water depth of 1867 m on Umnak Plateau: Hole U1339A (33.4 m drilling depth below seafloor [DSF]), Hole U1339B (196.0 m DSF), Hole U1339C (194.8 m DSF), and Hole U1339D (200.0 m DSF). Cores 323-U1339B-1H through 4H were primarily used for subseafloor microbial study, and both perfluorocarbon tracer (PFT) and whirlpack bags containing fluorescent microbeads were deployed. The remaining cores were used for paleoceanographic studies. Most cores had nearly 100% or greater recovery because of gas expansion. The exceptions are two short cores (323-U1339B-13H [2 m] and 323-U1339C-16H [4.5 m]) that were recovered when the APC fired into unknown objects, most likely glacial dropstones.

### Hole U1339A

Hole U1339A was spudded at 0430 h on 17 July (all times are ship local time, Universal Time Coordinated [UTC] – 11 h). The first core was shot with the bit at 1873 m drilling depth below rig floor (DRF), recovering the mudline and 4.94 m of core. The hole was terminated after Core 323-U1339A-4H when a suspected bottom-hole assembly (BHA)/coring system problem resulted in almost 100,000 lb of overpull on the last core. The drill string was tripped out of the hole, the coring system components were inspected, and several parts were changed. No conclu-

sive evidence of the mechanical problem was found. The BHA was run, and the coring system was tested successfully in the water column.

### Hole U1339B

The vessel was offset 20 m, the rest of the string was tripped to the seafloor, and Hole U1339B was spudded at 2315 h on 17 July. The first four cores (323-U1339B-1H through 4H) were dedicated to microbiology, and both PFT and whirlpack bags were deployed. Coring in Hole U1339B recovered the sedimentary sequence from the total depth of Hole U1339A to 196.0 m DSF. One short core (323-U1339B-13H) was recovered when the APC fired into an unknown object, most likely a glacial dropstone. The nonmagnetic core barrel was replaced with a steel core barrel when resistance became exceedingly high in Core 323-U1339B-19H. Hole U1339B was cored to 196.0 m DSF, and coring ended at 2010 h on 18 July when the bit cleared the seafloor.

### Hole U1339C

The vessel was offset 28 m, and Hole U1339C was spudded at 2230 h on 18 July. The first core was >9.5 m long but contained the mudline at its top. Core advance was a continuous 9.5 m except for Core 323-U1339C-16H, which contacted an apparent dropstone at 4.5 m. The nonmagnetic core barrel was used through Core 323-U1339C-17H, and APC coring proceeded with a steel core barrel through Core 323-U1339C-21H to 194.8 m DSF. The drill string cleared the seafloor at 1610 h on 19 July, officially ending Hole U1339C.

### Hole U1339D

The vessel was offset 28.3 m, and Hole U1339D was spudded at 1724 h on 19 July. Core 323-U1339D-1H was 6.6 m long. All successive cores were 9.5 m long, with the exception of one short core that resulted from premature firing of the APC. The nonmagnetic core barrel was used through Core 323-U1339D-17H, and APC coring proceeded with a steel core barrel through Core 323-U1339D-22H to 200.0 m DSF. Rig-up for wireline logging in Hole U1339D started at 1130 h on 20 July. The triple combination (triple combo) and Formation MicroScanner (FMS)-sonic tool strings were deployed, and both obtained good data. The drill string was pulled and secured for transit. Transit to IODP Site U1340 began at 0745 h on 21 July.

In all, APC coring for Site U1339 totaled 69 cores, 642.2 m penetrated, and 644.75 m recovered, for 103.1% core recovery.

## Lithostratigraphy

Four holes were drilled at Site U1339, with the deepest (Hole U1339D) reaching 200 mbsf. Overall, the sediments recovered at Site U1339 are a mixture of three components: biogenic (mainly diatom frustules with varying proportions of nannofossils, foraminifers, silicoflagellates, and radiolarians), volcanoclastic (mainly fine ash), and siliciclastic (clay- to pebble-sized clasts). Other accessory lithologies identified at this site include authigenic carbonate and pyrite. In general, the color of the sediment reflects its lithologic characteristics: sediment composed of mixed lithologies (diatom silt or diatom ashy silt) is dark greenish gray, whereas diatom ooze is olive-gray to olive. Most of the volcanoclastic ash layers are black, although a few massive light gray ash layers were also observed. One lithologic unit spanning the Pleistocene was defined at Site U1339 (Figs. F5, F6, F7, F8).

### Description of unit

#### Unit I

Intervals: Sections 323-U1339A-1H-1, 0 cm, through 4H-7, 80 cm; 323-U1339B-1H-1, 0 cm, through 22H-CC, 37 cm; 323-U1339C-1H-1, 0 cm, through 21H-CC, 41 cm; and 323-U1339D-1H-1, 0 cm, through 22H-CC, 38 cm

Depths: Hole U1339A, 0–33.7 mbsf; Hole U1339B, 0–196.93 mbsf; Hole U1339C, 0–195.34 mbsf; and Hole U1339D, 0–200.83 mbsf

Age: Pleistocene

Unit I is composed of mainly diatom-rich sediments mixed with varying amounts of volcanoclastic and siliciclastic material. In particular, three main types of lithologies were recognized. The first type is biogenic sediment, which is mainly diatom ooze with minor (<20%) amounts of other biogenics, including nannofossils, foraminifers, and trace (<5%) silicoflagellates and sponge spicules. The biogenics occur mixed with variable amounts (<5%–40%) of silt-sized volcanoclastic and siliciclastic material, including quartz, feldspar, clay minerals, and trace amounts of micas and zeolites. The color is usually olive-gray (5Y 4/2). The second type is sediment composed of subequal proportions of siliciclastic (silt-sized quartz, feldspar, and rock fragments and/or clay) and biogenic (mainly diatoms and secondarily nannofossils, foraminifers, silicoflagellates, and sponge spicules) material with only secondary volcanoclastic components. Depending on the proportion of siliciclastic to biogenic grains, the color varies from greenish gray (5GY 5/1) to dark greenish gray (5G 4/1 and 10Y 4/1). The third type is sediment composed of subequal proportions of volcanoclastic (mainly volcanic ash) and bio-

genic (mainly diatoms and secondarily nannofossils, foraminifers, silicoflagellates, and sponge spicules) material with only secondary siliciclastic components (see “[Site U1339 smear slides](#)” in “Core descriptions”). The color varies from very dark greenish gray (10Y 3/1) to dark gray (5Y 4/1.4). Volcanic ash layers are commonly black (5Y 2.5/1) and less commonly light gray (10Y 7/1 and 10YR 7/2).

Distinct ash layers ranging in thickness from a few millimeters to 10 cm occur throughout the unit, and layers thicker than 2 cm are reported as distinct lithologies (Figs. F5, F6, F7, F8). Several prominent volcanoclastic layers show either parallel or undulating sharp contacts with the underlying sediment. Conversely, the top boundaries are gradational and the ash is mixed with the overlying diatom ooze, most likely from bioturbation and/or diffusion. Some black ash layers are also characterized by graded bedding, with the coarser clasts concentrated at the bottom (Fig. F9B). Apart from distinct ash layers, fine volcanoclastic material is often concentrated in mottles that are likely the result of bioturbation of thin ash layers. Volcanic ash is a common secondary or trace lithologic component in most of the recovered sediments, and most volcanoclastic layers are black.

The largest scale sedimentary features at Site U1339 are decimeter- to meter-scale alternations of sediment color and texture that reflect alternations in lithology. The transitions between beds are commonly gradational, although sharp boundaries were also observed. Well-preserved laminations were primarily observed in six distinct intervals, each ranging between 10 and 40 cm in thickness (Figs. F5, F6, F7, F8). The laminations are alternations of millimeter-scale dark (mainly diatom ooze) and light (mainly nannofossil- and foraminifer-rich diatom ooze) laminae (see “[Site U1339 smear slides](#)” in “Core descriptions”). Laminated intervals always have ash layers either below or above them (Fig. F9). The thickest volcanic ash layer (~20 cm thick: interval 323-U1339B-3H-2, 108–128 cm) is overlain by ~20 cm of laminated sediment.

The major component of the sediments recovered at Site U1339 is biogenic, predominantly pennate and centric diatoms. The preservation of diatom frustules is generally good (see “[Biostratigraphy](#)”); however, in several of the smear slides, broken pennates and girdles without valves indicate dissolution. Diatom frustules hosting pyrite framboids were also observed. Calcareous tests are relatively rare because of the low preservation potential in these sediments and/or low rates of primary productivity of marine organisms producing carbonate tests. Both benthic and planktonic foraminifers are present; however,

they are never abundant, possibly because smear slides selectively sample smaller grain sizes (see “[Lithostratigraphy](#)” in the “[Methods](#)” chapter). Thin laminae dominated by foraminifer tests were also observed (always <20%; see “[Site U1339 smear slides](#)” in “[Core descriptions](#)”). These laminae are dominated by the benthic foraminifer *Bulimina* sp. Calcareous nannofossils, radiolarians, and sponge spicules are rare.

Terrigenous particles are common in the sediments recovered at Site U1339. The most abundant terrigenous grain types are silt-sized quartz and feldspar, clay, mica, and rock fragments (mainly polycrystalline quartz). Gravel- to pebble-sized rounded to angular clasts are interpreted as dropstones delivered by melting sea ice or icebergs (see “[Site U1339 thin sections](#)” in “[Core descriptions](#)”) (Figs. [F5](#), [F6](#), [F7](#), [F8](#), [F10](#)). Onboard petrographic thin section descriptions of two representative pebbles indicate that one of the main source lithologies for the ice-rafted material is metasandstone (see “[Site U1339 thin sections](#)” in “[Core descriptions](#)”) (Fig. [F11](#)). Some pebbles are composed of pumice or obsidian, suggesting a volcanic source.

Authigenic precipitates were also observed. Authigenic carbonate was found below 34 m core composite depth below seafloor (CCSF-A) in Holes U1339B–U1339D. Note that Hole U1339A extends only to 35.03 m CCSF-A. Authigenic carbonates occur more frequently below 145 m CCSF-A (Figs. [F5](#), [F6](#), [F7](#), [F8](#), [F12](#)), either as rhombohedra scattered in the sediment or as (semi-)lithified layers 5–10 cm thick. The disseminated dolomite rhombs range in size from 10 to 30  $\mu\text{m}$ , and crystallization occurs as pore space infilling in diatom cavities and/or as replacement of biosiliceous tests (Fig. [F12](#)). The authigenic carbonates were determined to be dolomite because of the presence of characteristic dolomite rhombs (Fig. [F12](#)) by XRD analysis (Fig. [F13](#)) (see XRD in “[Supplementary material](#)”).

Bioturbation is a common feature at Site U1339, as suggested by the rare occurrence of laminated intervals and the faint to pervasive mottling that characterizes most cores. The most commonly recognized trace fossils are *Planolites*, and a few examples of *Skolithos* were also observed. However, in most cases, bioturbation could not be related to specific ichnofacies types, and bioturbation intensity was mostly described as slight to moderate.

Coring disturbances, mainly in the form of subhorizontal gas expansion cracks and voids, were frequently observed in cores collected from all Site U1339 holes. Cracks and voids are likely caused by the high concentrations of methane found below the sulfate–methane transition (8–10 mbsf; see

“[Geochemistry and microbiology](#)”). Note that because of sediment loss from punctures, stratigraphic distortion may occur at puncture sites.

Depth variations of color reflectance parameter  $b^*$ , gamma ray attenuation (GRA) bulk density, and magnetic susceptibility were compared to lithologic variations at Site U1339 (Figs. [F5](#), [F6](#), [F7](#), [F8](#)). Overall, these parameters show distinct short-term variability and longer term trends that can be correlated to lithologic variations at both short- and long-term scales. GRA bulk density in mixed biogenic and terrigenous sediments increases with higher amounts of siliciclastics. Hence, sediments rich in detrital material have higher bulk densities than siliciclastic-poor, mainly biogenic sediments. Color reflectance parameter  $b^*$  reflects the yellowness of sediment, and these two parameters often run in tandem, with higher  $b^*$  values corresponding to less dense, more biogenic-rich sediments. Changes in magnetic susceptibility with depth mainly reflect volcanoclastic content, and a very good correlation exists between the thickest volcanic ash layers and the highest magnetic susceptibility excursions (Figs. [F5](#), [F6](#), [F7](#), [F8](#)).

## Discussion

The lithostratigraphic analysis of the sediment cores collected at Site U1339 as well as the comparison between sediment characteristics and depth variations in sediment color and physical properties suggest that late Pleistocene sedimentation on Umnak Plateau was influenced by ice sheet variability and in particular by glacial–interglacial changes in sea level and sea ice extent (Figs. [F5](#), [F6](#), [F7](#), [F8](#)). Glacial sediments are rich in silt-sized siliciclastic grains, probably reflecting greater terrigenous delivery to the site at times of low sea level than during interglacials, when much of the river sediment load would have been trapped on the wide continental shelf. Glacial sediments are also richer in granule- to pebble-sized clasts, which were probably delivered to the site by sea ice or glacial ice. Interglacial conditions are reflected by the predominance of biogenic components, mainly diatoms; however, it is unclear whether this predominance is due to higher productivity or less dilution by siliciclastic material.

According to the Site U1339 age model (see “[Biostratigraphy](#)” and “[Paleomagnetism](#)”), this variability occurs at very different scales. Considering that biostratigraphic data suggest a minimum average sedimentation rate for this site of 4.5 k.y./m, decimeter- to meter-thick rhythmic bedding occurs in the sub-Milankovitch range, whereas larger alternations between lithologies dominated by the two sediment types occur within the Milankovitch range. This variability is well represented by depth changes

in bulk density, where denser lithologies are richer in siliciclastics. Color reflectance parameter  $b^*$  also shows clear changes on the same scales and is more negative in the more grayish silt-rich sediments. Lithologic changes are represented to a lesser extent by magnetic susceptibility.

Laminated intervals are rare at Site U1339, indicating that bioturbation, and therefore oxygenated conditions, prevailed during most of the depositional history at this site. However, there is no clear relationship between the depths at which the laminated intervals occur, the deepest minima in bulk density recorded by GRA, and the other parameters shown in Figures F5, F6, F7, and F8, suggesting that low-oxygen conditions are not uniquely controlled by the same processes responsible for lithologic change. Lamination includes thin laminae dominated by foraminifer tests. Based on the analysis of several smear slides, these laminae appear to be dominated by the benthic foraminifer *Bulimina* sp., which is characteristic of low oxygen content (Kaiho, 1994).

At this stage, it is not possible to conclude that the association between volcanic ash layers and laminated intervals is the result of a causal relationship between the two. Intermixed ash and ash-filled mot-tles are very common at this site, showing that thin ash layers are ubiquitous and with bioturbation are mixing into the surrounding sediment. The low-oxygen conditions that allowed the preservation of the laminated intervals could also have helped preserve adjacent volcanic ash layers, accounting for an apparent association between laminated sediments and ash (Fig. F9). However, the presence of thin, unbioturbated volcanic ash layers with no visible association with laminated intervals suggests that the absence of bioturbation at this site is not always made visible by changes in sediment composition or color.

Several prominent volcanoclastic layers show either parallel or undulating sharp contacts with the underlying sediment. Conversely, the top boundary is gradual and the volcanoclastic material is mixed with the overlying diatom ooze, most likely from bioturbation. Some black volcanoclastic layers are also characterized by graded bedding, with coarser clasts concentrated at the bottom (Fig. F9B). This may indicate redeposition by vertical density currents (e.g., Carey, 1997).

## Biostratigraphy

Core catcher samples from Site U1339 are dominated by high-diversity siliceous microfossil assemblages. The samples also contain assemblages of calcareous and organic-walled microfossils with high diversity.

In general, the preservation of the different microfossil groups ranges from very good to moderate. Biostratigraphic datum events derived from radiolarians, diatoms, and silicoflagellates show that Site U1339 covers a Pleistocene sequence (Fig. F14; Table T2). Age control of the bottom of the sequence is difficult because of the very rare occurrences of biostratigraphic markers. A silicoflagellate datum event indicates that the bottom of the hole is slightly above the Brunhes/Matuyama Chron boundary (0.781 Ma), but this requires further investigation. The microfossils recovered comprise polar to subpolar floral and faunal assemblages that reflect the geographic setting of Site U1339 and glacial-interglacial changes. The dominance of *Neodenticula seminae* in the diatom assemblage clearly reflects fluctuations of Alaskan Stream influence. In addition, benthic foraminifer faunal changes likely reflect changes in dissolved oxygen concentrations and/or nutrient contents of the bottom water mass.

## Calcareous nannofossils

All core catcher samples from Holes U1339A–U1339D were examined to assess the presence, abundance, state of preservation, and taxonomic composition of calcareous nannofossils (Table T3). These data were recorded semiquantitatively following the codes defined in “Biostratigraphy” in the “Methods” chapter. At Site U1339, more than half of the samples are barren of calcareous nannofossils, whereas only eight samples contain abundant to common nannofossil assemblages. In general, preservation of the observed specimens varies from good to moderate throughout the samples. *Coccolithus pelagicus* and small geophyrocapsids are generally the dominant taxa. Reworked nannofossils were found in some core catcher samples and are particularly important in Sample 323-U1339B-5H-CC, which contains abundant specimens of *Coccolithus miopelagicus* (Miocene).

No calcareous nannofossil datum was proposed for this site because barren intervals prevented full interpretation. *Emiliania huxleyi* was identified in Samples 323-U1339B-1H-CC through 4H-CC, 323-U1339C-1H-CC, and 323-U1339D-1H-CC and 4H-CC. However, its first occurrence (FO) datum (0.29 Ma), which marks the base of nannofossil Zone NN21 (Martini, 1971), could not be reasonably constrained because of the barren intervals below in Holes U1339B–U1339D. A single specimen of *Pseudoemiliania lacunosa* was observed in Sample 323-U1339-16H-CC, but no specimens were found in the upper and lower sections of this hole or in other holes, and thus the last occurrence (LO) datum of this species (0.44 Ma) was not considered for age model construction of this site. The following samples occur

within Zone NN21: Samples 323-U1339B-1H-CC through 4H-CC, 323-U1339C-1H-CC, and 323-U1339D-1H-CC through 4H-CC, whereas Samples 323-U1339B-16H-CC through 22H-CC are within Zone NN19 (defined at its top by the LO of *P. lacunosa*). The limits of these two zones and the extension of Zone NN20 (which spans the LO of *P. lacunosa* at 0.44 Ma and the FO of *E. huxleyi* at 0.29 Ma) are thus not well constrained at this site.

Because of low specimen numbers, relative abundance counts were not performed for samples from Site U1339. However, all taxa observed are characteristic of the subarctic and transitional coccolithophore zones in the Pacific (Okada and Honjo, 1973) and have been observed frequently in cold-water environments and glacial sediments.

### Planktonic foraminifers

All core catcher samples from Holes U1339A–U1339D were examined for planktonic foraminifers from the >125  $\mu\text{m}$  size fraction (Table T4). The 125  $\mu\text{m}$  fraction of mudline samples from each hole was also studied. All core catcher samples and mudline samples are dominated by diatoms and, to some degree, coarse-grained clasts. Planktonic foraminifers are present in almost all samples except Samples 323-U1339B-9H-CC, 16H-CC, and 22H-CC; 323-U1339C-12H-CC; and 323-U1339D-9H-CC, 11H-CC, and 20H-CC. The fauna is mainly dominated by *Neogloboquadrina pachyderma* (sinistral). This species dominates modern subpolar–polar environments and is largely temperature dependent (Bé and Tolderlund, 1971). It is also the dominating species in sediment traps in the Bering Sea (Asahi and Takahashi, 2007). Additional species include *Globigerina bulloides*, *Globigerina umbilicata*, and *Neogloboquadrina pachyderma* (dextral), which are also found in sediment traps in the Bering Sea, reflecting subpolar conditions (Asahi and Takahashi, 2007). This fauna does not change significantly throughout the Pleistocene. Exceptions from the main distribution are Samples 323-U1339B-18H-CC and 323-U1339C-20H-CC, where *N. pachyderma* (dextral) is found in higher numbers than *N. pachyderma* (sinistral), and Sample 323-U1339C-20H-CC, where *G. bulloides* is as abundant as *N. pachyderma* (sinistral). Both *N. pachyderma* (dextral) and *G. bulloides* are characteristic of warmer sea-surface temperatures (SST) than *N. pachyderma* (sinistral) (e.g., Bé and Tolderlund, 1971).

### Benthic foraminifers

Twenty-nine species of benthic foraminifers were recovered in 79 samples from Holes U1339A–U1339D (Tables T5, T6, T7, T8). The majority of samples con-

tain abundant calcareous foraminifers with generally low diversity ranging from ~5 to 10 species per sample. These species show close affinities to those recorded in recent sediments within or near the oxygen minimum zone (OMZ) in the Sea of Okhotsk between 600 and 1750 m water depth (Bubenshchikova et al., 2008), and many have been recorded in Bering Sea deepwater sediments over the last glacial period (Okazaki et al., 2005; Khusid et al., 2006). Assemblages are somewhat different from those of the North Pacific Emperor seamounts (Butt, 1980). Although this site is beneath relatively deep waters, high productivity in surface waters greatly expanded the OMZ. There appears to be no long-term shift in fauna throughout the section; rather, samples exhibit changes in species dominance over timescales shorter than the sampling resolution is able to resolve. These assemblages are described below.

#### Assemblage I (*Islandiella norcrossi*–*Elphidium* cf. *batialis*)

Assemblage I is varyingly dominated by *Islandiella norcrossi*, *Elphidium* cf. *batialis*, *Stainforthia* spp., *Uvigerina* cf. *peregrina*, and *Uvigerina auberiana* in the samples listed in Tables T5, T6, T7, and T8. These species are predominantly found in the shallow infauna (0–1.7 cm) in the Sea of Okhotsk and are therefore generally indicative of higher dissolved-oxygen levels in the bottom water within the OMZ.

#### Assemblage II (*Nonionella labradorica*–*Globobulimina pacifica*)

Assemblage II is dominated by the intermediate and deep infaunal species *Nonionella labradorica*, *Globobulimina pacifica*, *Valvulineria* sp., and *Nonionella turgida digitata* in Samples 323-U1339A-3H-CC, 7H-CC, 12H-CC, and 20H-CC; 323-U1339B-1H-CC, 3H-CC, and 6H-CC; and 323-U1339D-6H-CC and 8H-CC. These species are found predominantly in the intermediate to deep infauna (1.8–5.2 cm) in the Sea of Okhotsk and are generally considered more tolerant of lower dissolved-oxygen levels.

The variation in abundance of these two assemblages is likely linked to glacial–interglacial changes in primary productivity and deepwater ventilation, although further high-resolution work is needed to ascertain its relationship with global climate.

### Ostracodes

Core catcher samples were examined for the presence of ostracodes, but only one specimen belonging to the genus *Argilloecia* was found in Sample 323-U1339B-10H-CC.

## Diatoms

Diatom biostratigraphy is based on the analysis of core catcher samples from each core from all holes at Site U1339. Wherever possible, datums were refined by analyzing additional toothpick samples taken at regular intervals from the core in question. Depth positions and age estimates of biostratigraphic marker events are shown in Tables T9, T10, T11, and T12. Diatoms are the dominant microfossils at Site U1339 and show good preservation throughout this Pleistocene record.

Only four cores were retrieved from Hole U1339A because of mechanical problems with the coring system. As a result of the high sedimentation rate in this hole, no datums were observed.

In Hole U1339B, the LO of *Proboscia curvirostris* was identified between Samples 323-U1339B-9H-CC and 8H-CC, giving a preliminary age of 0.28 Ma based on the result from the piston core at Site ES on the northernmost Emperor seamount (T. Katsuki, unpubl. data). A second age of 0.31 Ma was initially assigned to the interval between 323-U1339B-9H-3, 45 cm, and 9H-4, 45 cm, by the species *Thalassiosira jouseae*. However, in Hole U1339C, both datums were estimated in the same interval between Samples 323-U1339C-10H-CC and 10H-1, 25 cm. Furthermore, the results in Hole U1339D (Samples 323-U1339D-7H-CC and 8H-CC, for *P. curvirostris*, and Cores 323-U1339D-6H and 7H, for *T. jouseae*) contradict the LO relationship in Hole U1339B. Previous studies located the LO of *T. jouseae* just below the LO of *P. curvirostris* (Yanagisawa and Akiba, 1998; T. Katsuki, unpubl. data, Site KH99-03 ES-PC). The different LO patterns for both species at this site may be the result of the low abundance of *P. curvirostris* or the limited sample volume used for slide preparation. However, the extra sampling conducted for Core 323-U1339C-10H revealed that the LOs of *P. curvirostris* and *T. jouseae* co-occur in Sample 323-U1339C-10H-1, 25 cm, confining the two datums to an interval of 25 cm. This suggests that the LOs of both species are closely tied, and a finalized LO age of 0.3 Ma was assigned at this site. This age estimate is further supported by the LO datum of radiolarian *Spongodiscus* sp., which suggests an age of 0.3 Ma at similar depths. In the subarctic Pacific and around Japan, the datum of *P. curvirostris* is defined as 0.3 Ma (Barron and Gladenkov, 1995; Yanagisawa and Akiba, 1998). Thus, estimated diatom datums are used for general age determination at this site, although minor datum revisions at the 0.01 m.y.-scale resolution will be needed in the near future. The preceding older datum at 0.9 Ma was not observed in all holes. Using the biostratigraphic results of other microfossils and magnetic stratigraphy, Site U1339 cores younger

than 0.3 Ma were assigned to the *Neodenticula seminae* Zone, and cores from 0.3 Ma to the bottom of Holes U1339B–U1339D were assigned to the *P. curvirostris* Zone (Yanagisawa and Akiba, 1998). All Hole U1339A cores were assigned to the *N. seminae* Zone.

Diatom assemblages at Site U1339 are composed mainly of *N. seminae*, *Actinocyclus* spp., and *Thalassiosira* spp. (*T. antarctica* spores, *T. latimarginata* s.l., and *T. oestrupii*) throughout the obtained cores. In addition, relative abundances of coastal water diatoms, including *Chaetoceros* spores, and freshwater diatoms are common in most samples at this site. The occurrence of these coastal/freshwater diatoms can be explained by the proximal location of this site to the Bering Sea shelf. However, such species have been documented to reside in sea ice (von Quillfeldt et al., 2003) and therefore may be produced in situ and may not be a result of lateral transport. In the northeastern subarctic Pacific, the relative abundance of *N. seminae* in relation to the total number of diatoms has been used as a proxy for the Alaskan Stream (Sancetta, 1982). Indeed, at this site, a clear negative relationship was observed between the Alaskan Stream indicator and pelagic cold-water species for all cores, suggesting that Site U1339 is located at the salinity margin.

## Silicoflagellates

Because of diatom abundances, silicoflagellate skeletons are a minor component of the siliceous microfossils at this site. Silicoflagellate abundances are trace to few and, rarely, common (Table T13). Based on the silicoflagellate zonation established by Ling (1973b, 1992), one datum event was detected in Holes U1339B and U1339C and three were detected in Hole U1339D. The bottom of Hole U1339A did not reach the first (youngest) datum event at 0.24 Ma.

The first datum, LO of *Distephanus octonarius* (0.244 Ma), was estimated between Samples 323-U1339B-5H-CC and 6H-CC, between Samples 323-U1339C-7H-CC and 8H-CC, and between Samples 323-U1339D-5H-CC and 6H-CC. The age estimation for this datum is based on the results at Site 185 of DSDP Leg 19 (Ling, 1973b), and the calibrated age is  $0.24 \pm 0.05$  Ma. The interval above this datum event was assigned to the *Distephanus octangulatus* Zone in Ling (1973b).

The other two events, FO of *D. octangulatus* (0.741 Ma) and LO of *Dictyochoa subarctios* (0.736 Ma), were estimated between Samples 323-U1339D-20H-CC and 21H-CC. In Hole U1339B, *D. octangulatus* was observed in the bottommost sample (323-U1339B-22H-CC), and thus the datum event may be located lower than the bottom of the hole. These datums

were found slightly above the Brunhes/Matuyama Chron boundary during Leg 19 in the North Pacific (Ling, 1973b) and Ocean Drilling Program (ODP) Leg 128 in the Sea of Japan (Ling, 1992). However, geomagnetic analysis hints that the Brunhes/Matuyama boundary may possibly be located at ~189 mbsf in Hole U1339B. If this geomagnetic information becomes conclusive, the datum information of the FO of *D. octangulatus* and the LO of *D. subarctios* must be reconsidered at this or other sites in the Bering Sea.

### Radiolarians

Radiolarian biostratigraphy is based on the analysis of core catcher samples from Holes U1339A–U1339D. The preservation of radiolarians in samples from all cores is generally good, but abundance is common or few and diversity is low (Table T14). Radiolarian stratigraphy at Site U1339 extends from the *Botryostrobus aquilonaris* Zone to the *Stylatractus universus* Zone (Kamikuri et al., 2007). The radiolarian assemblage is composed mainly of *Cycladophora davisiana*, *Ceratospyrus borealis*, and *Stylodictya validispina*, which occur in most of the sections. Five radiolarian LO datums derived from the subarctic Pacific were identified at this site (Table T15):

- *Lychnocanoma nipponica sakaii* (50 ka)
- *Amphimelissa setosa* (80–100 ka)
- *Spongodiscus* sp. in Ling (1973a) (280–320 ka)
- *Axoprunum acquilonium* (250–430 ka)
- *Stylatractus universus* (410–510 ka)

The datums *L. nipponica sakaii*, *A. setosa*, and *Spongodiscus* sp. are basically consistent with each other in a comparison of all holes, indicating consistent occurrences and reliable age controls at this site. However, the datums *A. acquilonium* and *S. universus* are supported only by seldom occurrences in Holes U1339B–U1339D, indicating slightly uncertain top positions of stratigraphic age. Plausible datum events of both species occur in Hole U1339C (LO of *A. acquilonium*, between Cores 323-U1339C-9H and 10H, and LO of *S. universus*, between Cores 323-U1339C-11H and 12H). No radiolarian datum was identified below the LO of *S. universus*. Further age control for the lower sections is difficult because of very rare occurrences of the lower radiolarian stratigraphic marker (LO of *Eucyrtidium matuyamai* [0.9–1.5 Ma]).

### Palynology: dinoflagellate cysts, pollen, and other palynomorphs

Palynological assemblages were examined in core catcher samples from Holes U1339A, U1339B, and

U1339D (Table T16). These samples were extremely difficult to process because of abundant detrital silica and diatoms. Heavy liquid (sodium polytungstate) was systematically used to separate organic compounds from the silica. This preparation may have resulted in an underestimation of palynomorph abundances because some organic particles may have been trapped and entrained within the silica. Nevertheless, well-preserved and abundant palynomorphs, including mainly dinoflagellate cysts accompanied by variable numbers of pollen and spores (mostly bisaccate pollen and sphagnum), freshwater green algae (*Pediastrum* and *Botryococcus*), and organic linings of benthic foraminifers, were recovered in most samples. Preservation is mostly good, and very few reworked palynomorphs were recorded (Table T16).

All investigated samples yielded moderate to abundant dinoflagellate cysts (Table T16). However, the assemblages have relatively low species diversity (16 recorded taxa), probably because of insufficient on-board sample preparation. The dinoflagellate cyst assemblages are highly dominated by two taxa, *Brigantedinium* spp. and *Islandinium minutum*, which are produced by heterotrophic protoperidinal dinoflagellates feeding on diatoms (Jacobson and Anderson, 1986). Such assemblages could be related to extremely high diatom production and high upwelling intensity (Radi and de Vernal, 2004). The assemblages in Samples 323-U1339B-1H-CC and 3H-CC are marked by the dominance of *I. minutum*. In the modern ocean, this species shows its highest abundance in the Arctic and in circum-Arctic environments with very low SST and seasonal sea ice cover (Rochon et al., 1999; Head et al., 2001). In these samples (323-U1339B-1H-CC and 3H-CC), the percentage of *I. minutum* reaches up to 67%, remarkably analogous to occurrences in the North Water Polynia (Hamel et al., 2002). The assemblages also include taxa that characterize high-latitude environments, such as *Spiniferites frigidus* and the Arctic morphotype of *Polykrikos*. On the whole, the assemblages reflect a high-productivity environment with low SST and probably seasonal sea ice cover. Two main assemblage zones were distinguished: an assemblage dominated by *I. minutum* in Samples 323-U1339B-1H-CC and 3H-CC and an assemblage dominated by *Brigantedinium* spp. throughout the sequences.

Terrestrial palynomorphs are dominated by *Picea* and *Pinus* pollen grains, which occur in moderate to low numbers throughout the sequences. Their occurrence indicates atmospheric and/or oceanic long-distance transport and likely reflects the vegetation of adjacent land (Alaska and Siberia). Freshwater algae

occur only in Samples 323-U1339A-1H-CC through 4H-CC, 323-U1339B-1H-CC through 7H-CC, and 323-U1339D-2H-CC.

Sample 323-U1339B-22H-CC contains a single specimen of *Hystrichospaeropsi obscura*, with an LO at 0.7 Ma in the North Atlantic (Mudie, 1987). However, no specimens of this species were seen in other slides from the same sample or after verification in the bottommost cores of Hole U1339D (Samples 323-U1339D-19H-5, 75 cm; 20H-3, 73 cm; and 21H-2, 77 cm). Thus, this biostratigraphic marker cannot be applied with confidence.

## Paleomagnetism

The archive halves of all cores recovered at Site U1339 were measured on the three-axis cryogenic magnetometer at 2.5 cm intervals. Natural remanent magnetization (NRM) was measured before (NRM step) and/or after (demagnetization step) stepwise alternating-field (AF) demagnetization in peak fields as high as 20 mT. Core 323-U1339A-1H through Section 4H-4 and Sections 323-U1339B-7H-2 and 7H-3 were measured at NRM step and at 10 and 20 mT demagnetization steps, but other cores from Holes U1339A and U1339B were measured at only 10 and 20 mT demagnetization steps. Cores from Holes U1339C and U1339D were measured at only 20 mT demagnetization step to keep up with core flow.

Paleomagnetic directions after 20 mT AF demagnetization are plotted in Figure F15. The mean inclinations are nearly 70° over the entire depth range of the cores, and the site axial dipole inclination is ~72°, indicating that all sediments are from the Brunhes Chron (0–781,000 y before present [BP]), although an alternative interpretation is also possible (see below). The inclinations show common negative values, but almost all of them are associated with narrow intervals of sediment diagenesis or are a consequence of ash layers. The declinations were re-oriented with the FlexIt core orientation tool and also average near 0°, as expected for normal polarity of the Brunhes Chron.

There is a distinctive relationship between sediment intervals of low or negative inclination and NRM intensity. In many cases, the low/negative inclinations noted in Figure F15 are associated with anomalously strong NRM intensities that are often 10 times the NRM intensity values in the surrounding sediments. This relationship is illustrated in Figure F16. The anomalous intervals have a distinctive intensity maximum that is significantly greater than the intensity in surrounding sediments, and they also have

anomalously low inclinations in exactly the same intervals. This could be attributed to the authigenic growth of greigite ( $\text{Fe}_3\text{S}_4$ ) in the sediments after deposition due to sulfate reduction, methanogenesis (e.g., Blanchet et al., 2009), or the presence of ice-rafted pebbles. Geochemical data indicate that sulfate reduction starts within the uppermost 20 m and methanogenesis is present within the uppermost 50 m.

Further evidence of early diagenetic processes is noted in the overall NRM intensities, which are strong at the core top ( $\sim 10^{-1}$  A/m<sup>2</sup>) but diminish to  $\sim 10^{-3}$  A/m<sup>2</sup> near 200 mbsf (Fig. F17). NRM intensities first noticeably drop at 20–25 mbsf, consistent with sulfate reduction. This initial drop is likely associated with magnetic mineral dissolution under anoxic conditions, which diminishes overall NRM intensity. Lower NRM intensity due to selected magnetic mineral dissolution occurs throughout the sediment column below ~20 mbsf; narrow intervals of strong NRM intensity associated with greigite (or ice-rafted pebbles) occur superimposed on this general trend. Figure F17 shows that NRM values diminish below ~20 mbsf, whereas magnetic susceptibility data stay at a somewhat constant value. Near 170 mbsf, NRM intensities diminish notably again. The lower NRM intensities with more common negative inclinations below 170 mbsf may indicate the Brunhes/Matuyama boundary and that the lower intensities are due to incomplete removal of a strong normal polarity overprint from a weaker reversed polarity intensity.

NRM after 20 mT demagnetization was normalized by magnetic susceptibility (Fig. F17) to estimate magnetic field paleointensity in these sediments, although sediment variability and the presence of magnetic mineral dissolution plus intermittent greigite authigenesis make this a problematic task. The examination of paleointensity variations above 170 mbsf indicates no notable features. Relative paleointensity in the uppermost 20 m should provide a reasonable estimate of field variability for the last 100,000 y or so, but these data will be considered later when they can be compared with other independent data sets from IODP Expedition 323.

Finally, no clear magnetic field excursions in these sediments were found. The only exception may be an interval of reversed inclinations and anomalous declinations near 51 mbsf in Holes U1339B and U1339C that are associated with low NRM intensities. This interval is tentatively associated with Excursion 7 $\alpha$ , which is ~190,000 y BP (Lund et al., 2006).

## Geochemistry and microbiology

### Interstitial water chemistry

Seven interstitial water samples were extracted from 10 cm whole-round sediment sections from Hole U1339A at a resolution of two samples per core in the first core, three samples per core in the second core, and one sample per core thereafter, covering a depth of ~33 mbsf.

In microbiology-dedicated Hole U1339B, samples from the uppermost 35 m were taken at high resolution; 10 cm whole rounds were taken every 25 cm for the first two sections of the first core. Sampling resolution then decreased to every 75 cm for Sections 323-U1339B-1H-3 through 1H-6 and Cores 2H through 4H. The uppermost 35 m of sediment was cut into whole rounds at a near in situ temperature of 7°C in the Cold Laboratory. To prevent oxidation, whole rounds were stored in a nitrogen-filled glove box at 7°C until squeezed. One sample per core was taken from Cores 323-U1339B-5H through 22H. Interstitial water samples were processed for routine shipboard geochemical analyses (see “**Geochemistry**” in the “Methods” chapter). Samples were also collected for shore-based analyses of sulfur and oxygen isotopes of sulfate and hydrogen sulfide, trace metals, dissolved organic carbon, and fatty acids.

### Chlorinity, salinity, alkalinity, dissolved inorganic carbon, and pH

Chloride concentrations in Holes U1339A and U1339B are fairly constant throughout the sediment column, averaging ~540 mM. Downhole salinity values are nearly constant throughout Hole U1339B, varying only between 34 and 36 (Fig. F18D, F18I).

Alkalinity increases from 3 to 30 mM in the uppermost 10 m and reaches a maximum of 53 mM at ~120 mbsf in Hole U1339B (Fig. F18C). Curvature is well defined throughout the profile. The dissolved inorganic carbon (DIC) profile is similar to the alkalinity profile in shape and concentration range (Fig. F18A). pH values range from 7.7 to 8.2, with two local maxima at 16 and 78 mbsf in Hole U1339B (Fig. F18B).

### Dissolved sulfate and hydrogen sulfide

Sulfate concentrations decrease from seawater values to values below detection limit at ~10 mbsf (Fig. F18E). Dissolved hydrogen sulfide is below detection limit throughout the depths sampled in Hole U1339B, with the exception of 2.25 and 21.8 mbsf, where concentrations are 1.6 and 14.5  $\mu\text{M}$ , respectively (data not shown).

### Dissolved ammonium and phosphate

Ammonium concentrations increase throughout Hole U1339B and range from 0.02 to 5.6 mM (Fig. F18H). Phosphate concentrations increase to 186  $\mu\text{M}$  throughout the uppermost ~30 m; from 30 to 200 mbsf, concentrations vary between ~100 and 200  $\mu\text{M}$  (Fig. F18G).

### Dissolved calcium, magnesium, sodium, and potassium

Calcium concentrations range from 15.8 to 1.3 mM, decreasing downhole in the uppermost 10 m and remaining relatively constant thereafter to 200 mbsf (Fig. F19D). Potassium, magnesium, and sodium concentrations are 19.7–6.5, 86.5–25.2, and 770–360 mM, respectively, throughout the sediment column, and their downhole profiles are roughly similar (Fig. F19A–F19C). These constituents are highly variable in the uppermost ~35 m.

### Dissolved iron, manganese, boron, lithium, and strontium

Iron concentrations are less than ~6  $\mu\text{M}$ . There are a few outliers in the ~10–40  $\mu\text{M}$  range in the uppermost ~100 m (Fig. F19G). Manganese concentrations are less than ~10  $\mu\text{M}$  and also remain relatively constant with depth (Fig. F19E, F19G).

Boron concentrations increase between near seawater values (416  $\mu\text{M}$ ) and 1800  $\mu\text{M}$  at 140 mbsf (Fig. F19H) and then drop slightly to ~1400  $\mu\text{M}$  below 140 mbsf. Lithium concentrations at the surface of the upper sediment column are near seawater values (26  $\mu\text{M}$ ), decrease rapidly toward a well-defined minimum at ~10 mbsf, and then increase monotonously to >30  $\mu\text{M}$  with depth (Fig. F19I). Strontium concentrations, although scattered, decrease in the uppermost ~40 m. Deeper in the sediment column, strontium increases to local maxima of 101 and 125  $\mu\text{M}$  at 60 and 185 mbsf, respectively (Fig. F19E).

### Volatile hydrocarbons

Samples for volatile hydrocarbon analyses were taken from Holes U1339A and U1339B at the same resolution as the interstitial water samples described above. Methane concentrations are close to detection limit in the uppermost ~10 m. At the depth of sulfate depletion at ~10 mbsf, methane concentrations increase significantly (Fig. F18H). Below 10 mbsf, methane concentrations are minimum estimates. From 19.75 to 185 mbsf, ethane concentrations range from 0.25 to 2.6  $\mu\text{M}$ . Throughout the rest of the hole, ethane concentrations are below detection limit.

## Sedimentary bulk geochemistry

Splits of squeeze cakes from interstitial water whole rounds from Holes U1339A and U1339B were used for the analysis of solid-phase total carbon (TC), total nitrogen (TN), total sulfur (TS), and total inorganic carbon (TIC). From these analyses, total organic carbon (TOC) and calcium carbonate ( $\text{CaCO}_3$ ) concentrations were calculated (see “**Geochemistry**” in the “Methods” chapter) (Fig. F20).  $\text{CaCO}_3$  concentrations range from 0 to 13.3 wt% (average = 2.1 wt%). TOC and TN contents range from 0.47 to 1.83 wt% (average = 0.98 wt%) and from 0.07 to 0.23 wt% (average = 0.12 wt%), respectively.  $\text{CaCO}_3$ , TOC, and TN concentrations are highest near the sediment/water interface and decrease relatively sharply in the uppermost 10 m of the sediment column. In contrast, TS concentrations increase in the upper portion of the sediment column and fluctuate between 0.2 and 0.8 wt% to 200 mbsf (Fig. F20D). Splits of squeeze cakes were also collected and treated for shore-based analyses of bulk elemental composition, iron mineral phases, and iron-monosulfide and pyrite content and sulfur isotope composition.

## Microbiology

Samples for community structure and total prokaryotic cell abundance were collected adjacent to interstitial water whole rounds at the resolution described above. Samples were fixed according to “**Microbiology**” in the “Methods” chapter. All microbiology analyses will be performed postcruise.

PFT concentrations are below detection limit throughout Hole U1339B, indicating that contamination from drill fluid is insignificant.

## Conclusion

Dissolved sulfate, DIC, alkalinity, phosphate, and ammonium concentration profiles suggest relatively high rates of carbon turnover (i.e., microbial activity) at Site U1339, similar to other IODP shelf Sites U1343, U1344, and U1345. The relatively shallow sulfate–methane transition zone (SMTZ) is presently between 8 and 10 mbsf. The significance of anaerobic oxidation of methane (AOM) for carbon turnover is evident in the DIC concentration profile. The steepest DIC concentration gradient is directly above the SMTZ, suggesting that the highest DIC flux occurs from this zone.

Calcium and magnesium profiles show depletion at the depth of the present SMTZ. This suggests formation of authigenic Mg-rich carbonate, such as dolomite, driven by the production of DIC during AOM and an increase in pH and alkalinity, which leads to

oversaturation of the interstitial water with respect to carbonate.

Accumulation of ammonium and phosphate is indicative of microbially mediated organic matter degradation. A local minimum in phosphate concentration at ~60 mbsf indicates inorganic consumption of phosphate.

## Physical properties

Cores recovered from Holes U1339A–U1339D from Site U1339, located on the northern end of Umnak Plateau, were placed on the Special Task Multisensor Logger (STMSL) “fast track” to record magnetic susceptibility and GRA bulk density values. Core sections were then allowed to warm to ambient laboratory temperature (19°–20°C) before being placed on the Whole-Round Multisensor Logger (WRMSL) to measure magnetic susceptibility, GRA bulk density, *P*-wave velocity, and noncontact resistivity. Cores 323-U1339B-1H through 4H were mostly consumed for microbiology sampling after STMSL processing, so no WRMSL data are available for these cores. By the third core (323-U1339A-3H) it was apparent that allowing the cores to warm to ambient temperature was also allowing gas expansion, probably due to the disassociation of intergranular particles of methane gas hydrate. The freed water and expanding gas (expansion ratio on the order of 1:165) significantly disrupted the depositional and structural fabric of the core sediment and presented a significant hazard for core handling. To minimize this disturbance, small holes were drilled through the core liner of the sections of Hole U1339A that were already racked and housed in the core laboratory. Subsequently, for Holes U1339B–U1339D, holes were drilled through the core liners while the cores were on the catwalk. To further mitigate core disruption, whole-round sections were scanned on the WRMSL as soon as possible after recovery. Next, natural gamma radiation (NGR) logging and thermal conductivity measurements were conducted routinely. Because of operational problems and time constraints, *P*-wave velocity and sediment shear strength measurements were not determined on selected sections of the working halves after core splitting.

## Magnetic susceptibility

Magnetic susceptibility values vary widely, reflecting downhole changes in relative concentrations of terrigenous and tephra debris over biogenic material. These variations were expected because, during episodes of glacially lowered sea level, Alaskan drainage of the Yukon and Kuskokwim rivers presumably emptied near the shelf edge in the vicinity of the

nearby Pribilof Islands, 200–250 km to the north (VanLaningham et al., 2009). Many of the recovered ash layers were probably launched by the basaltic centers of these islands and the more siliceous edifices of the Aleutian Islands, located an equal distance to the south.

Magnetic susceptibility data exhibit a downhole pattern of cyclic excursions between high and low values. These data are presented and described in “[Lithostratigraphy](#)” and “[Stratigraphic correlation](#).”

### GRA wet bulk density

WRMSL GRA bulk density readings also oscillate downhole from relatively low values reflecting higher concentrations of biogenic (mainly diatom) debris to high values reflecting denser sediment richer in terrigenous components. In the “[Lithostratigraphy](#)” and “[Stratigraphic correlation](#)” sections, GRA data are displayed and compared with downhole changes in lithologic characteristics. Bulk density extracted from discrete sediment samples collected from the working halves is described below.

### Natural gamma radiation

NGR readings vary generally rhythmically with depth from highs of 25–40 counts/s to lows of ~10 counts/s. High NGR likely tracks clay mineral-bearing sediment, whereas low NGR tracks less radiogenic deposits richer in biogenic debris. Peaks in NGR are 10–25 m apart, reflecting sections of more abundant deposition of terrigenous material over Umnak Plateau. The downhole NGR profile for Hole U1339D, which is similar to those for combined Holes U1339A and U1339B as well as Hole U1339C, is displayed in Figure [F21](#).

### P-wave velocity

WRMSL *P*-wave velocity was measured on the four cores taken from Hole U1339A. Because readings for Cores 323-U1339A-3H and 4H were seriously degraded by core-cracking and gapping caused by gas expansion, the *P*-wave logger was turned off for all core sections deeper than ~33 mbsf. The noncontact resistivity scanner was also turned off because of noisy readings. Velocity readings acquired in the uppermost ~15 m of Holes U1339A and U1339D range from ~1.54 km/s near the seafloor to <1.5 km/s at ~4 mbsf to ~1.57 km/s at the maximum depth of measurement. Because of the presence of gas bubbles and cracks, most of the recorded values below a depth of a few meters are questionable. Reliable in situ downhole velocity measurements are reported in “[Downhole measurements](#).”

### MAD (discrete sample) wet bulk density

To measure moisture and density (MAD) properties, discrete samples of core sediment were taken from the working halves of the split sections. For Cores 323-U1339A-1H and 2H, discrete samples of ~10 cm<sup>3</sup> were collected across 2 cm wide segments of each core section, typically at 50–51 and 99–100 cm from the section top. To speed data gathering and processing for deeper cores, sediment samples from Holes U1339A and U1339B were taken across just one segment of core section, typically at 29–31 cm. Below Core 14H, discrete sampling was typically limited to odd-numbered sections (i.e., 1, 3, 5, and 7), depending on core recovery. The sediment sampling tool was a 2 cm inner diameter plastic syringe that matched the throat opening of a calibrated and numbered sample vial into which the sample was extruded.

The depth distribution of wet bulk density reveals a cyclicity of high values averaging ~1.6 g/cm<sup>3</sup> and low values of ~1.4 g/cm<sup>3</sup> (Fig. [F22](#)). Peaks and troughs of bulk density excursions are commonly separated by 25–40 m. The succession of highs and lows presumably reflects relatively terrigenous-rich and biogenic-rich sediment. Average bulk density increases gradually from a near-seafloor value of 1.35 g/cm<sup>3</sup> to 1.55 g/cm<sup>3</sup> at the bottom of the hole at ~200 mbsf. This gradient of ~0.1 g/cm<sup>3</sup>/100 m of depth most likely expresses sediment compaction.

### MAD porosity and water content

Porosity (percent pore space of wet sediment volume) measured on core samples exhibits an oscillating cyclicity with depth similar but of opposite polarity to the depth distribution of wet bulk density (Table [T17](#)). Water content, which is directly proportional to porosity, tracks its downhole distribution. Both curves are shown in Figure [F23](#). Variations in porosity and water content dominantly reflect the changing concentration of biogenic debris—particularly highly porous diatom frustules—with respect to more terrigenous and less porous sediment. Average porosity decreases downhole from a near-surface value of ~85% to ~65% at ~200 mbsf, presumably reflecting compaction (Fig. [F23](#)).

### Grain density

Grain (mineral) density versus depth oscillates from ~2.95 to ~2.3 g/cm<sup>3</sup> (Fig. [F24](#); Table [T17](#)). One-point excursions to extreme high and low values are probably spurious readings. Peaks are separated by 15–30 m. Grain density generally decreases downhole from a near-surface value of 2.65 g/cm<sup>3</sup> to 2.55

g/cm<sup>3</sup> at ~200 mbsf. Grain density variations presumably reflect interbedded diatom-rich and terrigenous-rich units and possibly a downhole overall trend of increasing diatom frustules and debris. This trend is similar to the downhole decrease in thermal conductivity (Fig. F23), which may also track increasing diatom content.

### Thermal conductivity

Thermal conductivity was routinely measured toward the middle (~70–80 cm) of Section 3 and commonly also in Section 6 of each core from Holes U1339A–U1339D. Values range widely from a low of ~0.5 W/(m·K) to >1 W/(m·K). The smallest range of values (~0.96–0.66 W/[m·K]) was recorded in Hole U1339D (Fig. F25). Lower values presumably reflect water-rich diatomaceous sections, whereas higher values reflect sections with more abundant terrigenous debris. In Hole U1339D, thermal conductivity generally decreases downhole from 0.8 W/(m·K) near the surface to 0.7 W/(m·K) at ~200 mbsf. This downhole decreasing trend is less clear in thermal conductivity data from Hole U1339C sections and is not exhibited by thermal conductivity data from combined Holes U1339A and U1339B.

### Formation factor

To determine formation factor, electrical conductivity (see “Physical properties” in the “Methods” chapter) was measured every 10 cm in the working half of the first core of Hole U1339A and every 20 cm in the working halves of Cores 323-U1339A-2H and 3H. Sediment conductivity ranges from 1.37 to 3.70 μS/cm. The highest values were recorded in ash layers, and formation factor generally increases downhole.

## Stratigraphic correlation

The composite depth scale and splice at Site U1339 is complete from 0.0 to 219.06 m CCSF-A (as defined in “Stratigraphic correlation” in the “Methods” chapter). The continuous splice ranges from the top of Core 323-U1339C-1H to the bottom of Section 323-U1339D-21H-6 (Tables T18, T19). One additional core below the splice (Core 323-U1339D-22H) was included in the composite depth framework by extrapolation. Correlations were accomplished using IODP Correlator software (version 1.652, which was abandoned for version 1.65 early during coring and replaced with version 1.655 for Hole U1339D and final site compilation).

The composite (CCSF-A) and splice (CCSF-D) depth scales are based primarily on the stratigraphic correlation of STMSL magnetic susceptibility data collected at 5 cm intervals as the average of two 1 s integrations. These primary correlations were assisted and verified throughout the cored interval with STMSL GRA bulk density data (Fig. F26), NGR (Fig. F27), and STMSL magnetic susceptibility (Fig. F28) measured at 2.5 cm intervals. *P*-wave velocity and noncontact resistivity data were also collected with the WRMSL in part of the cores. However, these data are not illustrated here because they were not useful for correlation—either because of low signal variability or the presence of frequent gas voids (which also compromised STMSL and WRMSL GRA bulk density data). Cores 323-U1339B-1H through 4H were mostly consumed for microbiology sampling after STMSL data collection, so no WRMSL data are available for these cores. STMSL data allow us to assign composite depths to the four cores recovered from Hole U1339B, but because these cores are unavailable for future sampling, they are not included in the splice.

The CCSF-A and CCSF-D depth scales were constructed by assuming that the uppermost sediment (the mudline) in Core 323-U1339C-1H was the sediment/water interface. A mudline was also recovered in Cores 323-U1339A-1H and 323-U1339B-1H, confirming the fidelity of the top of the recovered section. Core 323-U1339C-1H was selected as the anchor in the composite depth scale and is the only core with depths that are the same on the mbsf, CCSF-A, and CCSF-D scales. From this anchor we worked downhole, correlating the stratigraphy on a core-by-core basis using Correlator.

The match between holes is well constrained except for two suspect intervals where overlap between holes was short: 112–123 m CCSF-A (between Cores 323-U1339D-12H, 323-U1339C-12H, and 323-U1339D-13H) and 161–168 m CCSF-A (between Cores 323-U1339D-16H and 323-U1339C-17H). However, the spliced section in these intervals is supported by wireline logging data compared to GRA bulk density core logging data (see “Downhole measurements”).

The splice was constructed primarily from Holes U1339C and U1339D because these were minimally sampled at sea (Fig. F29). Two intervals from Hole U1339B were included in the splice when they were the least disturbed and most representative sections available (Table T19). Within the splice, the composite CCSF-A depth scale is defined as the CCSF-D depth scale. Note that CCSF-D rigorously applies

only to the spliced interval. Intervals outside the splice, although available with CCSF-A composite depth assignments, should not be expected to correlate precisely with fine-scale details within the splice or with other holes because of normal variation in the relative spacing of features in different holes. Such apparent stretching and squeezing may reflect coring artifacts or fine-scale variations in sediment accumulation and preservation at and below the seafloor.

The cumulative offset between mbsf and CCSF-A depth scales is not linear (Fig. F30). The affine growth factor (a measure of the fractional stretching of the composite section relative to the drilled interval; see “**Stratigraphic correlation**” in the “Methods” chapter) at Site U1339 is 1.10 between 0 and 100 mbsf and 1.17 between 100 and 200 mbsf. Larger growth factors in deeper intervals have been observed at other drill sites (for example, ODP Leg 202; Mix, Tiedemann, Blum, et al., 2003). At Site U1339, the larger growth factor at greater depths is consistent with more prominent gas expansion deeper in the section as well as normal expansion associated with release of overburden. Calculation of mass accumulation rates (MARs) based on the CCSF-A or CCSF-D scales should account for the expansion by dividing apparent depth intervals by the appropriate growth factor. After being divided by the growth factor (accounting for the different depth intervals), this scaled depth scale should be referred to as CCSF-B.

The deepest core at Site U1339 (Core 323-U1339D-22H) is not tied to the splice. Rather than appending this core below Core 323-U1339D-21H, we calculated its CCSF-A depth and affine value by extrapolating the value from the overlying core by a growth factor of 1.17.

## Downhole measurements

### Logging operations

Downhole logging of Hole U1339D started after APC coring to a total depth of 200 m DSF ended on 20 July 2009 at 0930 h (all times are ship local time, UTC – 11 h). In preparation for logging, the hole was conditioned with a ~50 bbl sweep of sea gel (attapulgitite, ~9 ppg), a go-devil was pumped through the drill string to open and lock the lockable flapper valve, and the bit was raised to the logging depth of 84 m DSF (1962 m DRF).

Two tool strings were deployed in Hole U1339D: the triple combo and the FMS-sonic combination (for tool and measurement acronyms, see “**Downhole measurements**” in the “Methods” chapter). Assem-

bly of the triple combo tool string began at 1210 h, and the string was run in hole (RIH) at 1330 h. After some testing of the wireline heave compensator (WHC), the tool string reached the bottom of the hole (2080 m wireline log depth below rig floor [WRF]) and a first uphole logging pass started at 1550 h at a speed of 900 ft/h. This pass was completed when the bottom of the string reached 2000 m WRF at 1610 h. The caliper arm would not close while the tool was being lowered to record the main pass, presumably because of debris underneath it. Some time was spent attempting to close the caliper arm by reentering the pipe to force the closing mechanism; however, the arm closed by itself before it was forced shut. After establishing that there was no apparent damage to the arm, the tool string was lowered back to the bottom of the hole and a second uphole pass started at 1647 h. This second pass ended when the tool string crossed the seafloor, marked by a drop in natural radioactivity at 1876 m WRF, 2.4 m shallower than the drillers seafloor depth at 1878.4 m DRF. The triple combo tool string reached the rig floor at 1848 h and was rigged down at 1935 h.

The FMS-sonic tool string was then rigged up and RIH at 2010 h. It reached the bottom of the hole at 2080 m WRF at 2130 h, and the first pass started at the logging speed of 900 ft/h. The pass was completed at 2150 h, with the bottom of the 35 m long tool string at 2005 m WRF. After the tool string returned to the bottom of the hole, the second pass started at 2200 h and ended at 2250 h after the seafloor was detected at 1875 m WRF. The tool string was back on the rig floor at 0000 h 21 July, and rig-down was complete at 0110 h.

### Downhole log data quality

Figures F31 and F32 show a summary of the downhole logging data acquired in Hole U1339D. These data were processed and converted to depth below seafloor and matched to depths between different logging runs. The resulting depth scale is wireline log matched depth below seafloor (WMSF) (see “**Downhole measurements**” in the “Methods” chapter).

The first indications of the overall quality of the logs are the size and shape of the borehole measured by the calipers. The hole size measured by the Hostile Environment Litho-Density Sonde caliper during the triple combo run and by the FMS arms is shown in the first column of Figures F31 and F32, respectively. For safety, the caliper and the FMS arms were closed before the top of the tool string reached the bottom of the pipe, but the data recorded below this depth indicate good hole conditions and only minor excursions from the nominal size of the drill bit.

The quality of the logs can also be assessed by comparing them with core measurements in the same hole or by looking at the repeatability of the measurements acquired in different runs. Figure F31 shows a comparison of the gamma ray and density logs with the NGR and GRA measurements on Hole U1339D cores and with MAD measurements made on samples from Site U1339. All data are in good agreement, which should allow for reliable core-log integration, but there is an apparent depth offset of ~3 m between the track and the log data, likely a result of different identifications of the seafloor. All logs were referenced to the seafloor depth of 1875 m WRF identified during the last pass of the FMS-sonic tool string. Comparison of the gamma ray logs measured during the main pass of the two runs shows excellent repeatability (Fig. F32).

Resistivity values measured by the spherically focused resistivity (SFLU) tool are lower than those recorded by induction measurements (e.g., medium and deep induction phasor-processed resistivity [IMPH and IDPH] in Fig. F31), probably because of current loss at the electrodes. The higher induction resistivities are closer to values typically measured in deep-sea sediments.

The high coherence in sonic waveforms used to derive compressional velocity suggests that, despite the closeness of the formation velocity to the sound velocity in the borehole fluid (~1500 m/h), the Dipole Sonic Imager was able to capture compressional wave arrivals and measure a reliable  $V_p$  profile over the entire open interval logged. Additional post-cruise processing will, however, be necessary to derive  $V_s$  logs from the recorded dipole waveforms.

Finally, the examples of FMS images in Figure F32 show that some of the buttons on one arm were not working properly, generating a continuous streak along most of the interval logged. When the FMS-sonic tool string returned to the surface, these buttons appeared to be covered with an insulating substance, which was then cleaned off. The overall quality of the images was not significantly affected by the faulty buttons, and the two passes provide a high-resolution image of the borehole wall.

### Logging stratigraphy and correlation

The downhole log measurements of bulk density, porosity, and electrical resistivity in Hole U1339D correlate very well (Fig. F31). Without significant variations in the overall composition of the mineral matrix, changes in sediment composition result in variations of porosity that affect bulk density and resistivity in a similar manner. These measurements in Hole U1339D also mostly correlate with the gamma

ray logs over the entire interval logged, with low variability reflecting the mostly uniform nature of the formation logged. Despite this uniformity, some trends express changes in the sedimentation history at this site, such as the parallel decrease with depth in gamma radiation, density, and resistivity from 86 to 102 m WMSF, which is typical of a retrograding fining-upward sequence. Similar sequences, although less clearly defined, seem to define the general trend of the logs downhole.

The downhole variations of gamma ray radioactivity (Fig. F33) are controlled by the sediment content of naturally occurring radioactive elements (K, U, and Th). Computed gamma ray (or gamma ray without uranium) is a more accurate measure of clay content than total gamma ray (Rider, 1996), which can be influenced by factors such as organic matter or detrital minerals. The most significant feature in the gamma ray logs is the increase at ~142 m WMSF, which is associated with an increase in the three radioactive components and a peak in uranium. The peak in uranium can be related to the occurrence of dolostones observed in the cores in this interval.

### Temperature measurements

Downhole temperature measurements at Site U1339 include one third-generation advanced piston corer temperature tool (APCT-3) deployment in Hole U1339A and four APCT-3 deployments in Hole U1339B (Table T20). During the deployment in Hole U1339A, the APCT-3 failed to couple properly with the formation and the recorded data could not be used. The measured temperatures range from 3.65°C at 23.0 m DSF to 12.83°C at 158.0 m DSF and closely fit a linear geothermal gradient of 68.0°C/km (Fig. F34). The record for Core 323-U1339B-13H displays some irregularities in temperature decay after penetration and was not used to calculate this gradient. The temperature at the seafloor was 2.1°C based on the average of the measurements at the mudline during all APCT-3 deployments. A simple estimate of heat flow can be obtained from the product of the geothermal gradient by the average thermal conductivity (0.80 W/[m·K]; see “Physical properties”), which gives a value of 54.4 mW/m<sup>2</sup>, within the range of previous measurement in the area (the global heat flow database of the international heat flow commission can be found at [www.heat-flow.und.edu/index.html](http://www.heat-flow.und.edu/index.html)).

### References

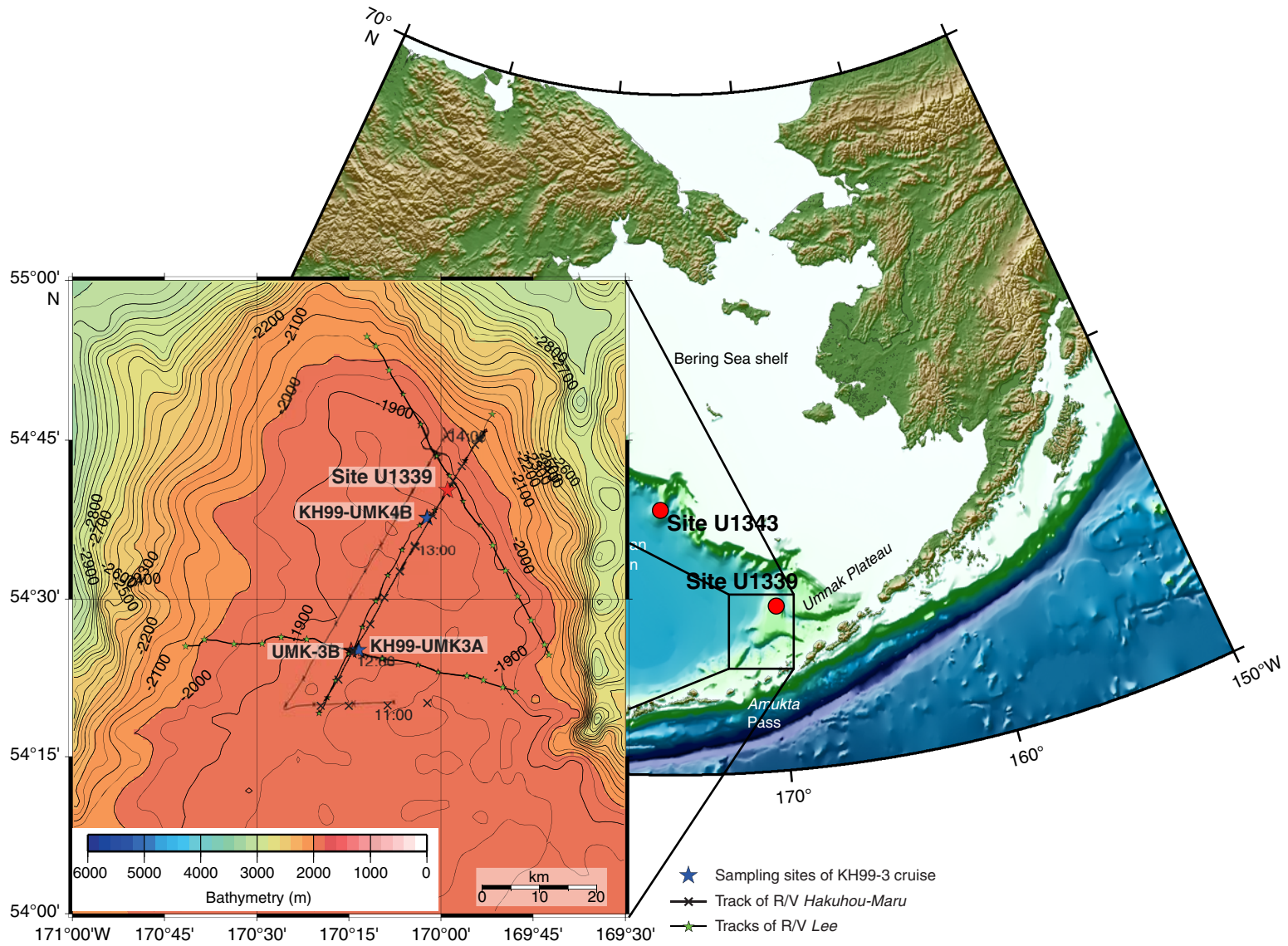
- Asahi, H., and Takahashi, K., 2007. A 9-year time-series of planktonic foraminifer fluxes and environmental change in the Bering Sea and the central subarctic

- Pacific Ocean, 1990–1999. *Prog. Oceanogr.*, 72(4):343–363. doi:10.1016/j.pocean.2006.03.021
- Barron, J.A., and Gladenkov, A.Y., 1995. Early Miocene to Pleistocene diatom stratigraphy of Leg 145. In Rea, D.K., Basov, I.A., Scholl, D.W., and Allan, J.F. (Eds.), *Proc. ODP, Sci. Results*, 145: College Station, TX (Ocean Drilling Program), 3–19. doi:10.2973/odp.proc.sr.145.101.1995
- Bé, A.W.H., and Tolderlund, D.S., 1971. Distribution and ecology of living planktonic foraminifera in surface waters of the Atlantic and Indian Oceans. In Funnel, B.M., and Riedel, W.R. (Eds.), *The Micropaleontology of Oceans*: Cambridge (Cambridge Univ. Press), 105–149.
- Blanchet, C.L., Thouveny, N., and Vidal, L., 2009. Formation and preservation of greigite (Fe<sub>3</sub>S<sub>4</sub>) in sediments from the Santa Barbara Basin: implications for paleoenvironmental changes during the past 35 ka. *Paleoceanography*, 24(2):PA2224. doi:10.1029/2008PA001719
- Bubenshchikova, N., Nürnberg, D., Lembke-Jene, L., and Pavlova, G., 2008. Living benthic foraminifera of the Okhotsk Sea: faunal composition, standing stocks and microhabitats. *Mar. Micropaleontol.*, 69(3–4):314–333. doi:10.1016/j.marmicro.2008.09.002
- Butt, A., 1980. Biostratigraphic and paleoenvironmental analyses of the sediments at the Emperor Seamounts, DSDP Leg 55, Northwestern Pacific: Cenozoic foraminifera. In Jackson, E.D., Koizumi, I., et al., *Init. Repts. DSDP*, 55: Washington, DC (U.S. Govt. Printing Office), 289–325. doi:10.2973/dsdp.proc.55.108.1980
- Carey, S., 1997. Influence of convective sedimentation on the formation of widespread tephra fall layers in the deep sea. *Geology*, 25(9):839–842. doi:10.1130/0091-7613(1997)025<0839:IOCSOT>2.3.CO;2
- Hamel, D., de Vernal, A., Gosselin, M., and Hillaire-Marcel, C., 2002. Organic-walled microfossils and geochemical tracers: sedimentary indicators of productivity changes in the North Water and northern Baffin Bay during the last centuries. *Deep-Sea Res., Part II*, 49(22–23):5277–5295. doi:10.1016/S0967-0645(02)00190-X
- Head, M.J., Harland, R., and Matthiessen, J., 2001. Cold marine indicators of the late Quaternary: the new dinoflagellate cyst genus *Islandinium* and related morphotypes. *J. Quat. Sci.*, 16(7):621–636. doi:10.1002/jqs.657
- Jacobson, D.M., and Anderson, D.M., 1986. Thecate heterotrophic dinoflagellates: feeding behavior and mechanisms. *J. Phycol.*, 22(3):249–258. doi:10.1111/j.1529-8817.1986.tb00021.x
- Kaiho, K., 1994. Benthic foraminiferal dissolved-oxygen index and dissolved-oxygen levels in the modern ocean. *Geology*, 22(8):719–722. doi:10.1130/0091-7613(1994)022<0719:BFDOIA>2.3.CO;2
- Kamikuri, S., Nishi, H., and Motoyama, I., 2007. Effects of late Neogene climatic cooling on North Pacific radiolarian assemblages and oceanographic conditions. *Palaeogeogr., Palaeoclimatol., Palaeoecol.*, 249(3–4):370–392. doi:10.1016/j.palaeo.2007.02.008
- Katsuki, K., and Takahashi, K., 2005. Diatoms as paleoenvironmental proxies for seasonal productivity, sea-ice and surface circulation in the Bering Sea during the late Quaternary. *Deep-Sea Res., Part II*, 52(16–18):2110–2130. doi:10.1016/j.dsr2.2005.07.001
- Khusid, T.A., Basov, I.A., Gorbarenko, S.A., and Chekhovskaya, M.P., 2006. Benthic foraminifera in upper Quaternary sediments of the southern Bering Sea: distribution and paleoceanographic interpretations. *Stratigr. Geol. Correl.*, 14(5):538–548. doi:10.1134/S0869593806050066
- Ling, H.Y., 1973a. Radiolaria: Leg 19 of the Deep Sea Drilling Project. In Creager, J.S., Scholl, D.W., et al., *Init. Repts. DSDP*, 19: Washington, DC (U.S. Govt. Printing Office), 777–797. doi:10.2973/dsdp.proc.19.128.1973
- Ling, H.Y., 1973b. Silicoflagellates and ebridians from Leg 19. In Creager, J.S., Scholl, D.W., et al., *Init. Repts. DSDP*, 19: Washington (U.S. Govt. Printing Office), 751–775. doi:10.2973/dsdp.proc.19.127.1973
- Ling, H.Y., 1992. Late Neogene silicoflagellates and ebridians from Leg 128, Sea of Japan. In Pisciotto, K.A., Ingle, J.C., Jr., von Breymann, M.T., and Barron, J., et al. (Eds.), *Proc. ODP, Sci. Results*, 127/128, Pt. 1: College Station, TX (Ocean Drilling Program), 237–248. doi:10.2973/odp.proc.sr.127128-1.126.1992
- Lund, S., Stoner, J.S., Channell, J.E.T., and Acton, G., 2006. A summary of Brunhes paleomagnetic field variability recorded in Ocean Drilling Program cores. In Sager, W.W., Acton, G.D., Clement, B.M., and Fuller, M. (Eds.), *ODP Contributions to Paleomagnetism*. Phys. Earth Planet. Int., 156(3–4):194–204. doi:10.1016/j.pepi.2005.10.009
- Martini, E., 1971. Standard Tertiary and Quaternary calcareous nannoplankton zonation. In Farinacci, A. (Ed.), *Proc. 2nd Int. Conf. Planktonic Microfossils Roma*: Rome (Ed. Tecnosci.), 2:739–785.
- Mix, A.C., Tiedemann, R., Blum, P., et al., 2003. *Proc. ODP, Init. Repts.*, 202: College Station, TX (Ocean Drilling Program). doi:10.2973/odp.proc.ir.202.2003
- Mudie, P.J., 1987. Palynology and dinoflagellate biostratigraphy of Deep Sea Drilling Project Leg 94, Sites 607 and 611, North Atlantic Ocean. In Ruddiman, W.F., Kidd, R.B., Thomas, E., et al., *Init. Repts. DSDP*, 94: Washington, DC (U.S. Govt. Printing Office), 785–812. doi:10.2973/dsdp.proc.94.118.1987
- Okada, H., and Honjo, S., 1973. The distribution of oceanic coccolithophorids in the Pacific. *Deep-Sea Res., Part A*, 20:355–374.
- Okazaki, Y., Takahashi, K., Asahi, H., Katsuki, K., Hori, J., Yasuda, H., Sagawa, Y., and Tokuyama, H., 2005. Productivity changes in the Bering Sea during the late Quaternary. *Deep-Sea Res., Part II*, 52(16–18):2150–2162. doi:10.1016/j.dsr2.2005.07.003
- Radi, T., and de Vernal, A., 2004. Dinocyst distribution in surface sediments from the northeastern Pacific margin (40–60°N) in relation to hydrographic conditions, productivity and upwelling. *Rev. Palaeobot. Palynol.*, 128(1–2):169–193. doi:10.1016/S0034-6667(03)00118-0
- Rider, M.H., 1996. *The Geological Interpretation of Well Logs* (2nd ed.): Caithness (Whittles Publ.).
- Rochon, A., de Vernal, A., Turon, J.L., Mathiessen, J., and Head, M.J., 1999. Distribution of recent dinoflagellate cysts in surface sediments from the North Atlantic

- Ocean and adjacent seas in relation to sea-surface parameters. *Am. Assoc. Strat. Palynol. Found. Contrib. Ser.*, Vol. 35.
- Sancetta, C., 1982. Distribution of diatom species in surface sediments of the Bering and Okhotsk seas. *Micropaleontology*, 28(3):221–257. doi:10.2307/1485181
- Scholl, D.W., and Creager, J.S., 1973. Geologic synthesis of Leg 19 (DSDP) results; far North Pacific, and Aleutian Ridge, and Bering Sea. In Creager, J.S., Scholl, D.W., et al., *Init. Repts. DSDP*, 19: Washington, DC (U.S. Govt. Printing Office), 897–913. doi:10.2973/dsdp.proc.19.137.1973
- Takahashi, K., 2005. The Bering Sea and paleoceanography. *Deep-Sea Res., Part II*, 52(16–18):2080–2091. doi:10.1016/j.dsr2.2005.08.003
- Takahashi, K., Ravelo, A.C., and Alvarez Zarikian, C.A., 2009. Pliocene–Pleistocene paleoceanography and climate history of the Bering Sea. *IODP Sci. Prosp.*, 323. doi:10.2204/iodp.sp.323.2009
- Tanaka, S., and Takahashi, K., 2005. Late Quaternary paleoceanographic changes in the Bering Sea and the western subarctic Pacific based on radiolarian assemblages. *Deep-Sea Res., Part II*, 52(16–18):2131–2149. doi:10.1016/j.dsr2.2005.07.002
- VanLaningham, S., Pisias, N.G., Duncan, R.A., and Clift, P.D., 2009. Glacial–interglacial sediment transport to the Meiji Drift, northwest Pacific Ocean: evidence for timing of Beringian outwashing. *Earth Planet. Sci. Lett.*, 277(1–2):64–72. doi:10.1016/j.epsl.2008.09.033
- Von Quillfeldt, C.H., Ambrose, W.G., Jr., and Clough, L.M., 2003. High number of diatom species in first-year ice from the Chukchi Sea. *Polar Biol.*, 26(12):806–818. doi:10.1007/s00300-003-0549-1
- Yanagisawa, Y., and Akiba, F., 1998. Refined Neogene diatom biostratigraphy for the northwest Pacific around Japan, with an introduction of code numbers for selected diatom biohorizons. *J. Geol. Soc. Jpn.*, 104:395–414.

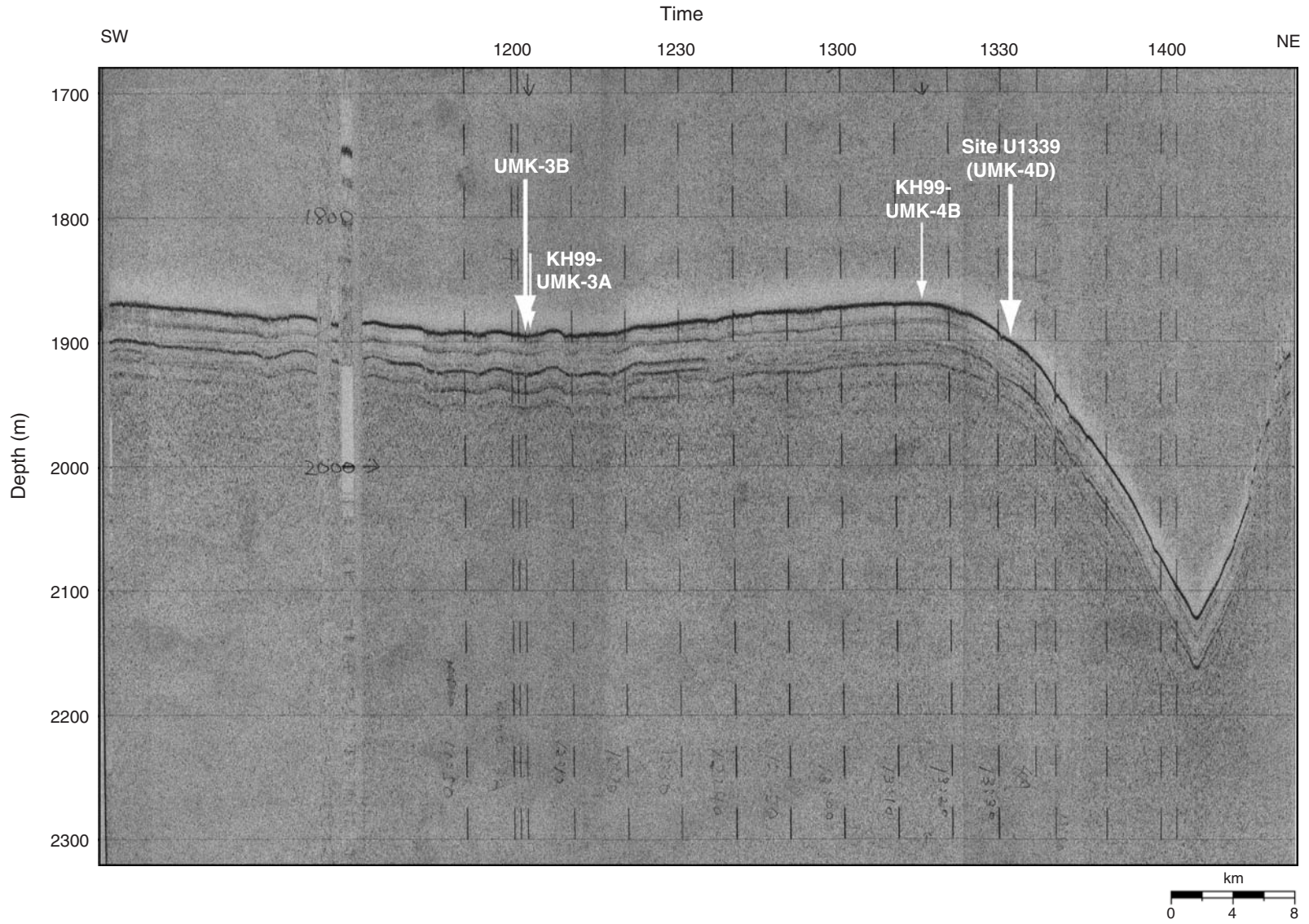
**Publication:** 15 March 2011  
**MS 323-103**

Figure F1. Location map for Site U1339 on Umnak Plateau.





**Figure F2.** 3.5 kHz subbottom profile survey from *Hakuhou-Maru* Cruise KH99-3 around Site U1339. Horizontal axis of ship time corresponds to time annotation in the swath bathymetric map along a southwest–northeast line.





**Figure F3.** Close-up seismic profile around Site U1339. **A.** U.S. Geological Survey (USGS) *Lee* Cruise L6-80 Line 2, a southwest–northeast line across Site U1339. **B.** USGS *Lee* Cruise L6-80 Line 5. BSR = bottom-simulating reflector.

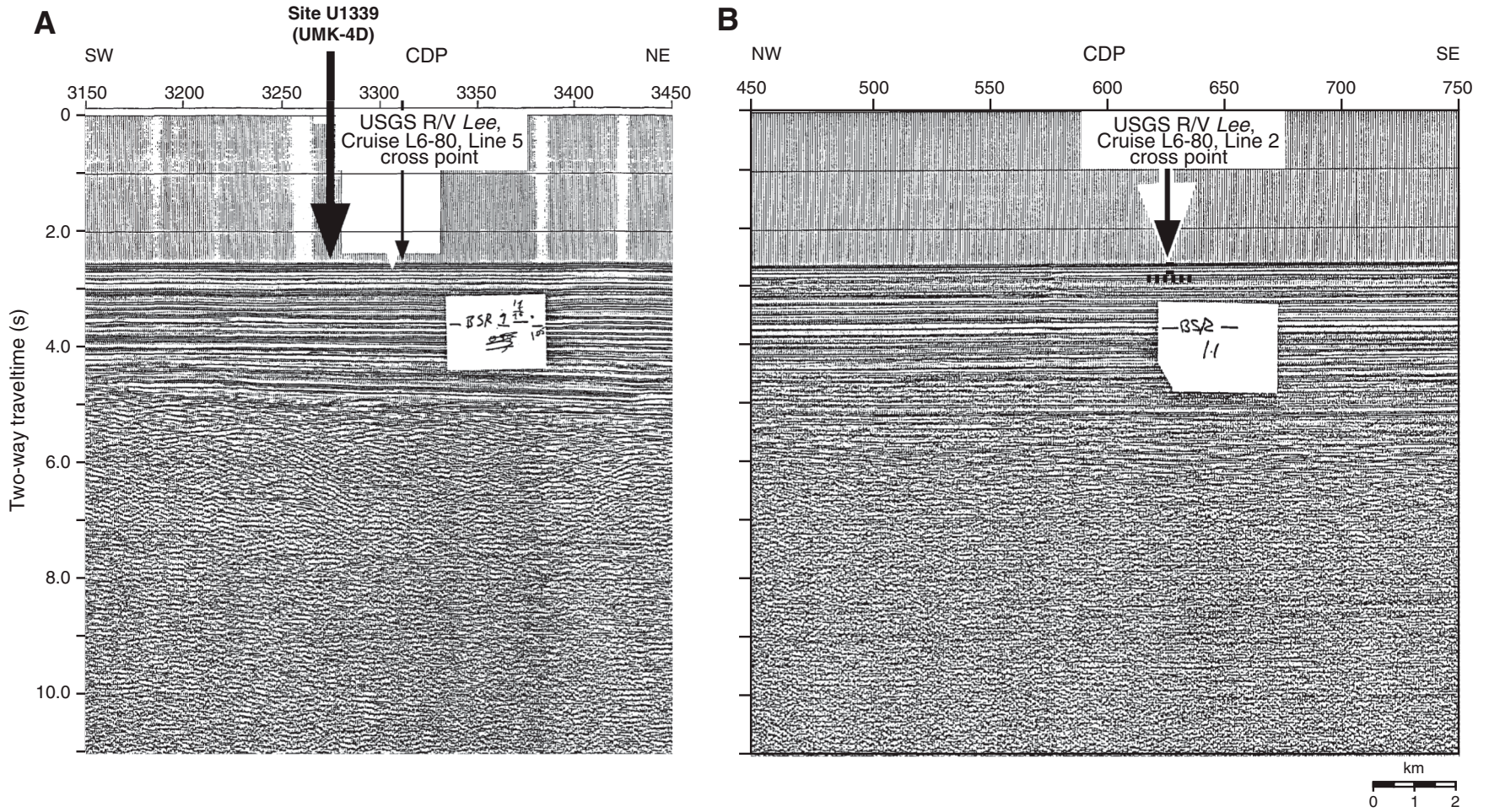


**Figure F4.** Example of reconstructed past surface water conditions and sea ice extent during the Last Glacial Maximum in the Bering Sea (Katsuki and Takahashi, 2005). Dark gray area = paleocontinental shelf, light gray area = paleobathymetry between 400 and 900 m isobaths. Double black arrows = stronger flow than today, gray arrows = weaker flow than today. Circles = cores examined by Katsuki and Takahashi (2005), stars = cores reported from various sources as cited in Katsuki and Takahashi (2005). ES = Emperor Seamount.

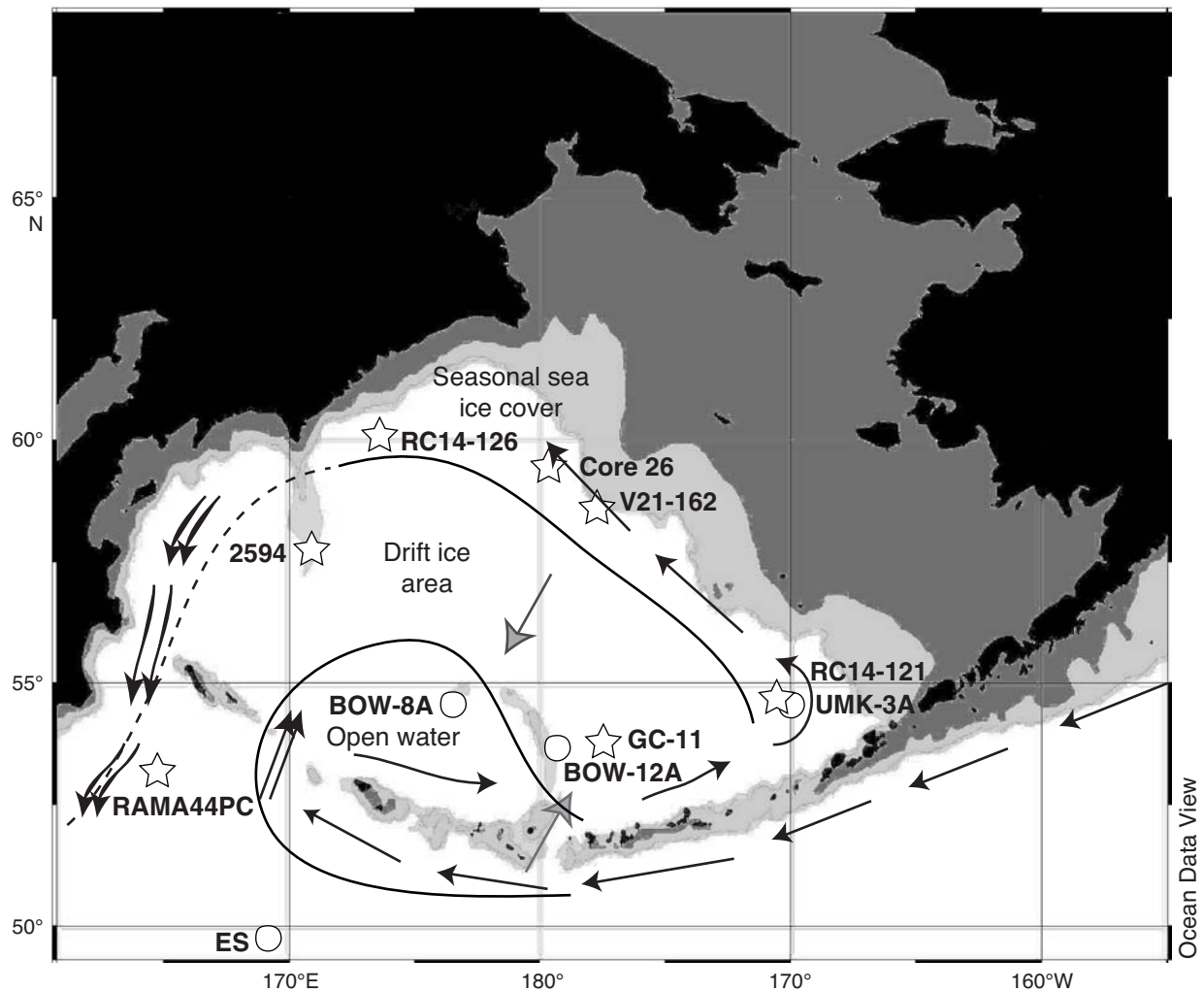




**Figure F5.** Summary of lithology, structures, accessories, microfossils, and physical properties, Hole U1339A. See legend in Figure F6 in the “Methods” chapter. Soft-sed = soft-sediment, auth = authigenic, calc = calcareous, NGR = natural gamma radiation, GRA = gamma ray attenuation, sed rate = sedimentation rate.

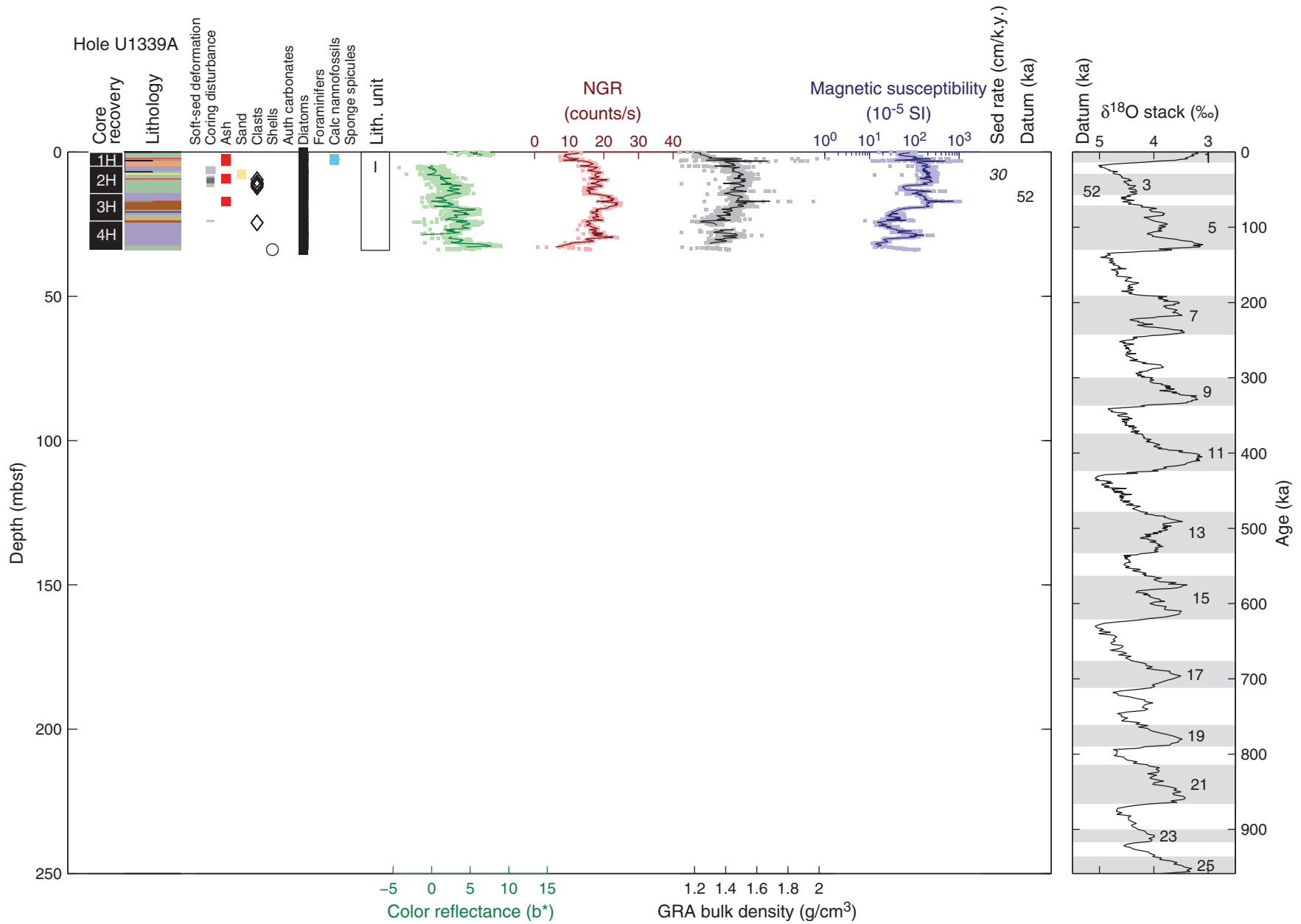




**Figure F6.** Summary of lithology, structures, accessories, microfossils, and physical properties, Hole U1339B. See legend in Figure F6 in the “Methods” chapter. Soft-sed = soft-sediment, auth = authigenic, calc = calcareous, NGR = natural gamma radiation, GRA = gamma ray attenuation, sed rate = sedimentation rate.

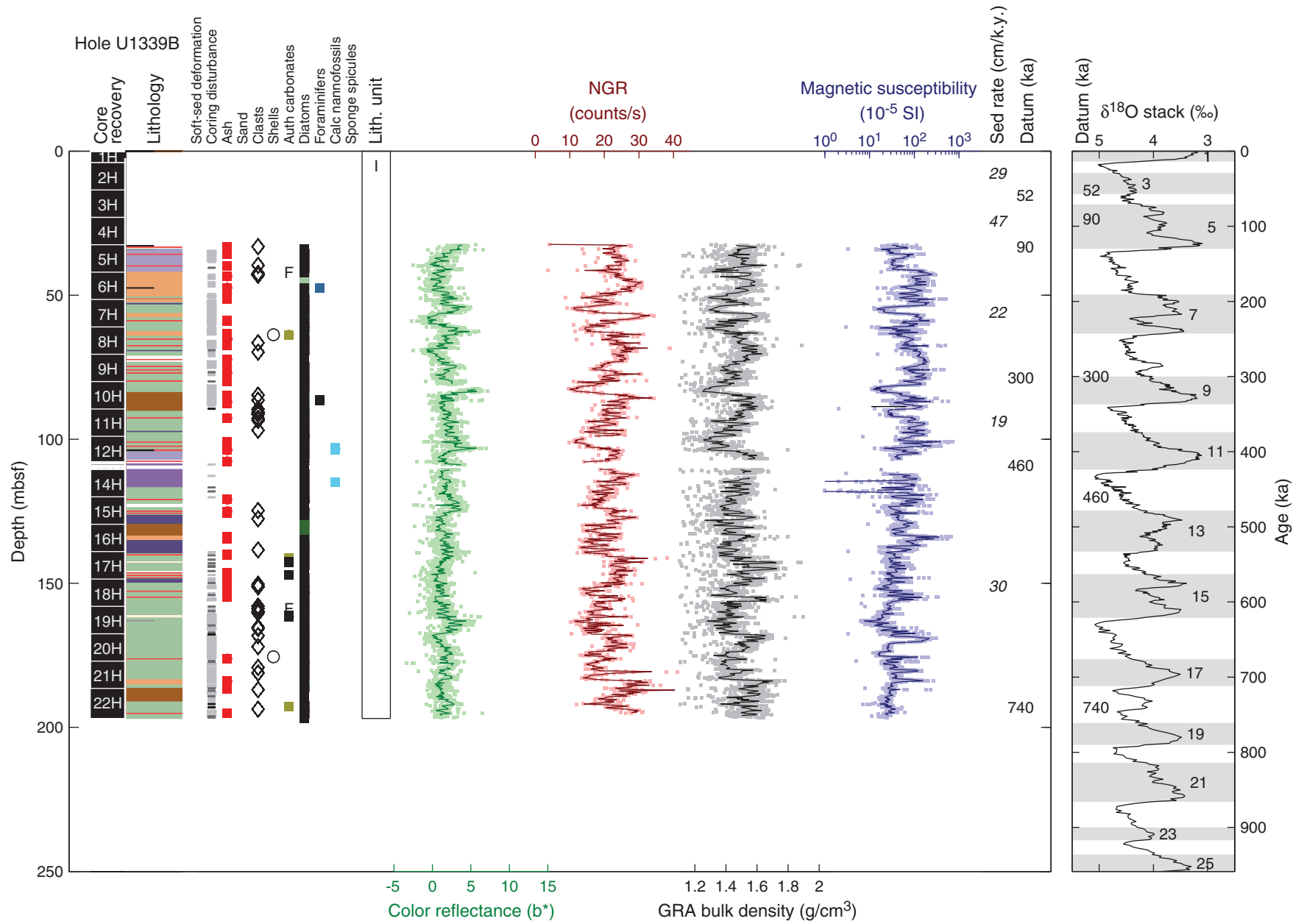




**Figure F7.** Summary of lithology, structures, accessories, microfossils, and physical properties, Hole U1339C. See legend in Figure F6 in the “Methods” chapter. Soft-sed = soft-sediment, auth = authigenic, calc = calcareous, NGR = natural gamma radiation, GRA = gamma ray attenuation, sed rate = sedimentation rate.

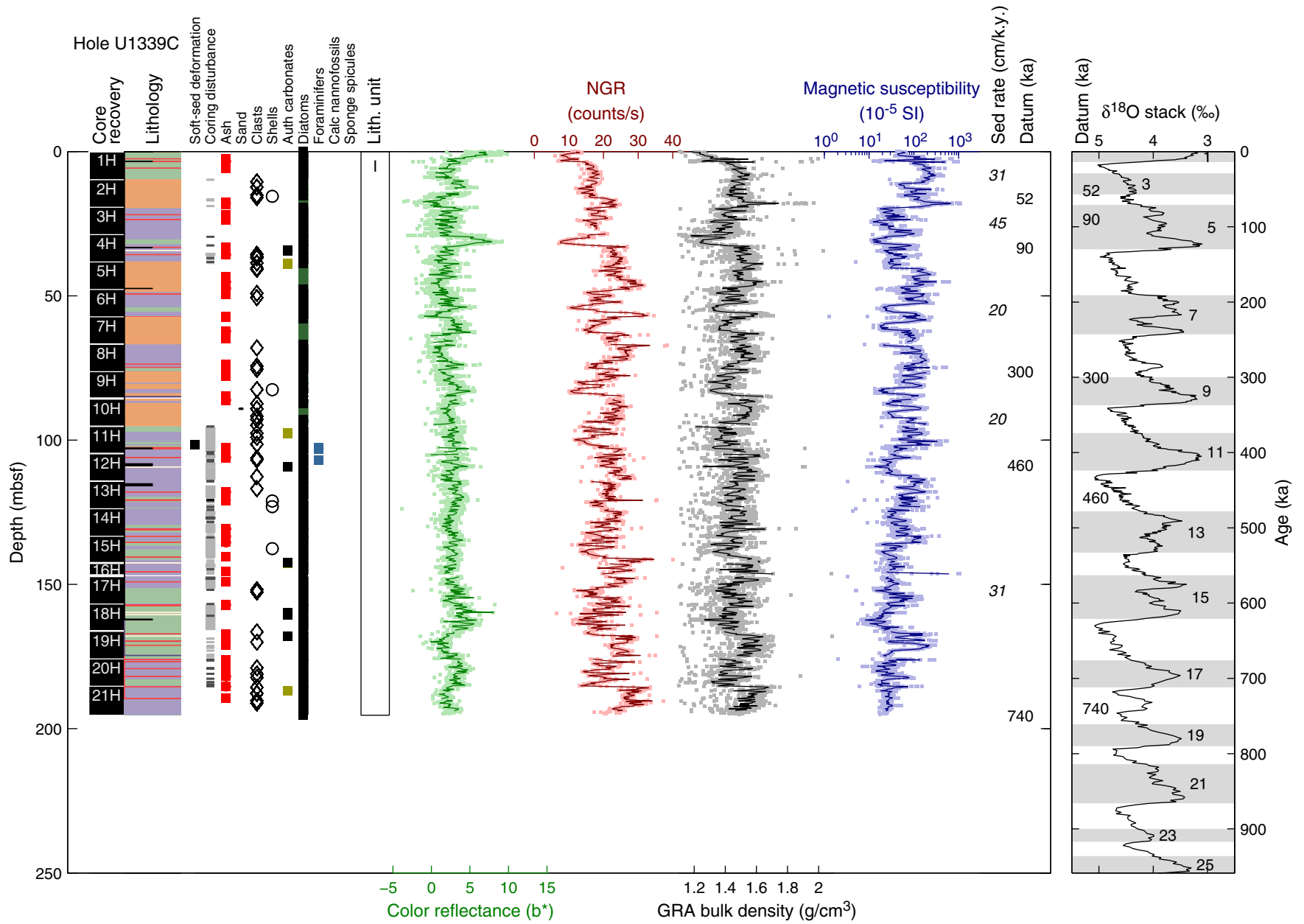




**Figure F8.** Summary of lithology, structures, accessories, microfossils, and physical properties, Hole U1339D. See legend in Figure F6 in the “Methods” chapter. Soft-sed = soft-sediment, auth = authigenic, calc = calcareous, NGR = natural gamma radiation, GRA = gamma ray attenuation, sed rate = sedimentation rate.

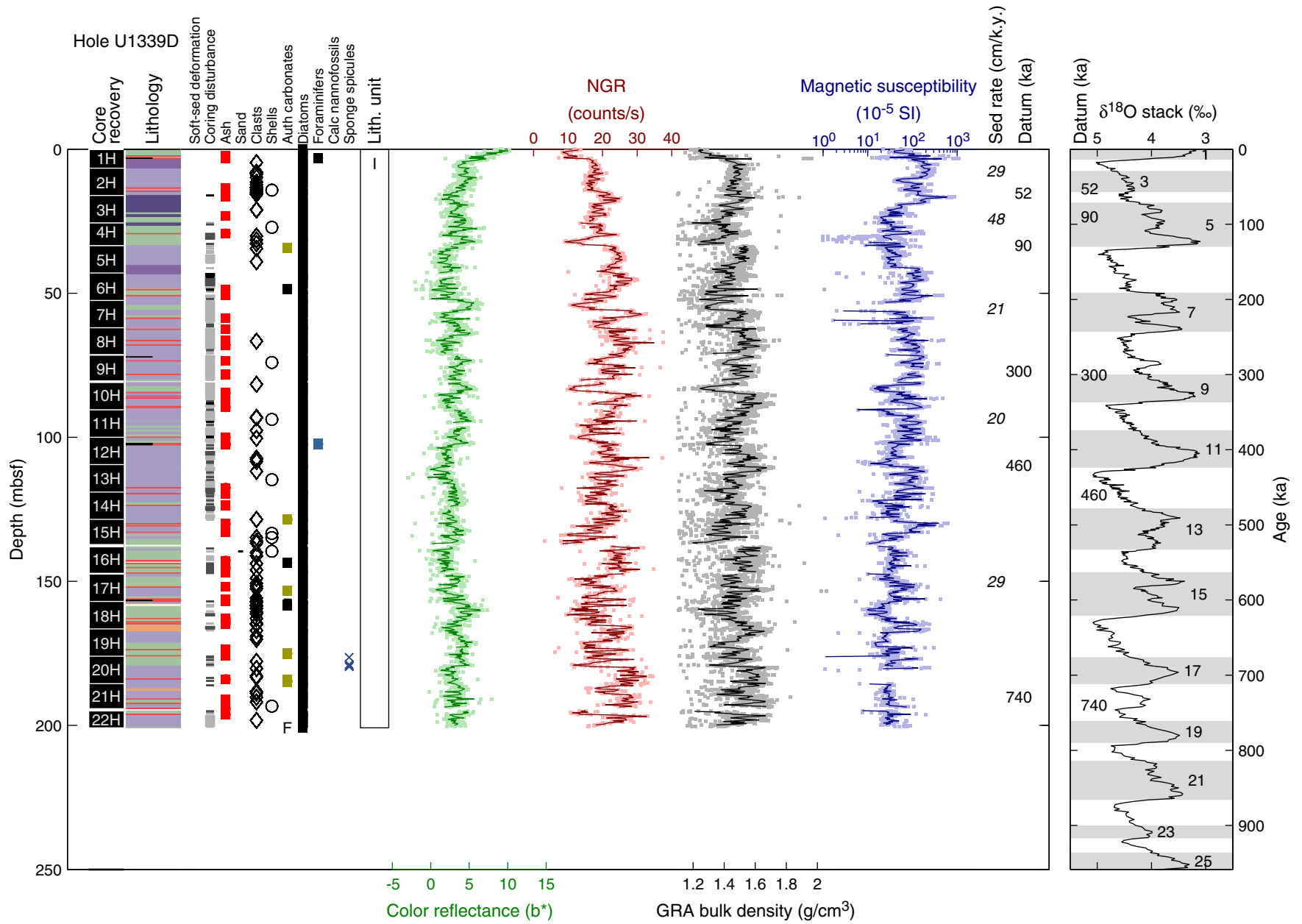


**Figure F9.** Image scans of black ash layers and laminated sediments. **A.** Interval 323-U1339A-1H-3, 0–23 cm. **B.** Interval 323-U1339B-12H-4, 111–145 cm. Note that the laminated interval overlies the ash layer in A, whereas three laminated intervals occur interbedded with three ash layers in B, which also shows an example of graded bedding.

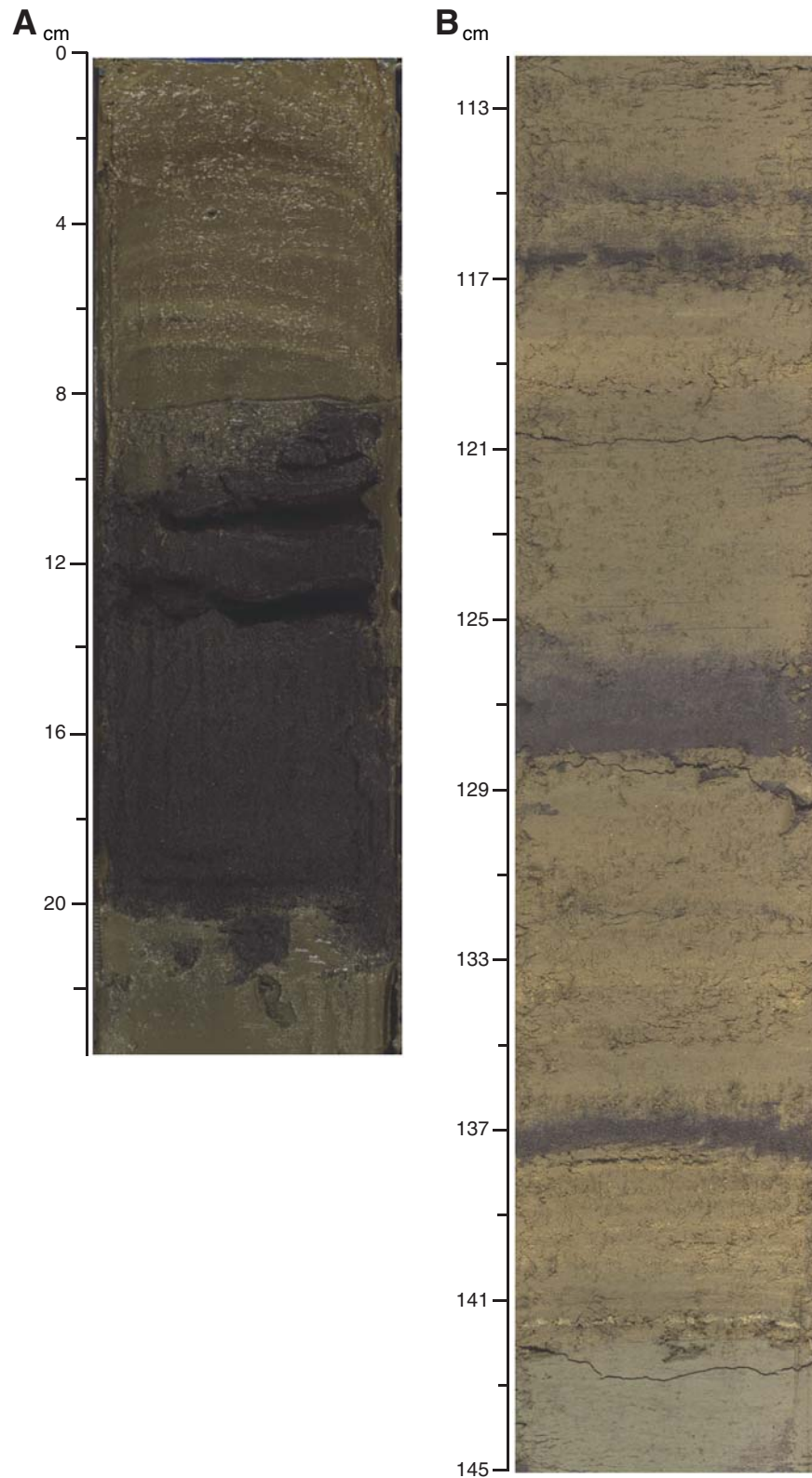
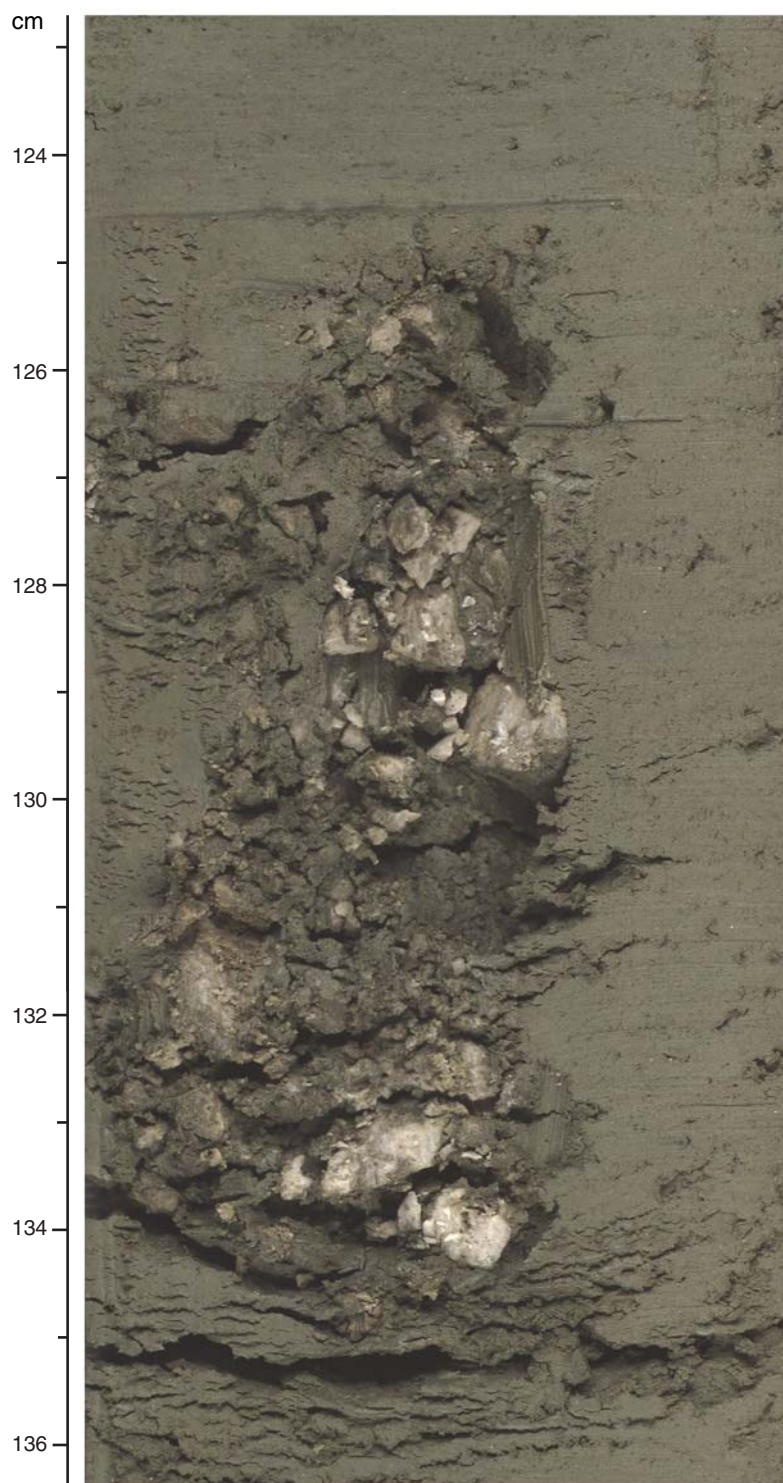
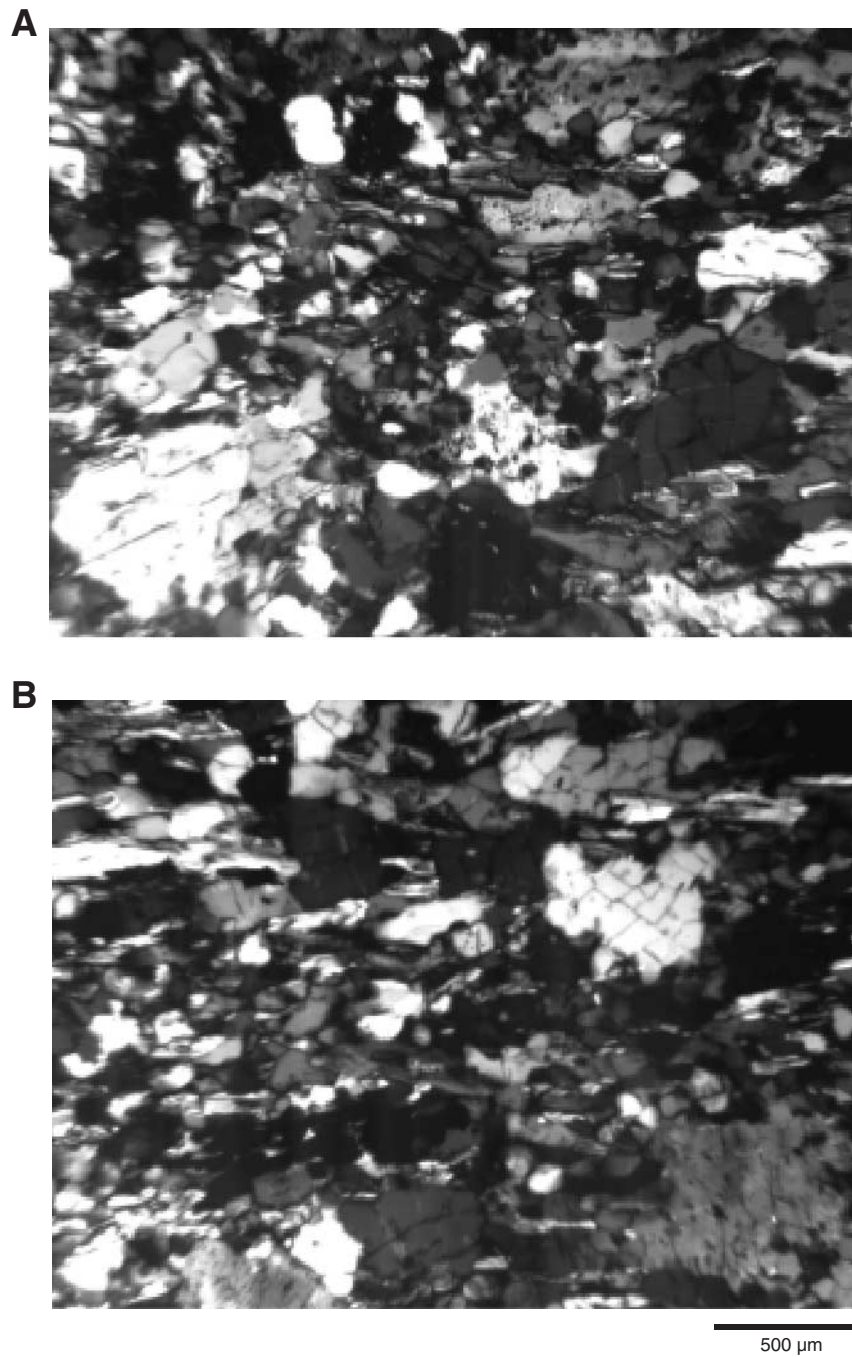


Figure F10. Photograph of gravel (IRD) from interval 323-U1339D-21H-2, 123–136 cm.



**Figure F11.** Photomicrographs of IRD metasandstone pebbles in (A) Samples 323-U1339A-10H-1, 0–2 cm, and (B) 323-U1339A-2H-4, 22–26 cm (cross-polarized light).



**Figure F12.** Thin section photomicrographs of a dolostone layer in Sample 323-U1339B-5H-7, 17–21 cm, under (A) cross-polarized and (B) plane-polarized light.

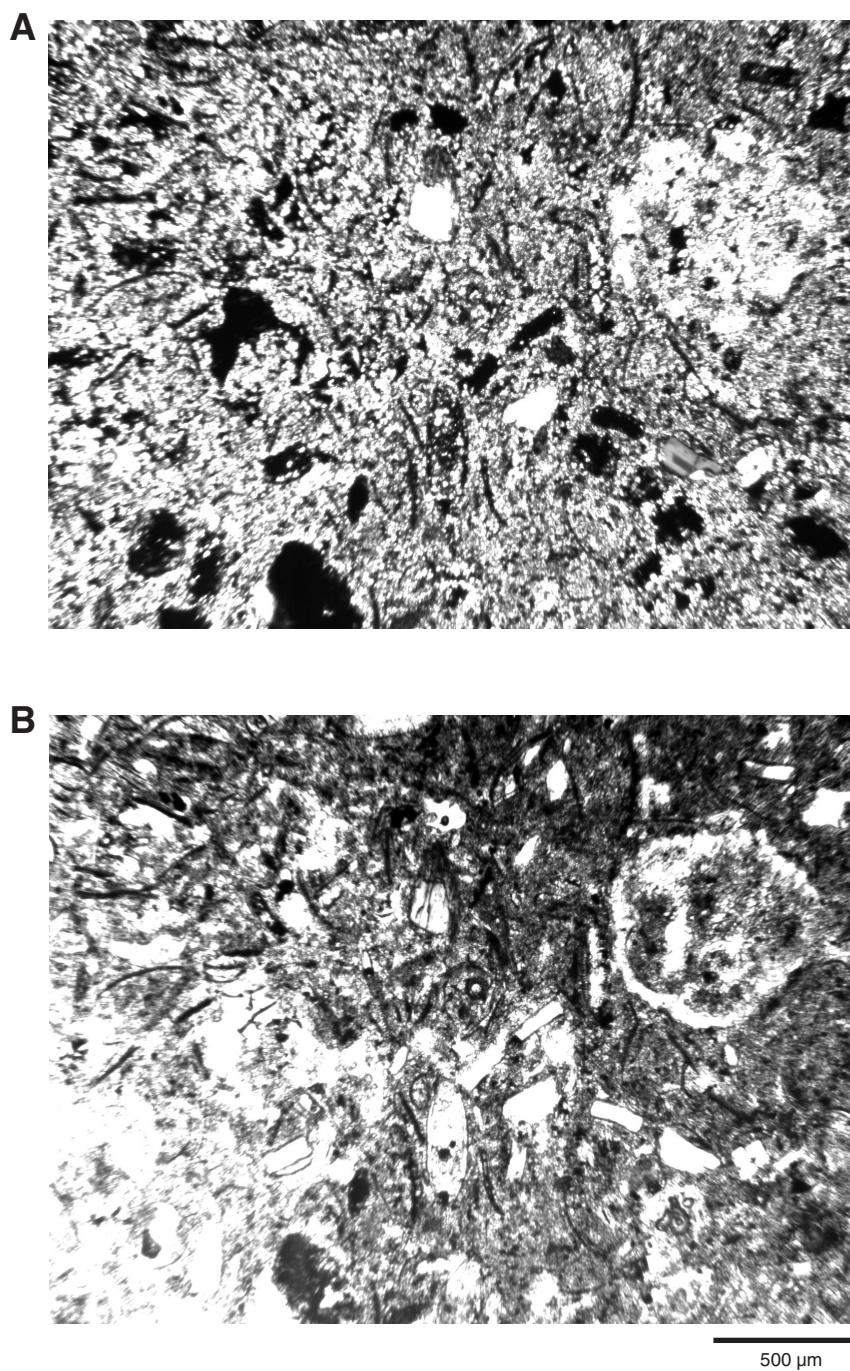


**Figure F13.** Results of onboard X-ray diffractometric analysis of Sample 323-U1339B-5H-2, 12–14 cm, demonstrating the preponderance of dolomite minerals in this layer. A = albite, D = dolomite, H = halite, Q = quartz, I = illite.

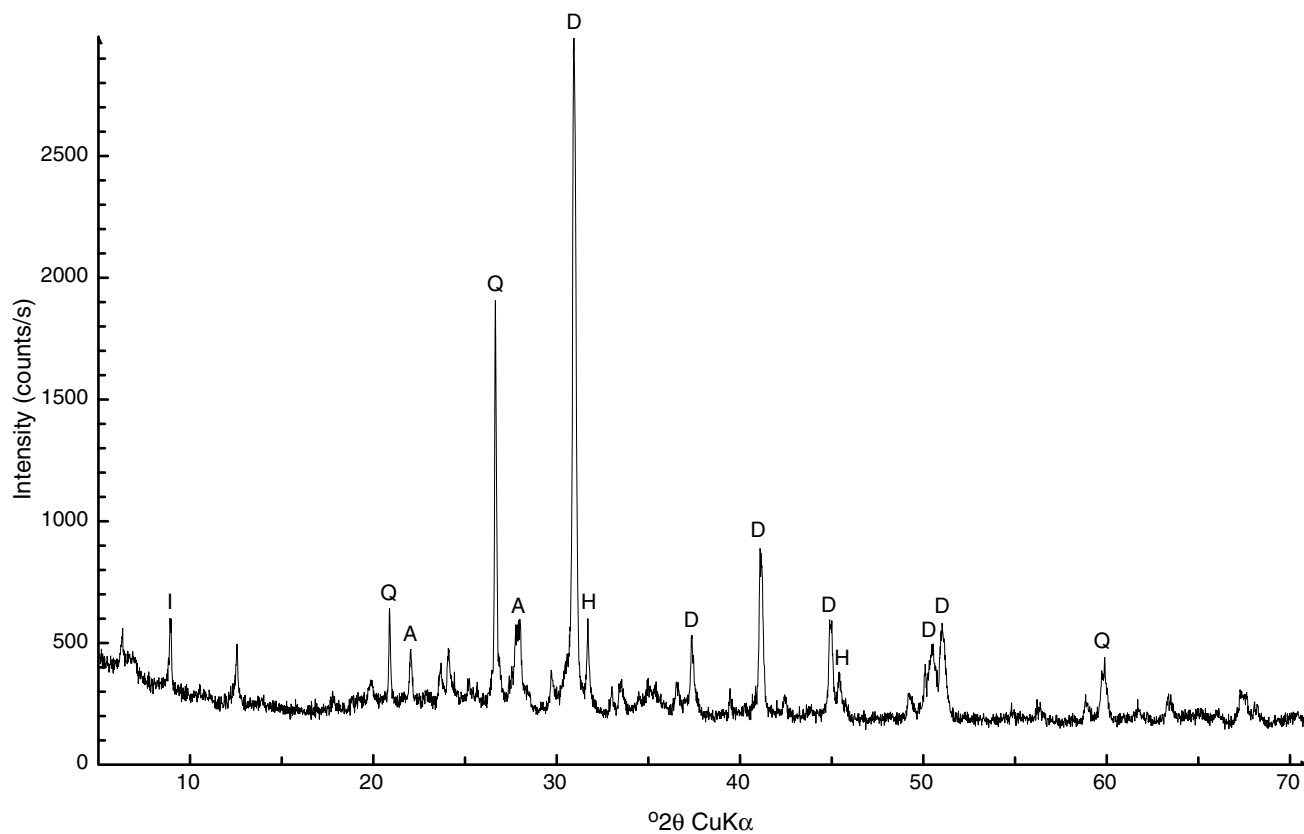


**Figure F14.** Age-depth plot for Site U1339 showing biostratigraphic datums based on radiolarians, diatoms, and silicoflagellates.

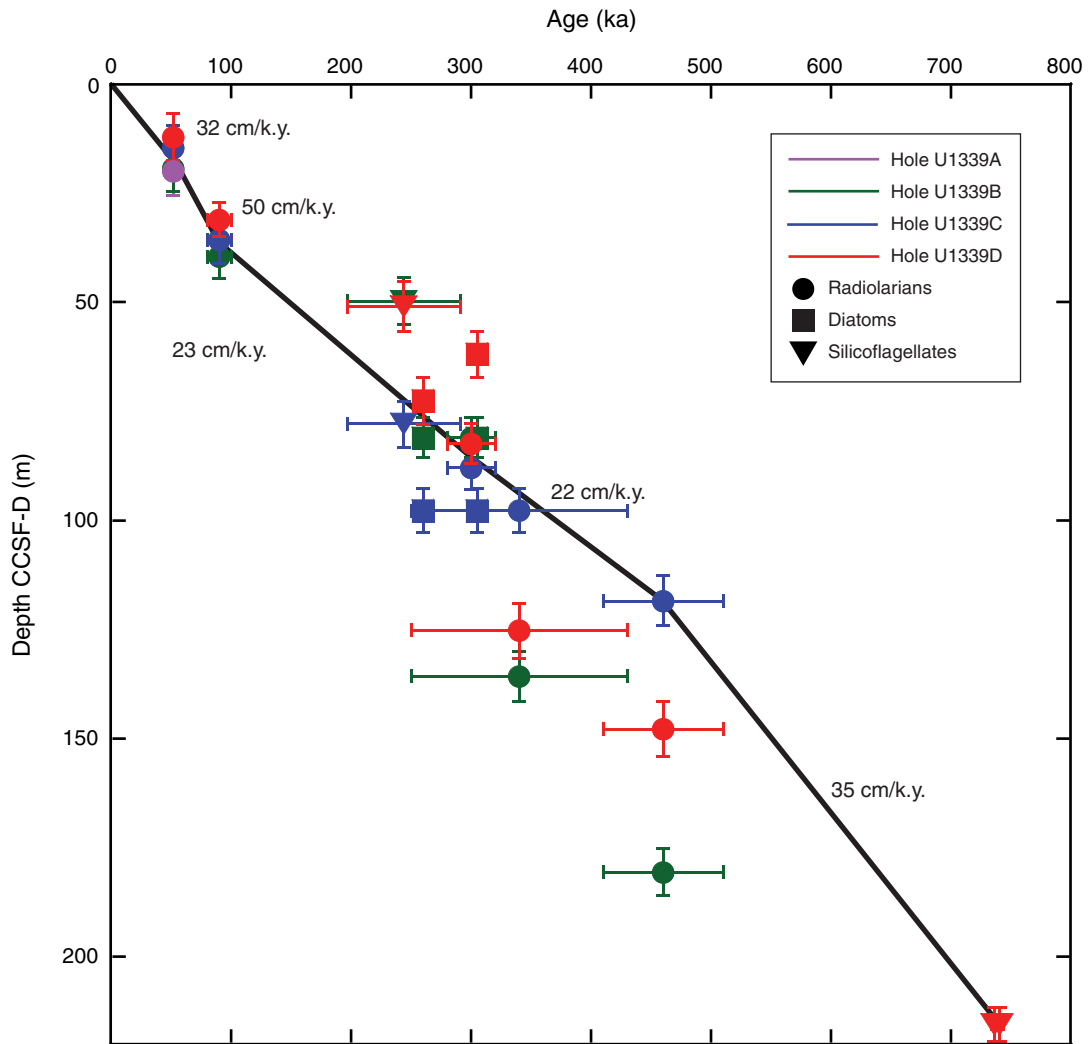


**Figure F15.** Inclination and declination of NRM after 20 mT AF demagnetization, Holes U1339A/B, U1339C, and U1339D. Declination data have been corrected using FlexIt orientation data.

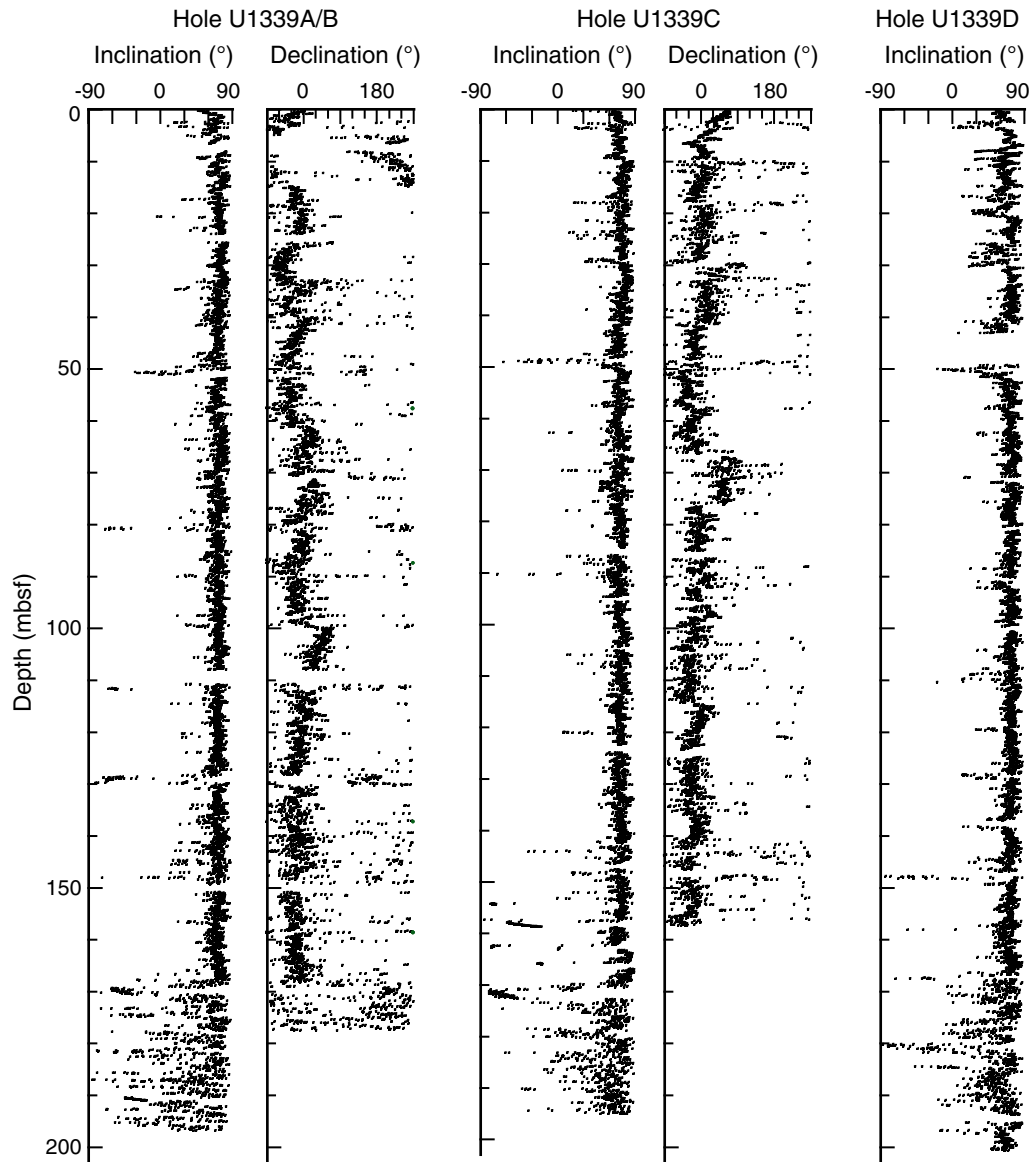


**Figure F16.** Low-inclination intervals associated with high NRM intensity after 20 mT AF demagnetization ( $Int_{20\text{ mT}}$ ).

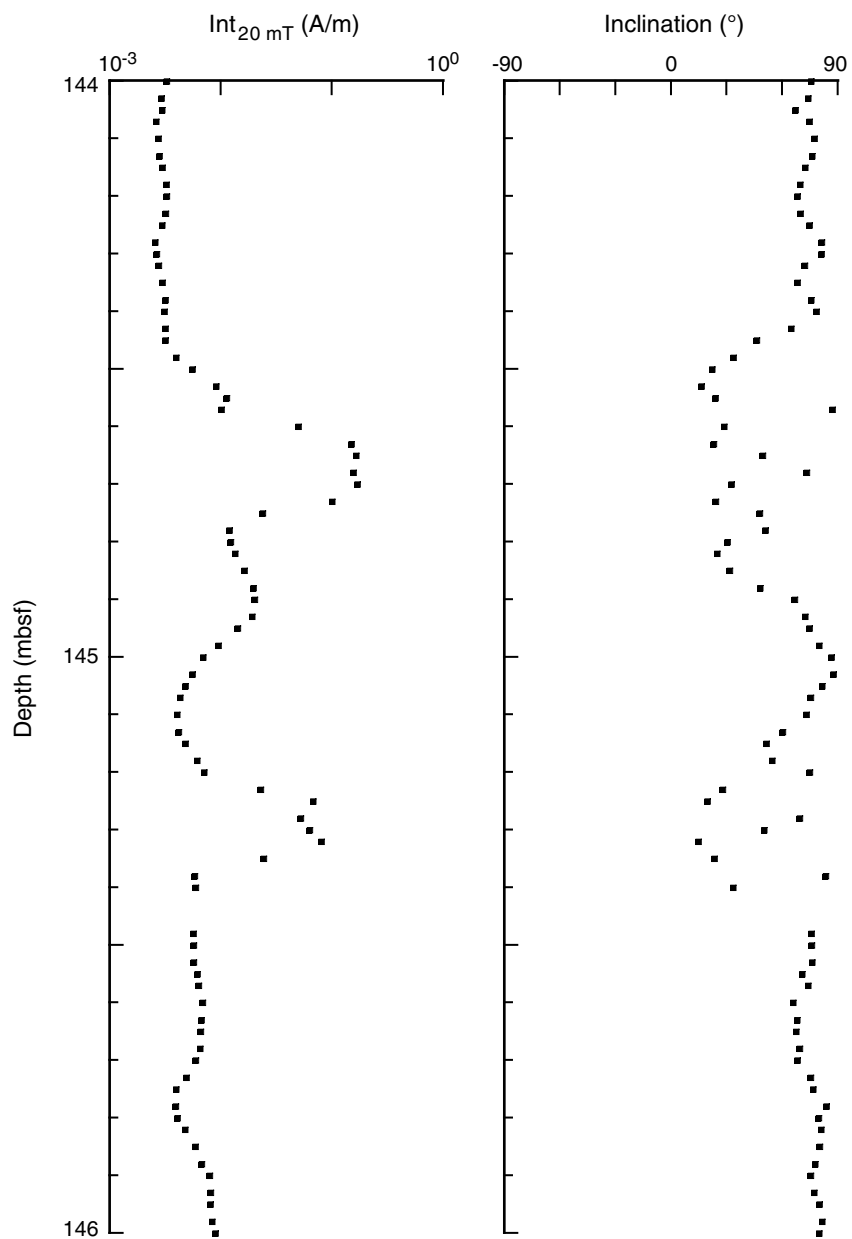


**Figure F17.** Magnetic susceptibility, NRM intensity after 20 mT AF demagnetization ( $Int_{20\text{ mT}}$ ), and the ratio of  $Int_{20\text{ mT}}$  to magnetic susceptibility, combined Holes U1339A/B.

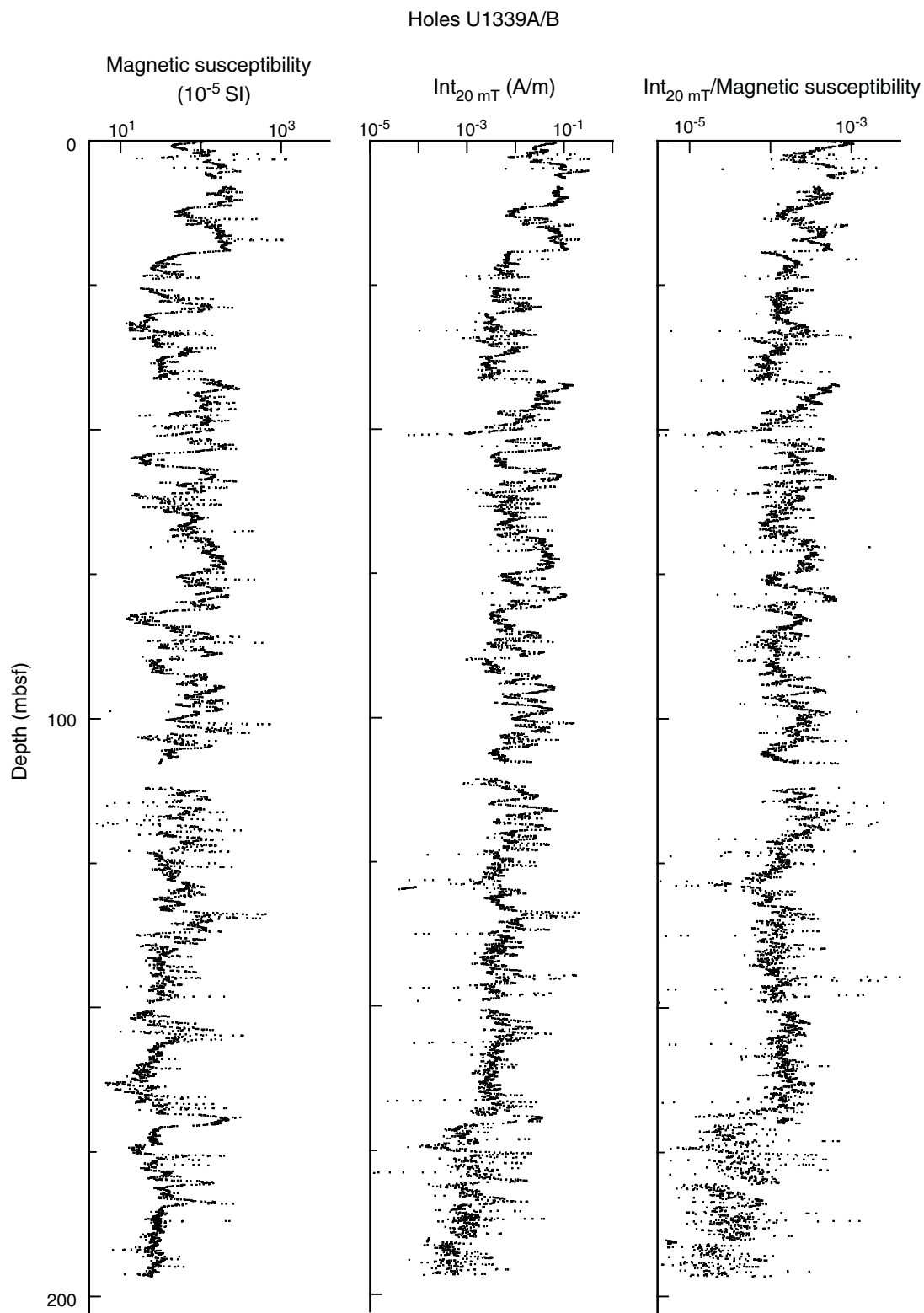


**Figure F18.** Dissolved chemical concentrations, Hole U1339B. **A.** Dissolved inorganic carbon (DIC). **B.** pH. **C.** Alkalinity. **D.** Chloride. **E.** Sulfate. **F.** Methane. **G.** Phosphate. **H.** Ammonium. **I.** Salinity.

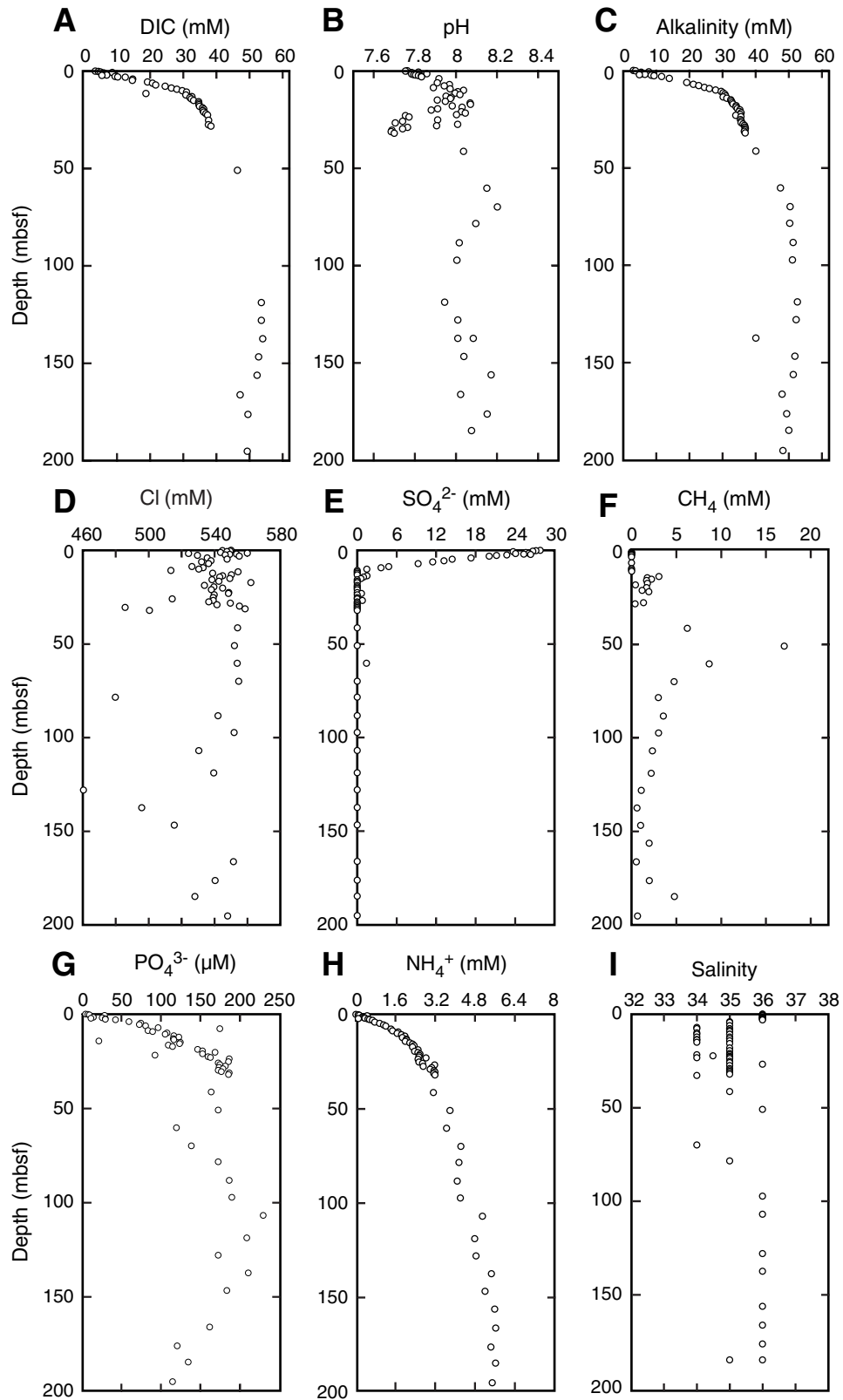
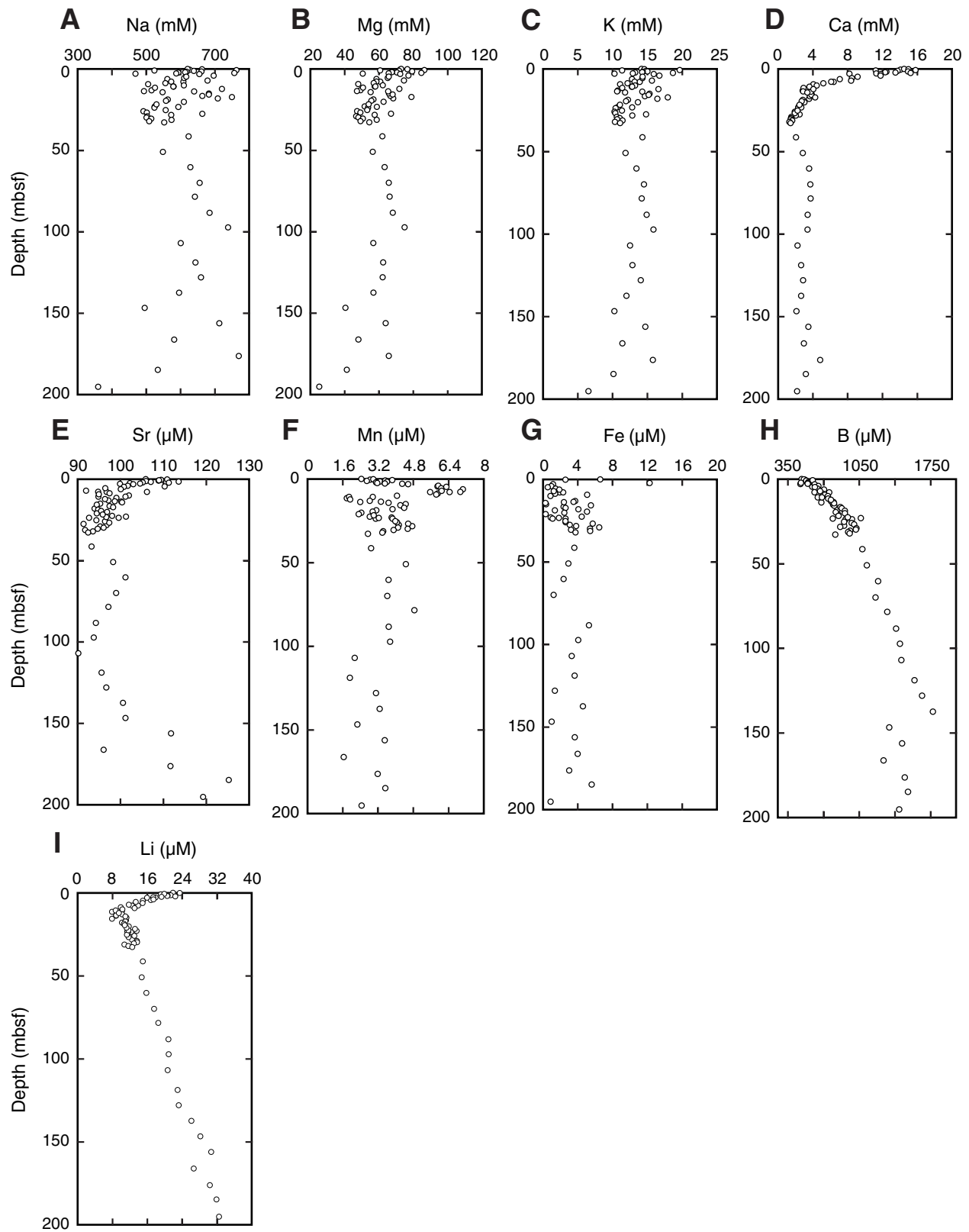


Figure F19. Dissolved chemical concentrations, Hole U1339B. A. Sodium. B. Magnesium. C. Potassium. D. Calcium. E. Strontium. F. Manganese. G. Iron. H. Boron. I. Lithium.



**Figure F20.** Solid-phase chemical concentrations, Holes U1339A and U1339B. **A.** Calcium carbonate ( $\text{CaCO}_3$ ). **B.** Total organic carbon (TOC). **C.** Total nitrogen (TN). **D.** Total sulfur (TS).

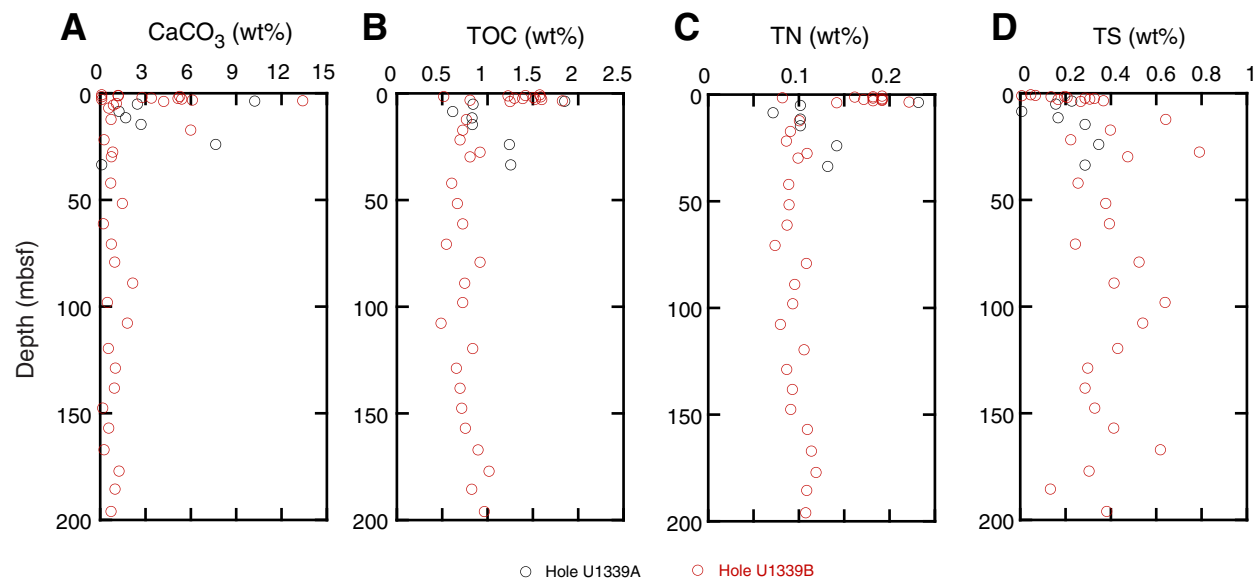
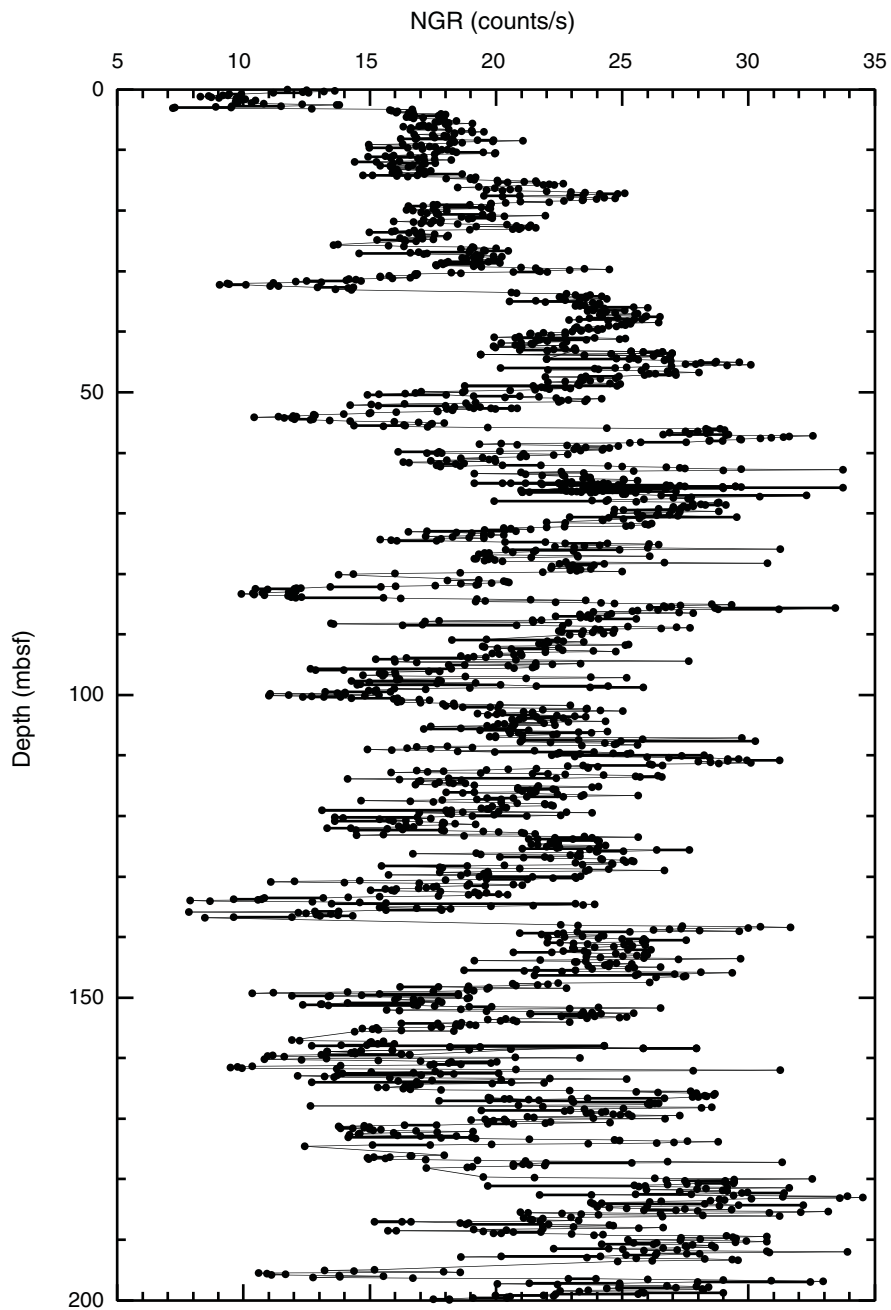


Figure F21. Downhole distribution of natural gamma ray (NGR) measurements, Hole U1339D.



**Figure F22.** Downhole distribution of moisture and density (MAD) wet bulk density determined on discrete samples of core sediment, combined Holes U1339A/B.

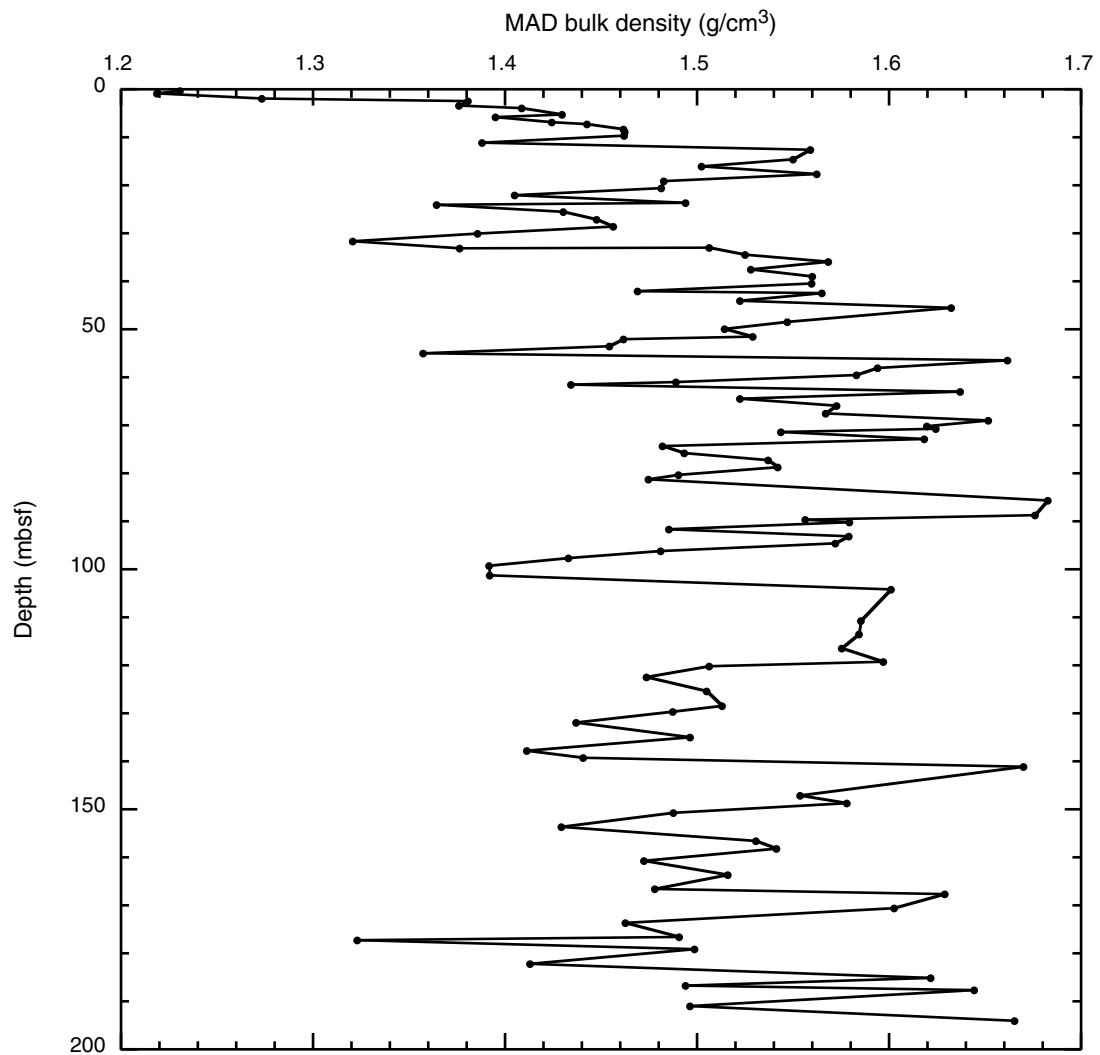
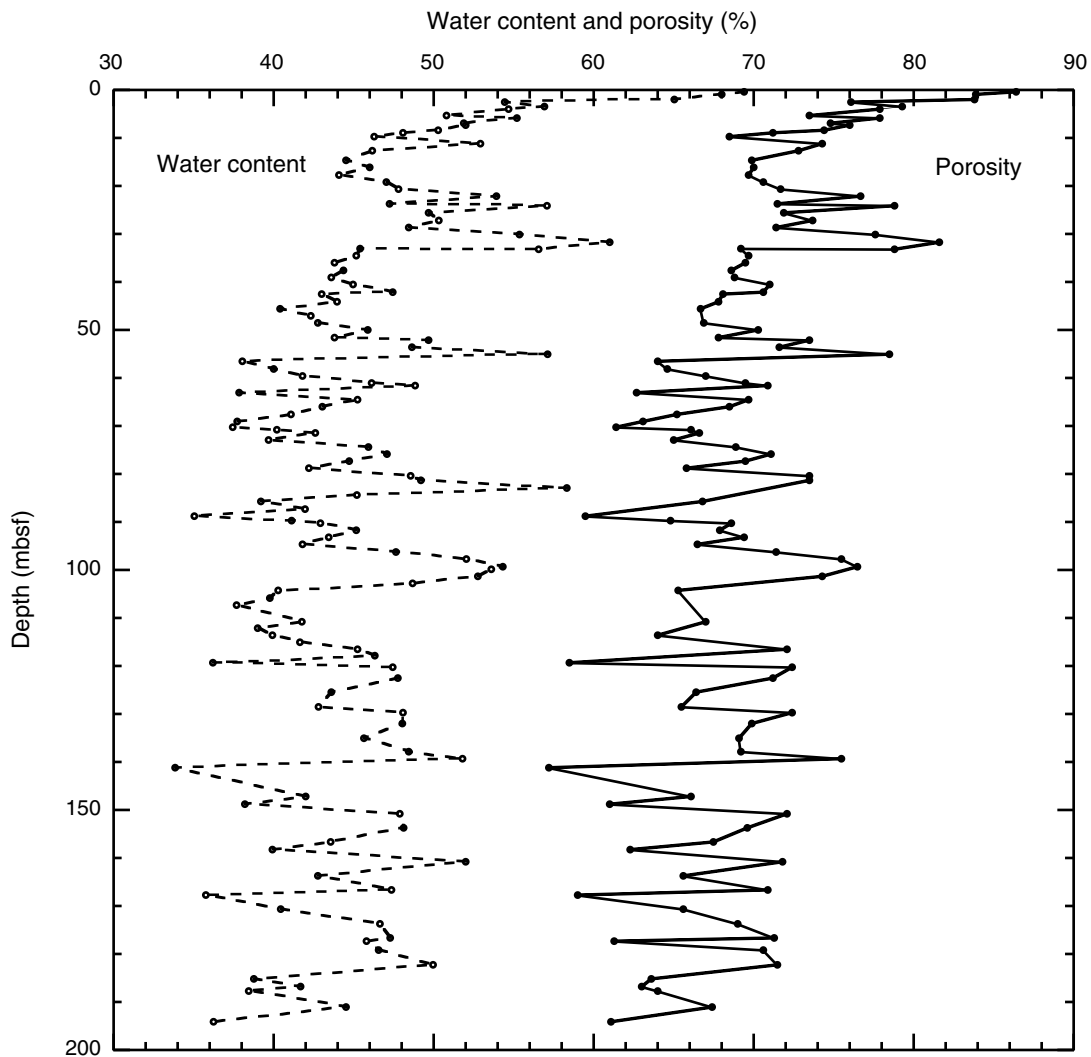


Figure F23. Downhole distribution of water content and porosity, combined Holes U1339A/B.



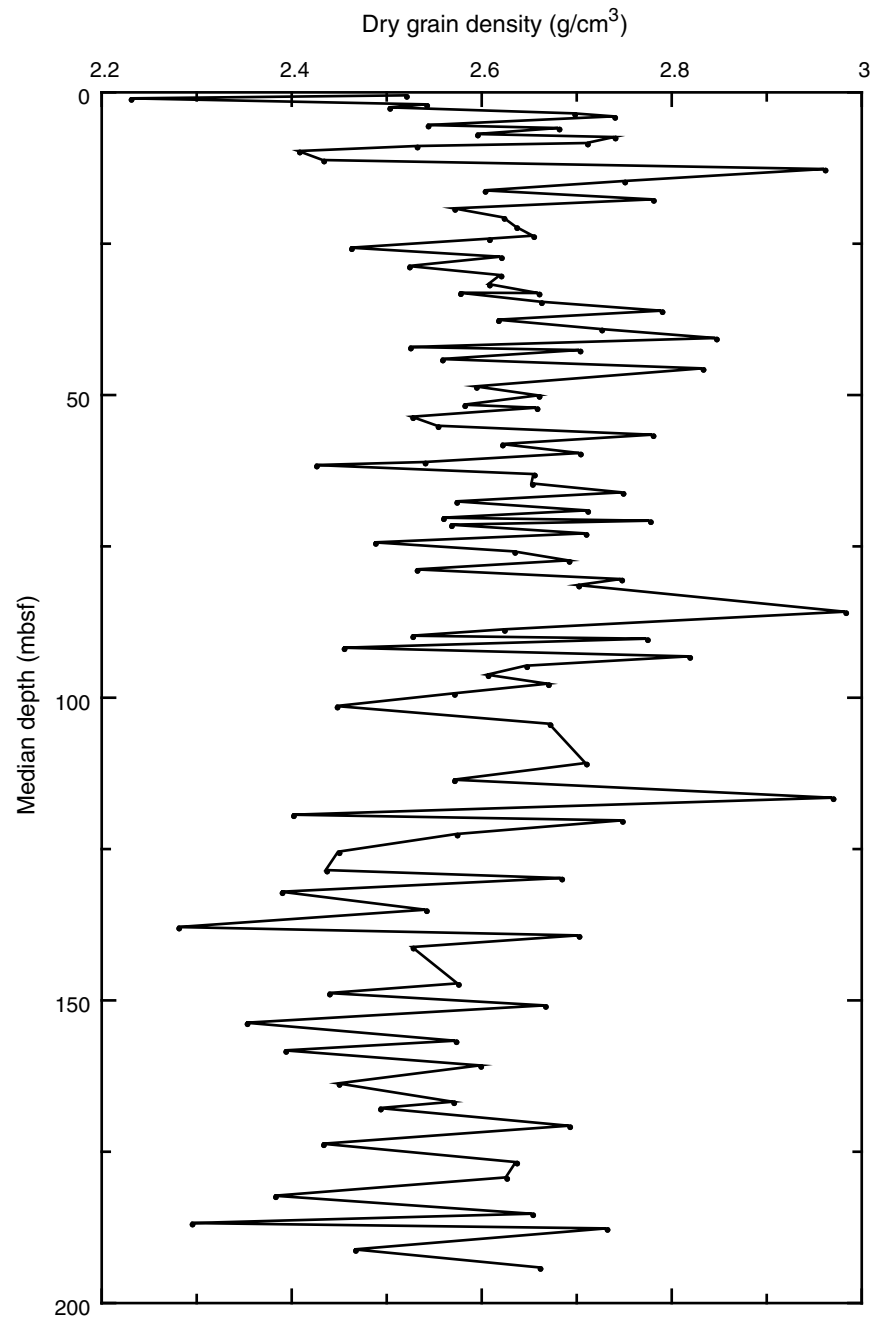
**Figure F24.** Downhole distribution of dry grain density, combined Holes U1339A/B.

Figure F25. Downhole distribution of thermal conductivity, Hole U1339D.

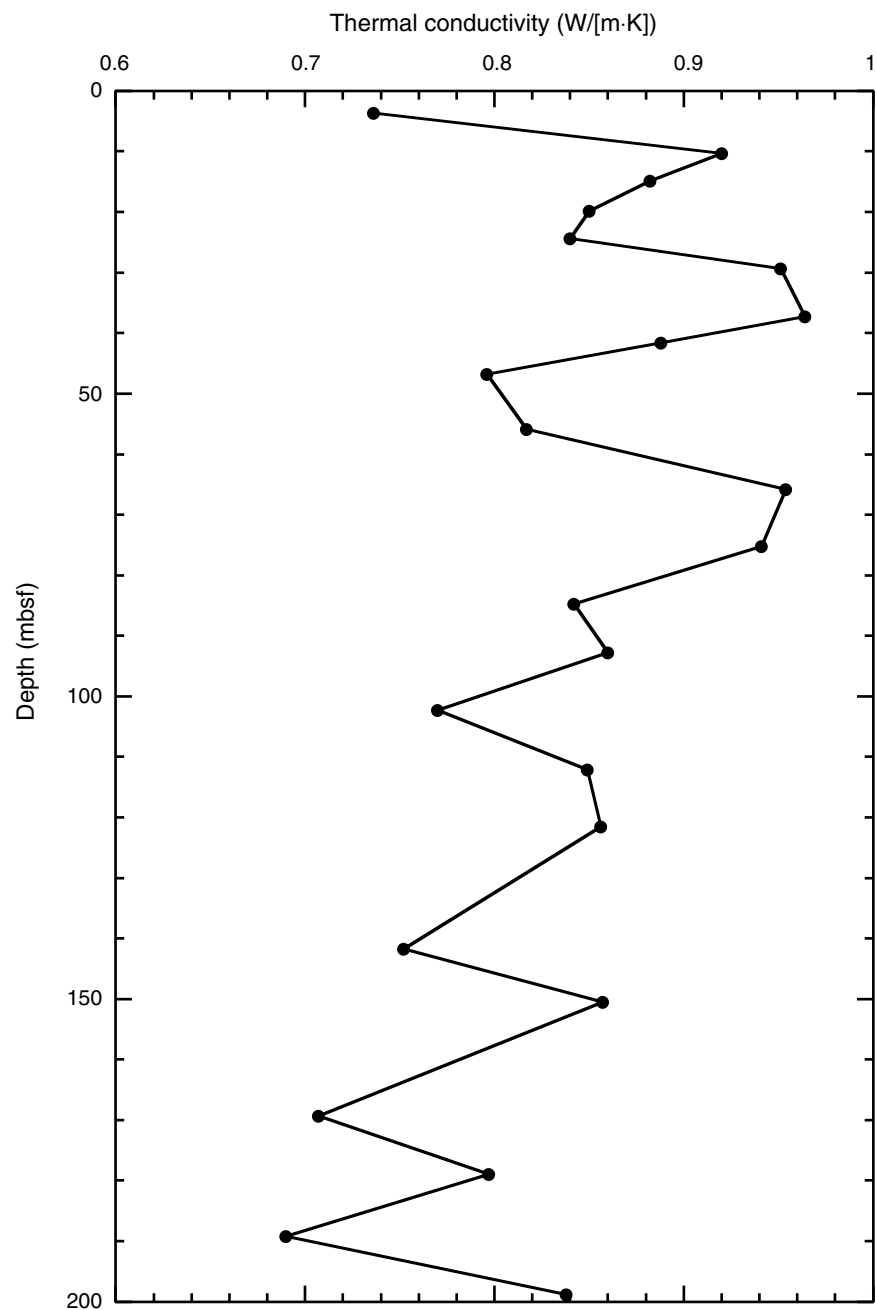


Figure F26. Gamma ray attenuation (GRA) bulk density vs. composite depth, Site U1339. A. 0–75 m CCSF-A. (Continued on next two pages.)

A

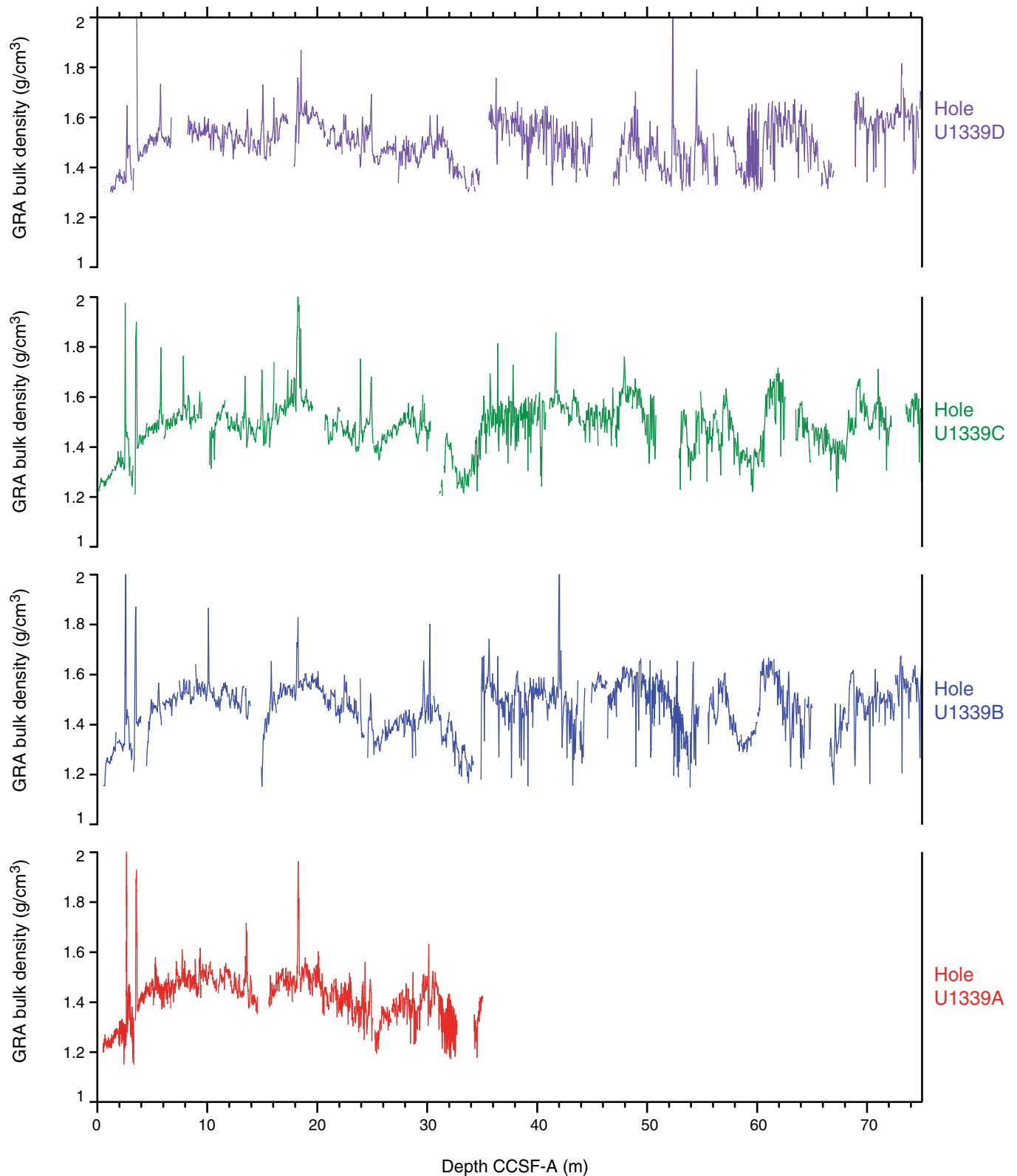


Figure F26 (continued). B. 75–150 m CCSF-A. (Continued on next page.)

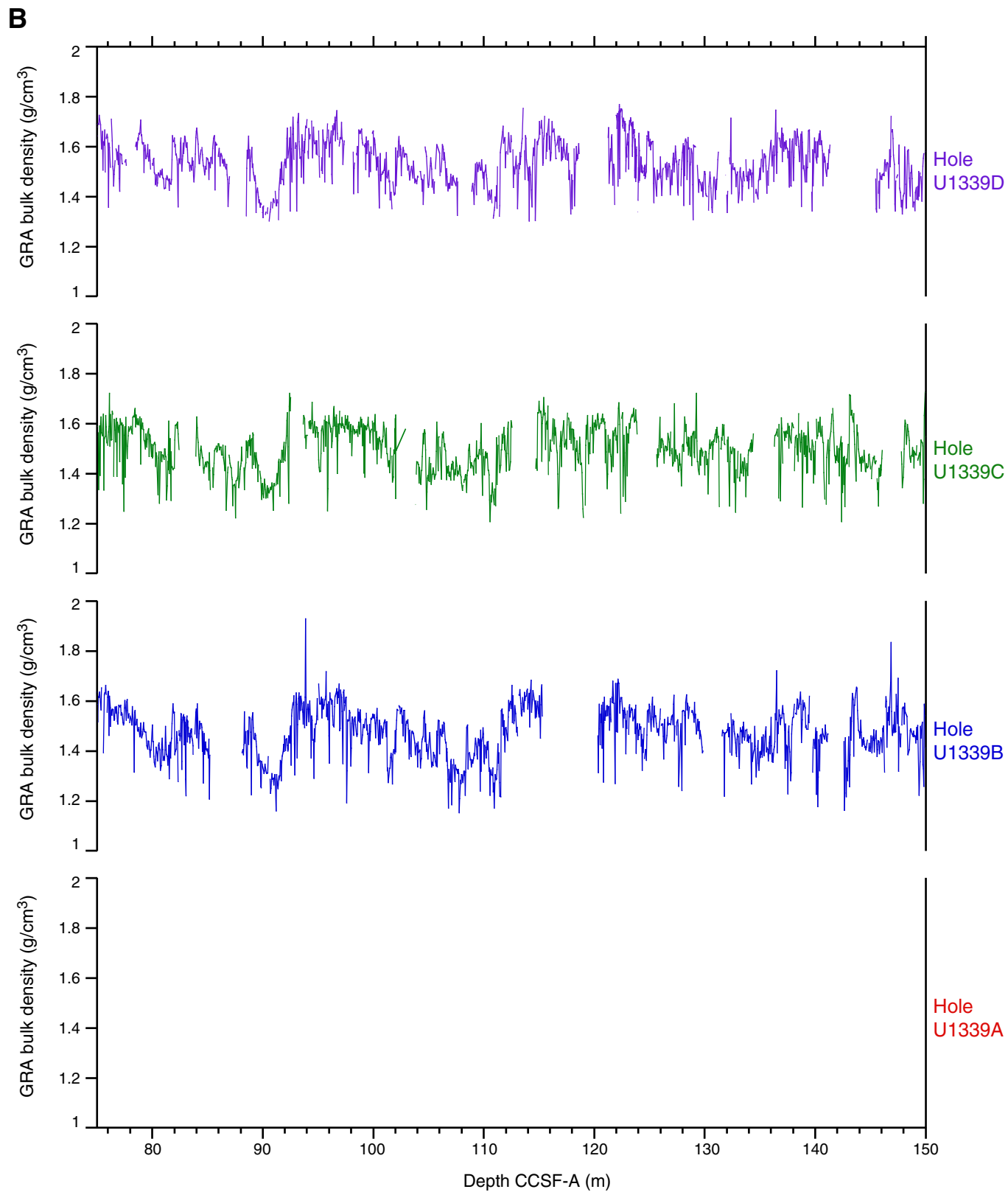
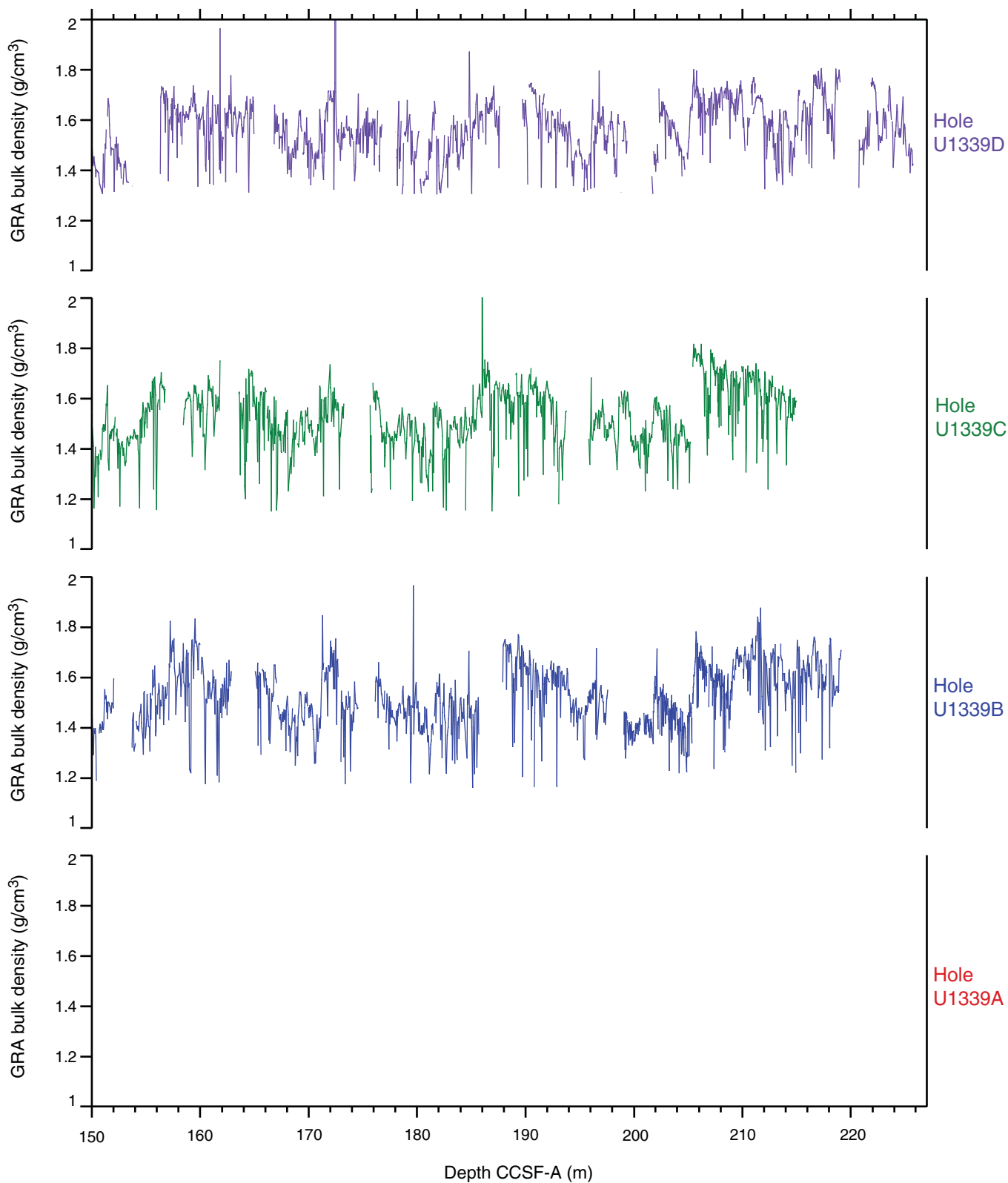


Figure F26 (continued). C. 150–225 m CCSF-A.

C



**Figure F27.** Natural gamma radiation (NGR) vs. composite depth, Site U1339. A. 0–75 m CCSF-A. No data are available for 0–32 m CCSF-A for Hole U1339B (microbiology-dedicated cores). (Continued on next two pages.)

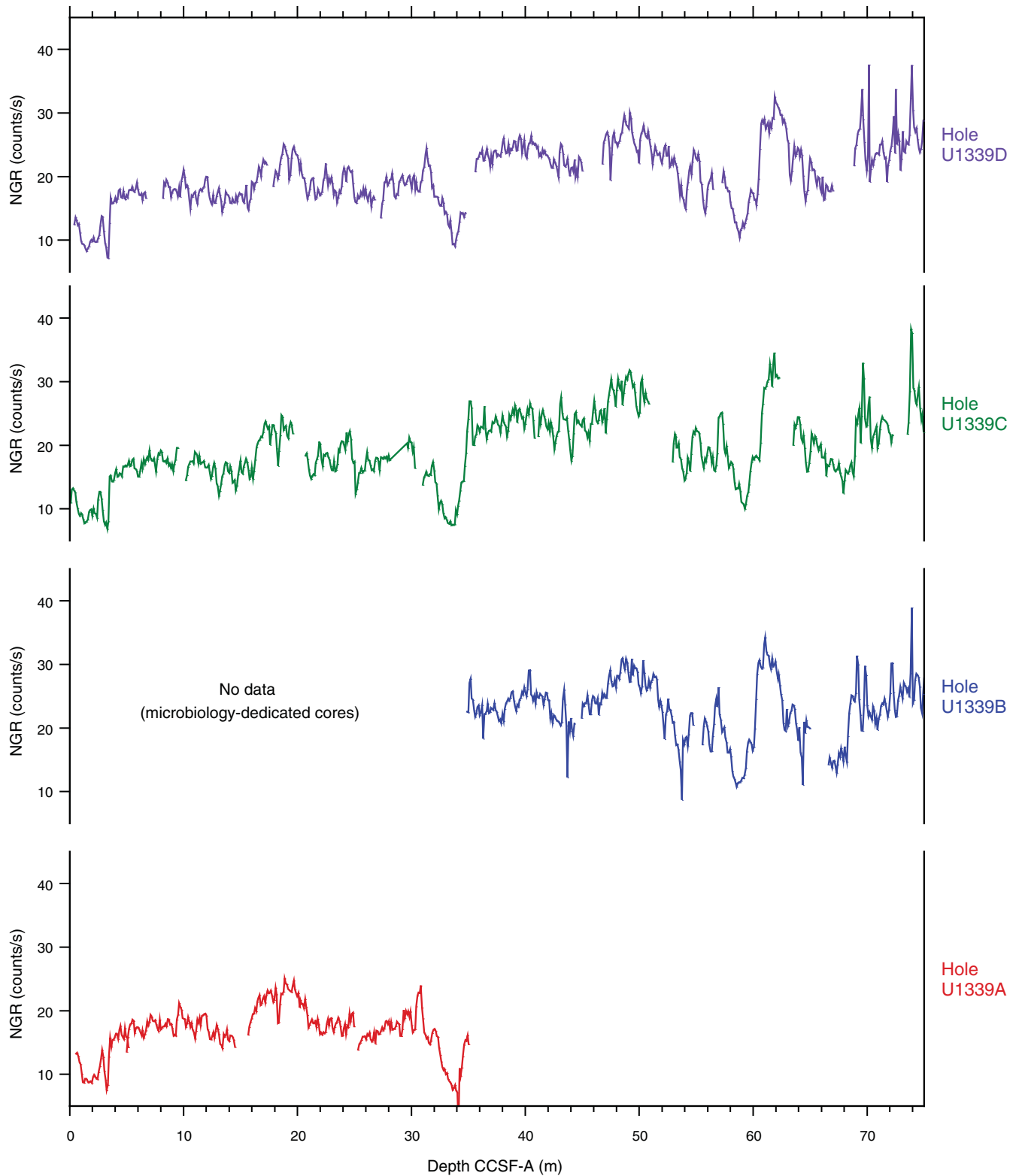
**A**

Figure F27 (continued). B. 75–150 m CCSF-A. (Continued on next page.)

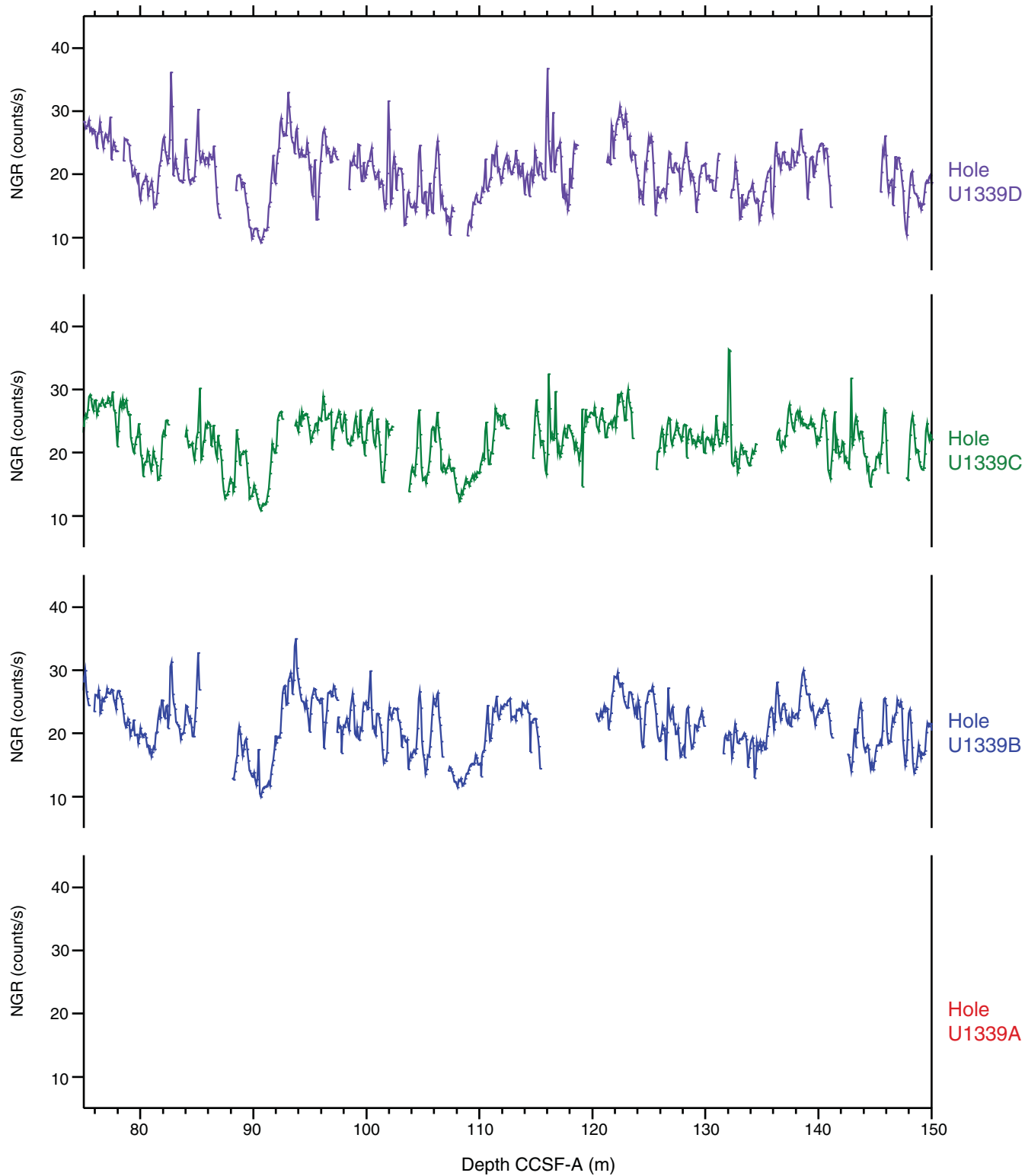
**B**

Figure F27 (continued). C. 150–225 m CCSF-A.

C

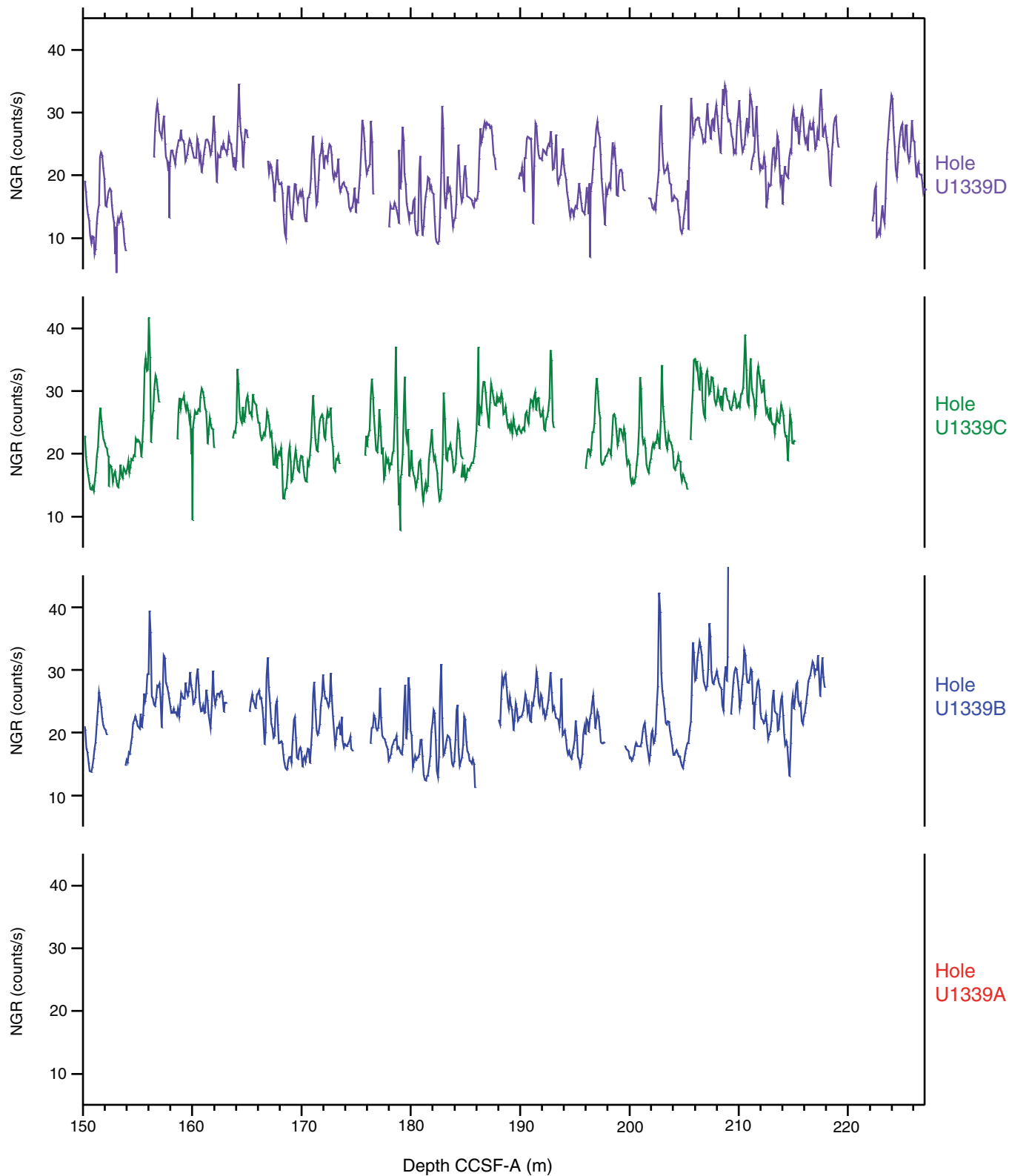


Figure F28. STMSL magnetic susceptibility vs. composite depth, Site U1339. A. 0–75 m CCSF-A. (Continued on next two pages.)

A

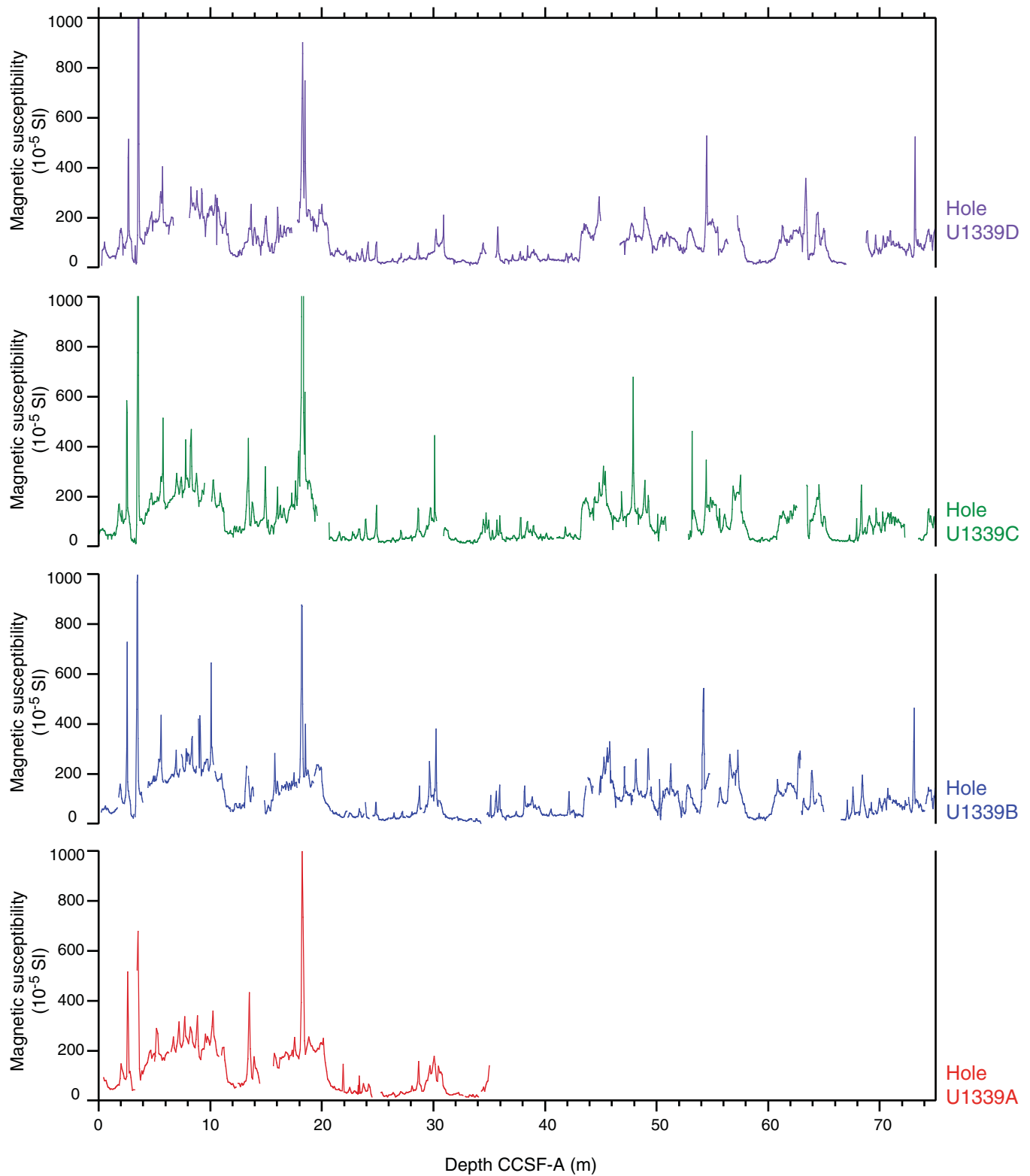


Figure F28 (continued). B. 75–150 m CCSF-A. (Continued on next page.)

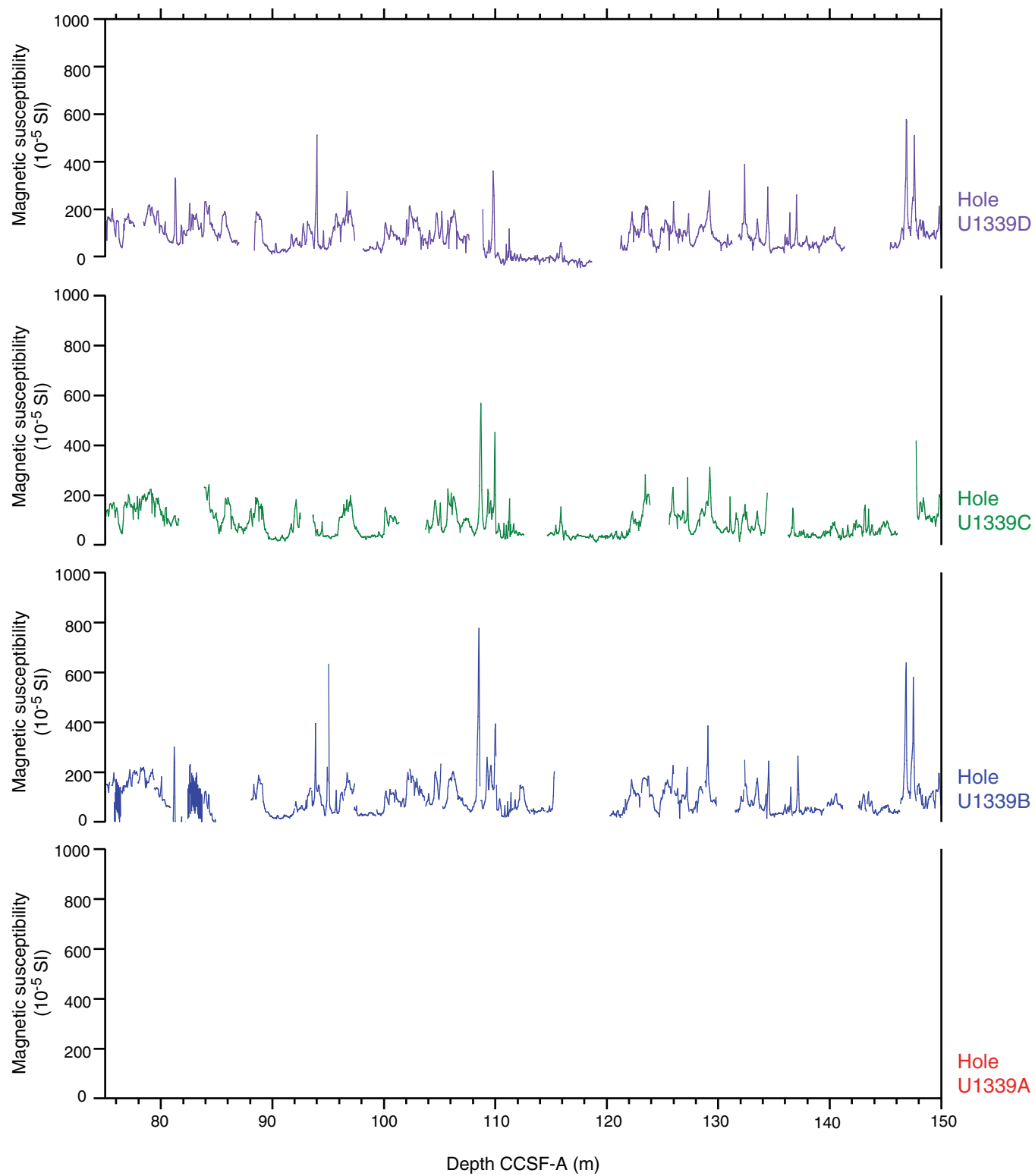
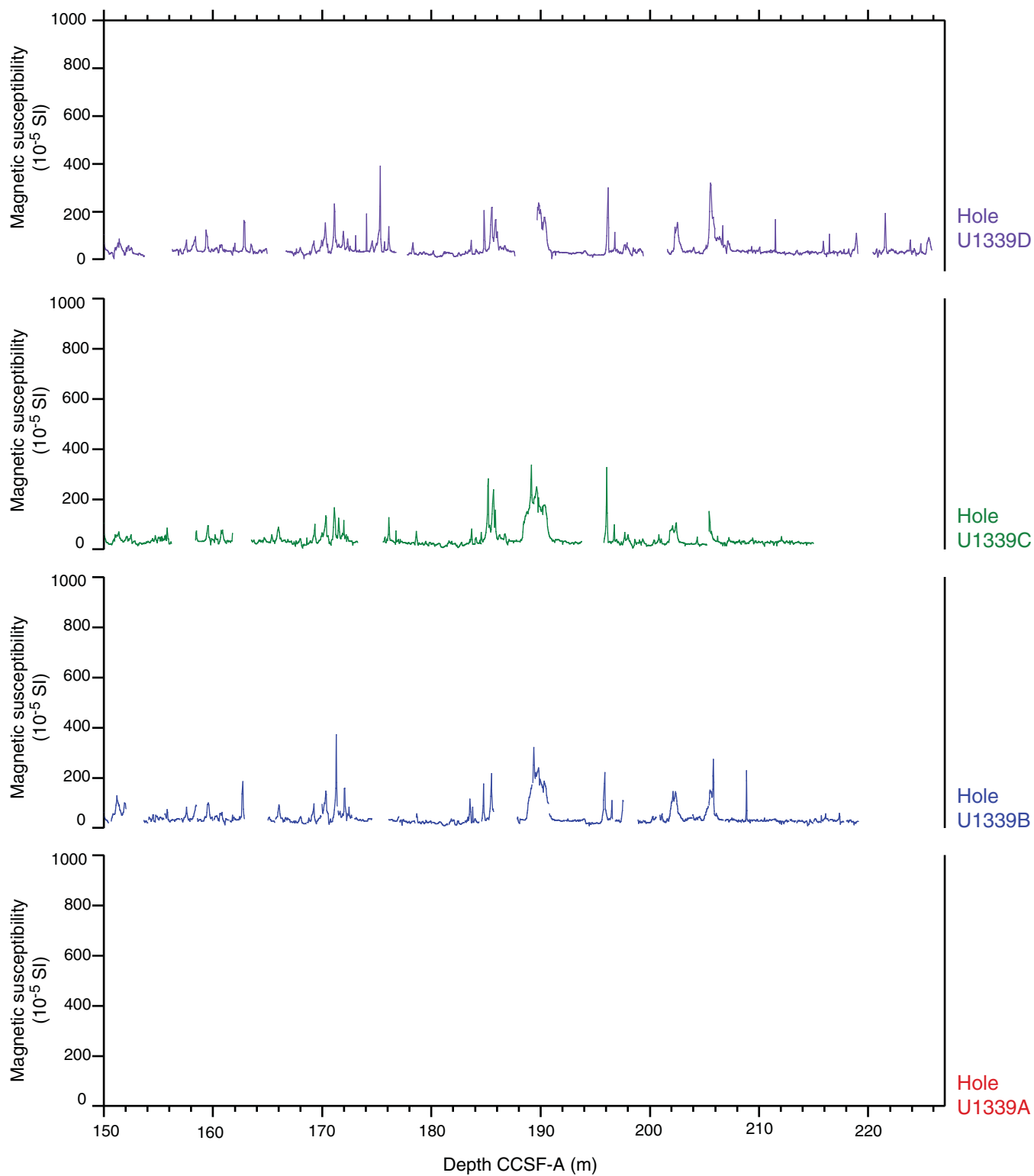
**B**

Figure F28 (continued). C. 150–225 m CCSF-A.

C





**Figure F29.** Spliced composite records of magnetic susceptibility, natural gamma radiation (NGR), and WRMSL gamma ray attenuation (GRA) bulk density with 40 cm smoothing, Site U1339.

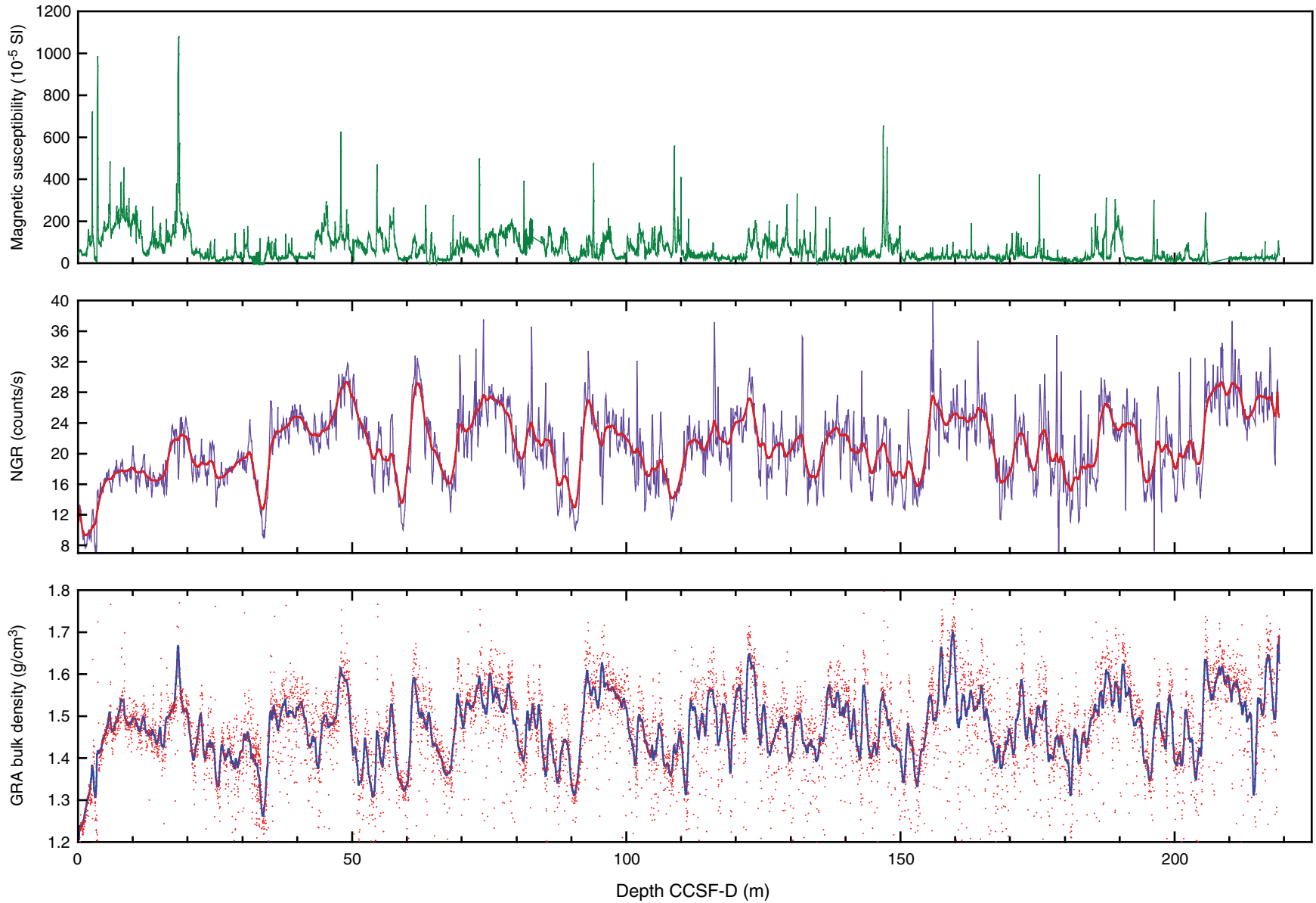


**Figure F30. A.** Mbsf vs. composite (CCSFF-A) depth in the splice, Site U1339. A 1:1 line is shown for comparison. **B.** Growth of cumulative depth offset (m) vs. mbsf in the splice. Cores from 0.00 to 100 mbsf have a growth factor of 1.10. Cores from below 100 mbsf have a growth factor of 1.17 m.

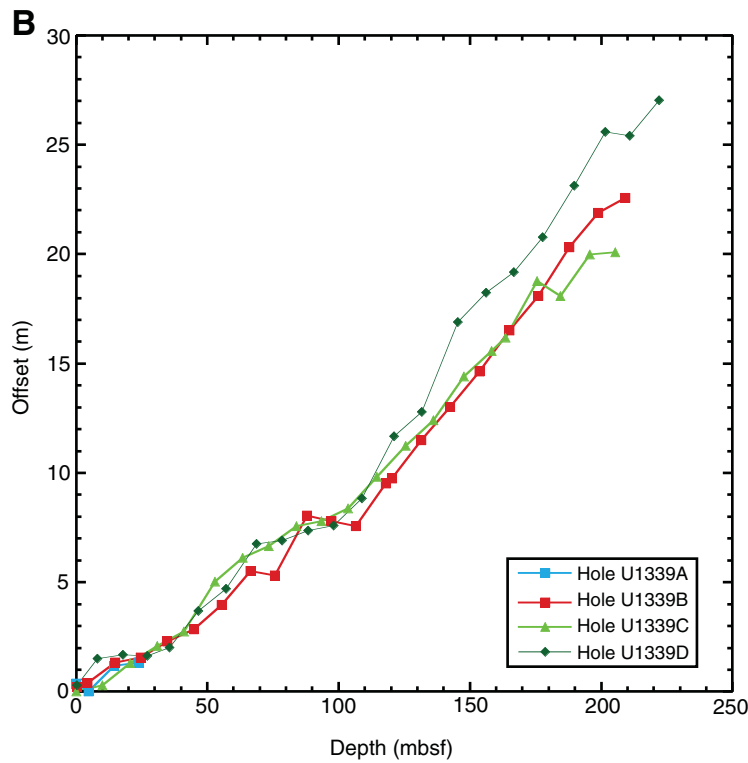
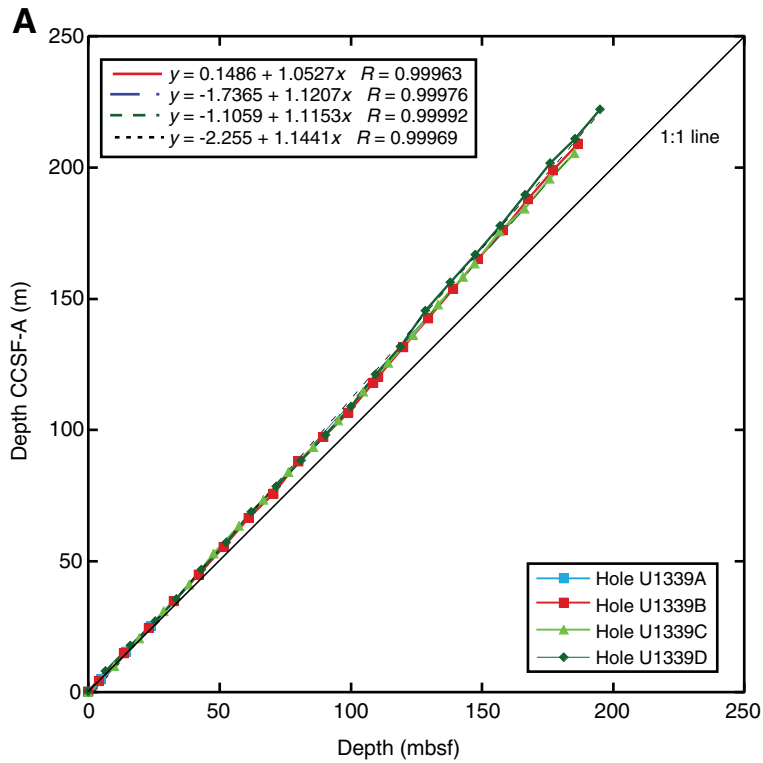


**Figure F31.** Summary of the logs recorded by the triple combination tool string, Hole U1339D. HLDS = Hostile Environment Litho-Density Sonde, gAPI = American Petroleum Institute gamma ray units, c/s = counts per second, MAD = moisture and density core data, GRA = gamma ray attenuation bulk density core track measurements, IDPH = deep induction phasor-processed resistivity, IMPH = medium induction phasor-processed resistivity, SFLU = spherically focused resistivity.

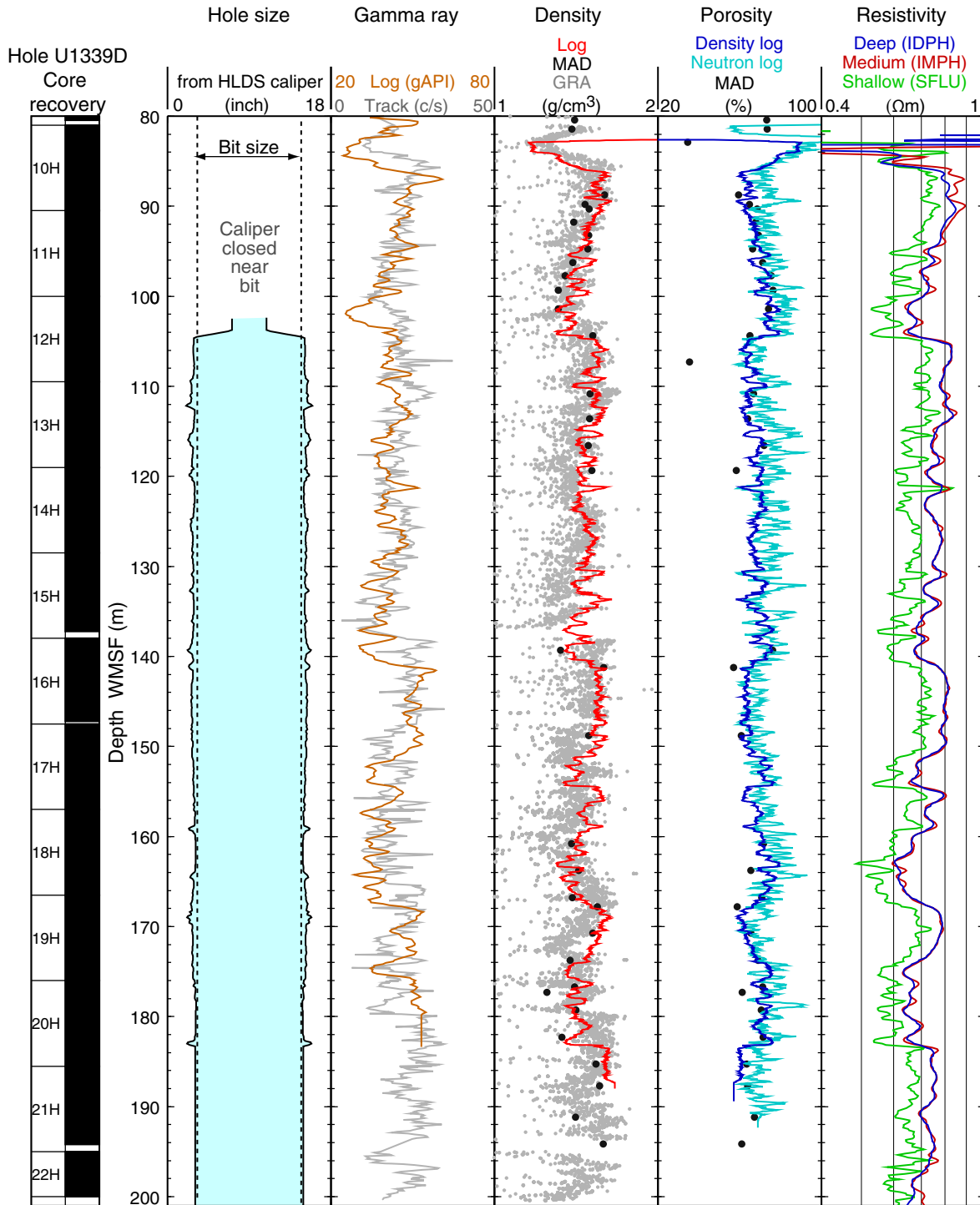


**Figure F32.** Summary of the logs recorded by the Formation MicroScanner (FMS)-sonic tool string, Hole U1339D. Hole size is calculated by the two calipers on the FMS. The gamma ray log recorded during the main pass of the triple combination (TC) tool string is shown for comparison and to confirm the good match between the two runs. High waveform coherence (red in the velocity track) is a measure of the reliability of the slowness/time coherence algorithm used to derive compressional velocity ( $V_p$ ) from the recorded waveforms. gAPI = American Petroleum Institute gamma ray units.

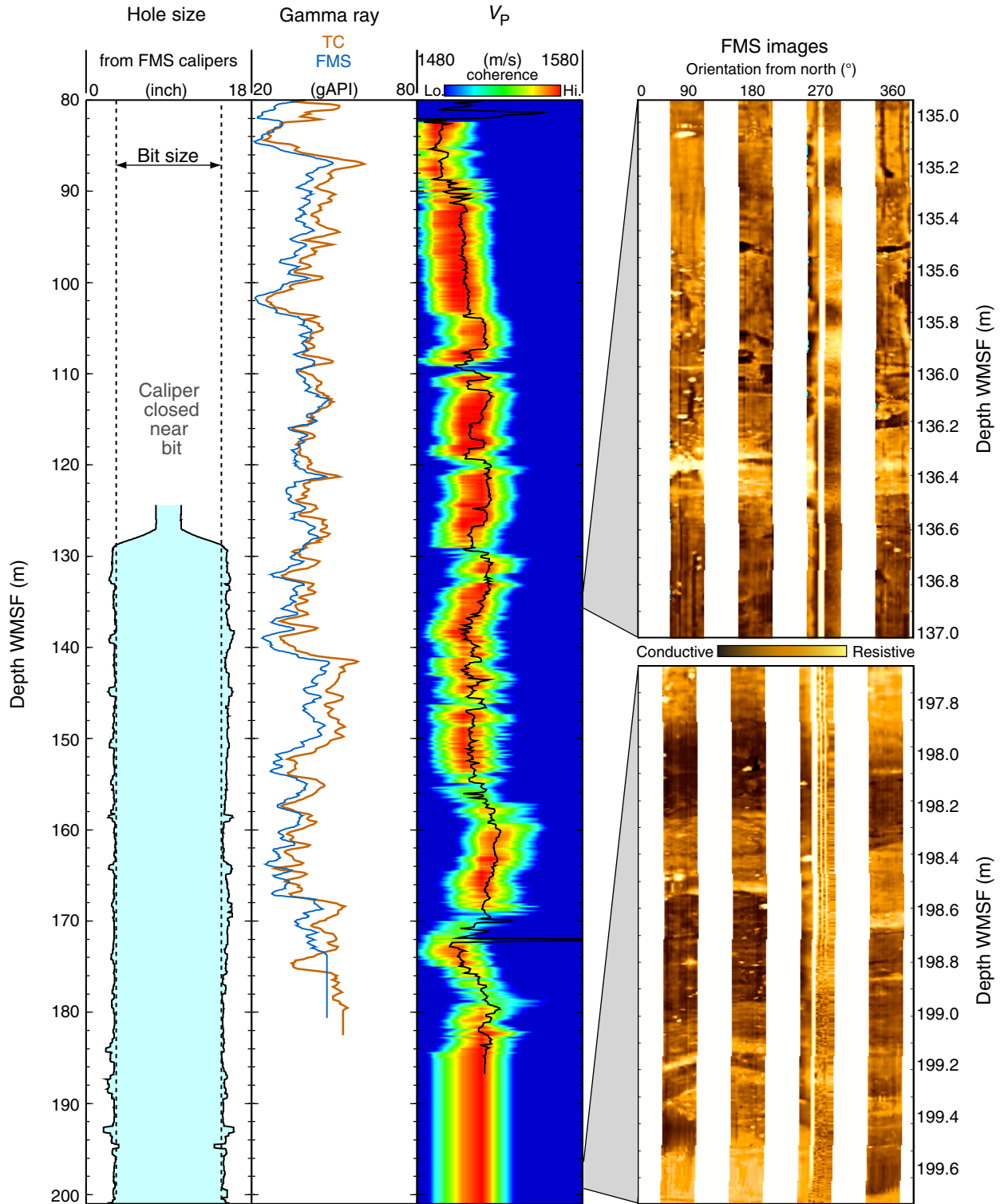


**Figure F33.** Summary of spectral natural gamma ray measurements, Hole U1339D. gAPI = American Petroleum Institute gamma ray units, CGR = computed gamma ray (gamma ray without the uranium contribution), GR = total gamma ray.

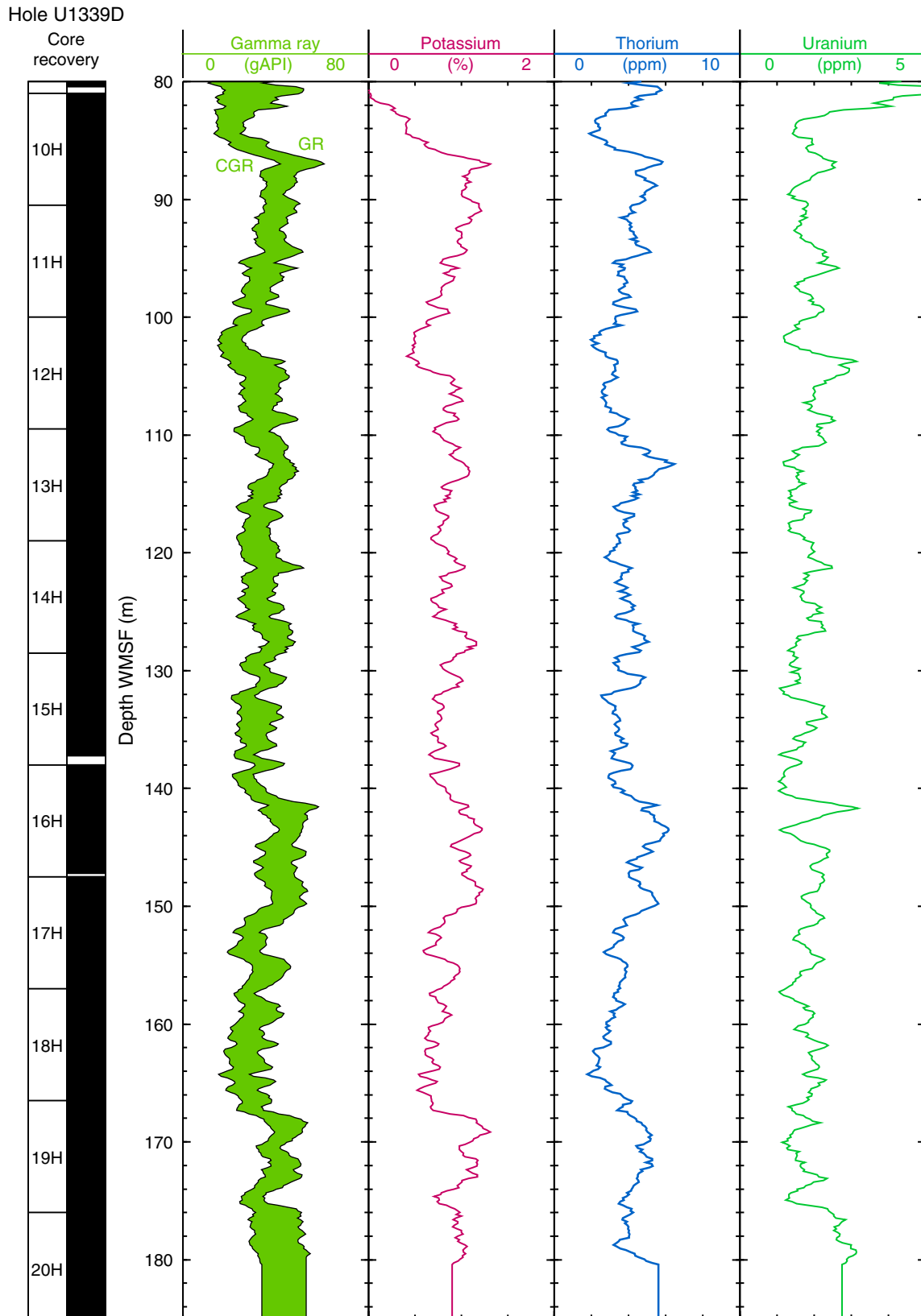


**Figure F34.** A. Records of APCT-3 penetrations and temperature decays, Hole U1339B. B. Summary of temperature measurements. The temperature gradient was derived from the three most successful records. Because of deviations in the decay curve, the temperature measured in Core 323-U1339B-13H was not considered sufficiently reliable.

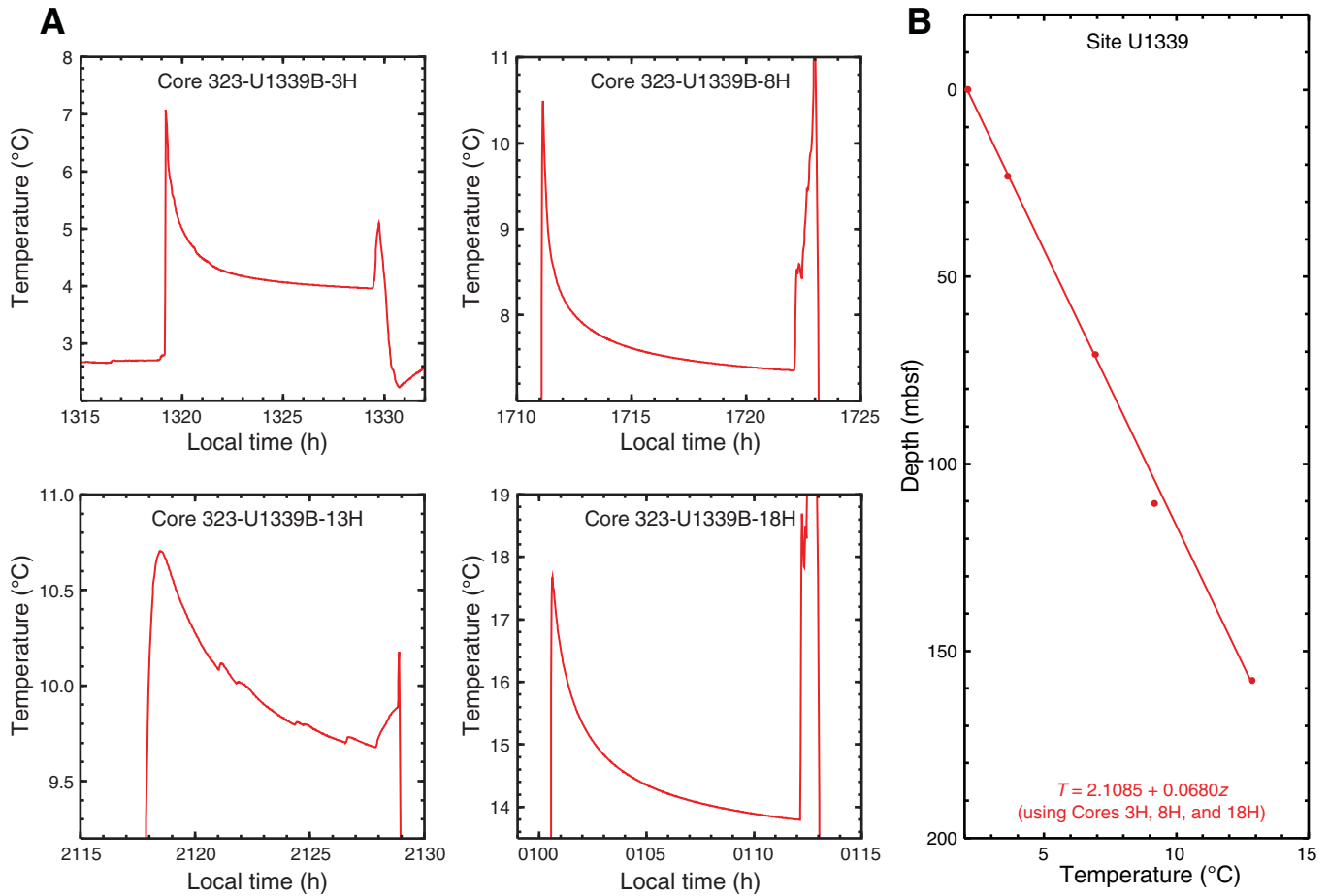


**Table T1.** Coring summary, Holes U1339A, U1339B, U1339C, and U1339D. (See table notes.) (Continued on next page.)

<b>Hole U1339A</b>									
Latitude: 54°40.2001'N									
Longitude: 169°58.9017'W									
Time on hole (h): 22.5									
Seafloor (drill pipe measurement from rig floor, m DRF): 1878									
Distance between rig floor and sea level (m): 11.3									
Water depth (drill pipe measurement from sea level, m): 1865.8									
Total depth (drill pipe measurement from rig floor, m DRF): 1911.4									
Total penetration (mbsf): 33.4									
Total length of cored section (m): 33.4									
Total core recovered (m): 34.87									
Core recovery (%): 104									
Total number of cores: 4									
<b>Hole U1339B</b>									
Latitude: 54°40.2103'N									
Longitude: 169°58.9106'W									
Time on hole (h): 29.67									
Seafloor (drill pipe measurement from rig floor, m DRF): 1878.9									
Distance between rig floor and sea level (m): 11.3									
Water depth (drill pipe measurement from sea level, m): 1867.6									
Total depth (drill pipe measurement from rig floor, m DRF): 2074.9									
Total penetration (mbsf): 196.0									
Total length of cored section (m): 196.0									
Total core recovered (m): 204.45									
Core recovery (%): 104									
Total number of cores: 22									
<b>Hole U1339C</b>									
Latitude: 54°40.2063'N									
Longitude: 169°58.8852'W									
Time on hole (h): 19.83									
Seafloor (drill pipe measurement from rig floor, m DRF): 1878.9									
Distance between rig floor and sea level (m): 11.3									
Water depth (drill pipe measurement from sea level, m): 1867.6									
Total depth (drill pipe measurement from rig floor, m DRF): 2073.7									
Total penetration (mbsf): 194.8									
Total length of cored section (m): 194.8									
Total core recovered (m): 199.40									
Core recovery (%): 102									
Total number of cores: 21									
<b>Hole U1339D</b>									
Latitude: 54°40.1891'N									
Longitude: 169°58.8909'W									
Time on hole (h): 39.58									
Seafloor (drill pipe measurement from rig floor, m DRF): 1879.4									
Distance between rig floor and sea level (m): 11.3									
Water depth (drill pipe measurement from sea level, m): 1868.1									
Total depth (drill pipe measurement from rig floor, m DRF): 2079.4									
Total penetration (mbsf): 200.0									
Total length of cored section (m): 200.0									
Total core recovered (m): 206.0									
Core recovery (%): 103									
Total number of cores: 22									

Core	Date (2009)	UTC (h)	Depth DSF (m)		Length (m)		Recovery (%)	Comments
			Top	Bottom	Cored	Recovered		
<b>323-U1339A-</b>								
1H	17 Jul	1550	0.0	4.9	4.9	4.94	101	Nonmagnetic barrel
2H	17 Jul	1700	4.9	14.4	9.5	9.84	104	Oriented nonmagnetic barrel
3H	17 Jul	1820	14.4	23.9	9.5	9.93	105	Oriented nonmagnetic barrel
4H	17 Jul	1910	23.9	33.4	9.5	10.16	107	Oriented nonmagnetic barrel
Cored totals:					33.4	34.87	104	
<b>323-U1339B-</b>								
1H	18 Jul	1055	0.0	4.0	4.0	4.01	100	Oriented nonmagnetic barrel
2H	18 Jul	1135	4.0	13.5	9.5	9.75	103	Oriented nonmagnetic barrel
3H	18 Jul	1240	13.5	23.0	9.5	9.49	100	Oriented nonmagnetic barrel
4H	18 Jul	1325	23.0	32.5	9.5	9.73	102	Oriented nonmagnetic barrel
5H	18 Jul	1400	32.5	42.0	9.5	9.77	103	Oriented nonmagnetic barrel
6H	18 Jul	1455	42.0	51.5	9.5	10.33	109	Oriented nonmagnetic barrel

Table T1 (continued).

Core	Date (2009)	UTC (h)	Depth DSF (m)		Length (m)		Recovery (%)	Comments
			Top	Bottom	Cored	Recovered		
7H	18 Jul	1530	51.5	61.0	9.5	10.10	106	Oriented nonmagnetic barrel
8H	18 Jul	1635	61.0	70.5	9.5	9.95	105	Oriented nonmagnetic barrel
9H	18 Jul	1725	70.5	80.0	9.5	9.97	105	Oriented nonmagnetic barrel
10H	18 Jul	1805	80.0	89.5	9.5	9.98	105	Oriented nonmagnetic barrel
11H	18 Jul	1850	89.5	99.0	9.5	9.85	104	Oriented nonmagnetic barrel
12H	18 Jul	1935	99.0	108.5	9.5	9.48	100	Oriented nonmagnetic barrel
13H	18 Jul	2040	108.5	110.5	2.0	0.49	24	Oriented nonmagnetic barrel
14H	18 Jul	2130	110.5	120.0	9.5	10.07	106	Oriented nonmagnetic barrel
15H	18 Jul	2210	120.0	129.5	9.5	10.08	106	Oriented nonmagnetic barrel
16H	18 Jul	2305	129.5	139.0	9.5	10.01	105	Oriented nonmagnetic barrel
17H	19 Jul	0005	139.0	148.5	9.5	9.67	102	Oriented nonmagnetic barrel, liner patch
18H	19 Jul	0130	148.5	158.0	9.5	10.39	109	Oriented nonmagnetic barrel
19H	19 Jul	0250	158.0	167.5	9.5	9.96	105	Oriented nonmagnetic barrel
20H	19 Jul	0350	167.5	177.0	9.5	10.24	108	Steel barrel
21H	19 Jul	0440	177.0	186.5	9.5	10.70	113	Steel barrel
22H	19 Jul	0530	186.5	196.0	9.5	10.43	110	Steel barrel, shattered liner
			Cored totals:		196.0	204.45	104	
323-U1339C-								
1H	19 Jul	0945	0.0	9.8	9.8	9.78	100	Oriented nonmagnetic barrel
2H	19 Jul	1045	9.8	19.3	9.5	9.72	102	Oriented nonmagnetic barrel
3H	19 Jul	1130	19.3	28.8	9.5	9.89	104	Oriented nonmagnetic barrel
4H	19 Jul	1215	28.8	38.3	9.5	10.16	107	Oriented nonmagnetic barrel
5H	19 Jul	1255	38.3	47.8	9.5	10.19	107	Oriented nonmagnetic barrel
6H	19 Jul	1330	47.8	57.3	9.5	10.14	107	Oriented nonmagnetic barrel
7H	19 Jul	1420	57.3	66.8	9.5	9.35	98	Oriented nonmagnetic barrel
8H	19 Jul	1510	66.8	76.3	9.5	9.79	103	Oriented nonmagnetic barrel
9H	19 Jul	1620	76.3	85.8	9.5	9.04	95	Oriented nonmagnetic barrel
10H	19 Jul	1700	85.8	95.3	9.5	9.31	98	Oriented nonmagnetic barrel
11H	19 Jul	1745	95.3	104.8	9.5	9.23	97	Oriented nonmagnetic barrel
12H	19 Jul	1825	104.8	114.3	9.5	9.66	102	Oriented nonmagnetic barrel
13H	19 Jul	1910	114.3	123.8	9.5	9.51	100	Oriented nonmagnetic barrel
14H	19 Jul	1950	123.8	133.3	9.5	10.29	108	Oriented nonmagnetic barrel
15H	19 Jul	2040	133.3	142.8	9.5	9.72	102	Oriented nonmagnetic barrel
16H	19 Jul	2120	142.8	147.3	4.5	3.82	85	Oriented nonmagnetic barrel
17H	19 Jul	2215	147.3	156.8	9.5	10.31	109	Oriented nonmagnetic barrel
18H	19 Jul	2300	156.8	166.3	9.5	9.22	97	Steel barrel
19H	19 Jul	2355	166.3	175.8	9.5	10.18	107	Steel barrel
20H	20 Jul	0040	175.8	185.3	9.5	10.05	106	Steel barrel
21H	20 Jul	0130	185.3	194.8	9.5	10.04	106	Steel barrel
			Cored totals:		194.8	199.40	102	
323-U1339D-								
1H	20 Jul	0445	0.0	6.6	6.6	6.62	100	Nonmagnetic barrel
2H	20 Jul	0545	6.6	16.1	9.5	9.54	100	Nonmagnetic barrel
3H	20 Jul	0635	16.1	25.6	9.5	9.59	101	Nonmagnetic barrel
4H	20 Jul	0720	25.6	33.5	7.9	7.88	100	Nonmagnetic barrel
5H	20 Jul	0845	33.5	43.0	9.5	9.84	104	Nonmagnetic barrel
6H	20 Jul	0930	43.0	52.5	9.5	10.07	106	Nonmagnetic barrel
7H	20 Jul	1010	52.5	62.0	9.5	10.08	106	Nonmagnetic barrel
8H	20 Jul	1045	62.0	71.5	9.5	9.30	98	Nonmagnetic barrel
9H	20 Jul	1120	71.5	81.0	9.5	8.95	94	Nonmagnetic barrel
10H	20 Jul	1155	81.0	90.5	9.5	9.63	101	Nonmagnetic barrel
11H	20 Jul	1230	90.5	100.0	9.5	9.98	105	Nonmagnetic barrel
12H	20 Jul	1305	100.0	109.5	9.5	10.42	110	Nonmagnetic barrel
13H	20 Jul	1340	109.5	119.0	9.5	10.49	110	Nonmagnetic barrel
14H	20 Jul	1510	119.0	128.5	9.5	9.93	105	Nonmagnetic barrel
15H	20 Jul	1540	128.5	138.0	9.5	8.74	92	Nonmagnetic barrel
16H	20 Jul	1615	138.0	147.5	9.5	9.21	97	Nonmagnetic barrel
17H	20 Jul	1645	147.5	157.0	9.5	10.48	110	Nonmagnetic barrel
18H	20 Jul	1740	157.0	166.5	9.5	10.28	108	Steel barrel
19H	20 Jul	1820	166.5	176.0	9.5	10.37	109	Steel barrel
20H	20 Jul	1855	176.0	185.5	9.5	10.09	106	Steel barrel
21H	20 Jul	1930	185.5	195.0	9.5	8.71	92	Steel barrel
22H	20 Jul	2010	195.0	200.0	5.0	5.83	117	Steel barrel
			Cored totals:		200.0	206.03	103	
			Site totals:		624.2	644.75	103	

Notes: DRF = drilling depth below rig floor, mbsf = meters below seafloor, DSF = drilling depth below seafloor. UTC = Universal Time Coordinated.

**Table T2.** Datum events of radiolarians, diatoms, and silicoflagellates, Holes U1339A, U1339B, U1339C, and U1339D. (See table notes.)

Datum event	Taxon	Age (ka)	Depth (mbsf)			
			Hole U1339A	Hole U1339B	Hole U1339C	Hole U1339D
LO <i>Lychnocanoma nipponica sakaii</i>	Radiolarian	52 ± 5	19.49	18.51	14.60	11.33
LO <i>Amphimelissa setosa</i>	Radiolarian	90 ± 10		37.59	34.03	29.54
LO <i>Distephanus octonarius</i>	Silicoflagellate	244 ± 47		47.25	71.59	48.16
LO <i>Proboscia curvirostris</i>	Diatom	300		75.66	90.18	66.89
LO <i>Spongodiscus</i> sp.	Radiolarian	300 ± 20		75.66	80.94	75.73
LO <i>Thalassiosira jouseae</i>	Diatom	300		75.66	90.18	57.78
LO <i>Axoprunum acquilonium</i>	Radiolarian	340 ± 90		125.30	90.18	115.07
LO <i>Stylatractus universus</i>	Radiolarian	460 ± 50		163.38	109.45	133.04
FO <i>Distephanus octangulatus</i>	Silicoflagellate	741 ± 3				190.10
LO <i>Dictyochoa subarctios</i>	Silicoflagellate	736 ± 2				190.10

Notes: For first occurrences (FO), the depth was estimated as the midpoint between the depth at which the species was first observed and the depth of the next sample below. For last occurrences (LO), the depth was estimated as the midpoint between the depth at which the species was last observed and the depth of the next sample above.



**Table T3.** Calcareous nannofossil range chart, Holes U1339A, U1339B, U1339C, and U1339D. (See table notes.) (Continued on next page.)

Core, section, interval (cm)	Martini (1971) zone	Abundance	Preservation	<i>Coccolithus pelagicus</i>	<i>Coccolithus braarudii</i>	<i>Cyclococcolithus leptoporus</i>	<i>Cyclococcolithus leptoporus</i> (small)	<i>Emiliania huxleyi</i>	<i>Gephyrocapsa</i> (medium)	<i>Gephyrocapsa</i> (large)	<i>Gephyrocapsa</i> (small)	<i>Pseudoemiliania lacunosa</i>	Other taxa	Comments
323-U1339A-1H-CC	?	A	G	D										
2H-CC		R	M-G	R	R									
3H-CC		B												
4H-CC		C	M-G	C	F				C	R				
323-U1339B-1H-CC	NN21	A	M-G	D	R			C	F					
2H-CC		R	M-G					R						
3H-CC		R	M-G					R						
4H-CC		R	M-G	R				R						
5H-CC		?	B											Reworked specimens of <i>Coccolithus miopelagicus</i> and <i>Dictyococcites</i> spp.
6H-CC			B											
7H-4, 54			R	M		R							Unidentified species (1)	Etched specimens
7H-CC			B											
8H-CC			B											
9H-CC			R	M-G	R									
10H-CC			R	M-G						R				
11H-CC			R	M	R									
12H-CC			C	M-G	F					R	C			
13H-CC			B											
14H-CC			B											
15H-CC		?	B											
16H-CC		NN19	R	M	R					R		R		<i>Pseudoemiliania lacunosa</i> ; only one specimen
17H-CC			R	M	R									Overgrowth in <i>Coccolithus pelagicus</i>
18H-CC			C	M	D									
19H-CC			B											
20H-CC			R	M	R									Overgrowth in <i>Coccolithus pelagicus</i>
21H-CC			B											
22H-CC		B												
323-U1339C-1H-CC	NN21	R	G					R						<i>Emiliania huxleyi</i> abundance based in 1 specimen
2H-CC		R	M-G	R										<i>Thoracosphaera</i> spp. observed
3H-CC		B												
4H-CC	?	R	M-G	R										Reworked specimens
5H-CC		B												
6H-CC		B												
7H-CC		B												
8H-CC		B												
9H-CC		R	M-G	R					R	R				<i>Thoracosphaera</i> spp. observed
10H-CC		F	M-G	R						F				



Table T3 (continued).

Core, section, interval (cm)	Martini (1971) zone	Abundance	Preservation	<i>Coccolithus pelagicus</i>	<i>Coccolithus braarudii</i>	<i>Cydococcolithus leptoporus</i>	<i>Cydococcolithus leptoporus</i> (small)	<i>Emiliania huxleyi</i>	<i>Gephyrocapsa</i> (medium)	<i>Gephyrocapsa</i> (large)	<i>Gephyrocapsa</i> (small)	<i>Pseudoemiliania lacunosa</i>	Other taxa	Comments	
11H-CC	?	F	M-G	F						F					
12H-CC		B													
13H-CC		F	M	F						F				Overgrowth in <i>Coccolithus pelagicus</i>	
14H-CC		B													
15H-CC		B													
16H-CC		B													
17H-CC		B													
18H-CC		B													Maybe 1 extremely etched specimen of <i>Coccolithus pelagicus</i>
19H-CC		R	M-G	R						R				Etched specimens	
20H-CC		R	M-G	R						R					
21H-CC		R	M							R					
323-U1339D-	NN21	C	M-G	D			F							Reworked individuals present	
1H-CC		R	M	R											
2H-CC		B													
3H-CC		C	M-G	C			R	R	C						
4H-CC		B												Reworked individuals present	
5H-CC		B												Reworked individuals present	
6H-CC		B												Reworked individuals present	
7H-CC		B												Reworked individuals present	
8H-CC		B													
9H-CC		R	P		R										
10H-CC		B													
11H-CC	B														
12H-CC	R	M							R						
13H-CC	C	M-G	R					F	C						
14H-CC	F	M	R						F						
15H-CC	B														
16H-CC	F	M	F	R				R	R					Overgrowth in <i>Coccolithus pelagicus</i>	
17H-CC	B														
18H-CC	B														
19H-CC	B														
20H-CC	B														
21H-CC	B														
22H-CC	B														

Notes: Abundance: A = abundant, C = common, F = few, R = rare, B = barren. Preservation: G = good, M = moderate, P = poor. ? = zone uncertain.

Table T4. Planktonic foraminifer range chart, Holes U1339A, U1339B, U1339C, and U1339D. (See table notes.) (Continued on next page.)

Core, section	Abundance	Preservation	<i>Globigerina bullioides</i>	<i>Globigerina umbilicata</i>	<i>Neogloboquadrina pachyderma</i> (dex)	<i>Neogloboquadrina pachyderma</i> (sin)	<i>Turborotalia quinqueloba</i>	Other observations
323-U1339A- Mudline	F							
1H-CC	D	G	R	R		D		Abundant siliciclastics
2H-CC	A	G	R			A		Abundant siliciclastics
3H-CC	P	G				P		Few siliciclastics
4H-CC	F	G	P			F		Dominant siliciclastics
323-U1339B- Mudline	B							
1H-CC	A	G	D		F	P		Abundant siliciclastics
2H-CC	R	G	R					Abundant siliciclastics
3H-CC	A	G	A		R			Few siliciclastics
4H-CC	A	G	A		F	P	P	Abundant siliciclastics
5H-CC	A	G	D	P	R	P		Abundant siliciclastics. Tests are yellow, Fe coated?
6H-CC	P	G	P					Few siliciclastics
7H-CC	F	G	F			P		Few siliciclastics
8H-CC	P	G	P					Abundant siliciclastics
9H-CC	B							Abundant siliciclastics
10H-CC	R	G	R		P		P	Dominant siliciclastics. Rock fragment >1 cm
11H-CC	P	G	P		P			Abundant siliciclastics
12H-CC	A	G	A		P	P		Few siliciclastics
13H-CC	R	G	R					Abundant siliciclastics
14H-CC	P	G	P		P	P		Abundant siliciclastics
15H-CC	P	G	P		P			Dominant siliciclastics
16H-CC	B							Dominant siliciclastics
17H-CC	A	G	A	F	P			Abundant siliciclastics
18H-CC	A	G	F	A	P			Dominant siliciclastics
19H-CC	A	G	A		P	P		Dominant siliciclastics
20H-CC	P	G	P	P		P		Dominant siliciclastics
21H-CC	P	G	P		P			Dominant siliciclastics
22H-CC	B							Dominant siliciclastics
323-U1339C- Mudline	B							
1H-CC	A	G		A	F	F		Few siliciclastics
2H-CC	A	G		A	F	R		Abundant siliciclastics
3H-CC	R	G		R	P			Abundant siliciclastics
4H-CC	F	G		F	P			Dominant siliciclastics
5H-CC	A	G		A	F			Dominant siliciclastics
6H-CC	A	G		A	R			Dominant siliciclastics
7H-CC	A	G		A	R			Dominant siliciclastics
8H-CC	P	G		P				Abundant siliciclastics
9H-CC	A	G	P	A	P			Few siliciclastics
10H-CC	A	G		A	R			Abundant siliciclastics
11H-CC	A	G		A	F		P	Abundant siliciclastics
12H-CC	B							Abundant siliciclastics
13H-CC	A	G		A		P		Abundant siliciclastics
14H-CC	R	G		R				Abundant siliciclastics
15H-CC	A	G		A	P	P		Abundant siliciclastics
16H-CC	P	P		P	P			Abundant siliciclastics
17H-CC	D	G		D	R			Dominant siliciclastics
18H-CC	R	G		R				Dominant siliciclastics
19H-CC	A	G	F	A	R			Few siliciclastics
20H-CC	A	G	A	A	A			Abundant siliciclastics
21H-CC	A	G	P	A	R			Few siliciclastics
323-U1339D- Mudline	A	G		A	F	R		Dominant siliciclastics



Table T4 (continued).

Core, section	Abundance	Preservation	<i>Globigerina bulloides</i>	<i>Globigerina umbilicata</i>	<i>Neogloboquadrina pachyderma</i> (dex)	<i>Neogloboquadrina pachyderma</i> (sin)	<i>Turborotalia quinqueloba</i>	Other observations
1H-CC	A	G	A	F	F			Dominant siliciclastics
2H-CC	A	G	A	R				Dominant siliciclastics
3H-CC	F	G	F	P				Dominant siliciclastics
4H-CC	A	G	A	F				Dominant siliciclastics
5H-CC	R	G	R					Dominant siliciclastics
6H-CC	D	G	D	F		P		Dominant siliciclastics
7H-CC	F	G	F	R				Dominant siliciclastics
8H-CC	A	G	A	F	R			Dominant siliciclastics
9H-CC	B							Dominant siliciclastics
10H-CC	F	M	F					Few siliciclastics
11H-CC	B							Few siliciclastics
12H-CC	P	M	P	P				Few siliciclastics
13H-CC	A	G	A	P				Abundant siliciclastics
14H-CC	A	G	A	P				Abundant siliciclastics
15H-CC	A	G	P	A	R	P		Abundant siliciclastics
16H-CC	A	G	D	F	P			Dominant siliciclastics
17H-CC	R	M	R	R				Dominant siliciclastics
18H-CC	A	M	R	A	F	R		Dominant siliciclastics
19H-CC	A	G	R	A	R	R		Dominant siliciclastics
20H-CC	B							Dominant siliciclastics
21H-CC	R	M	R	R	R	P		Dominant siliciclastics
22H-CC	R	M	P	R				Abundant siliciclastics

Notes: Abundance: D = dominant, A = abundant, F = few, R = rare, P = present, B = barren. Preservation: VG = very good, G = good, M = moderate, P = poor. Dex = dextral, sin = sinistral.

Table T5. Benthic foraminifer range chart, Hole U1339A. (See table notes.)

Core, section, interval (cm)	Abundance		Preservation										Observations								
	D	A	Alabaminella weddellensis	Bolivina sp. 1	Cibicides lobatulus	Elphidium cf. batialis	Globobulimina pacifica	Globocassidulina sp.	Islandiella norcrossi	Nonionella labradorica	Nonionella turgida digitata	Oridorsalis umbonatus		Pullenia sp. 1	Pygmaeistrion aff. hispida	Pyrgo sp.	Stairforthia spp.	Triloculina sp.	Triloculina sp. 1	Uvigerina auberiana	Uvigerina cf. peregrina
323-U1339A-1H-CC	D	G	R	R	A	R	R	D	F	R	R	R	R	R	F	R	R	R	F	F	Abundant siliciclastics
2H-CC	A	G		F	D	R	R	D	F	R	R	R	R	R	F	R	R	R	R	R	Abundant siliciclastics
3H-CC	F	G		R	R	F	R	A	F	R	R	R	R	R	F	R	R	R	R	R	Few siliciclastics
4H-3, 156-159	R	G			A	F	R	A	A	R	R	R	P								Abundant siliciclastics
4H-CC	A	G			F			R	R									R	F		Dominant siliciclastics

Notes: Abundance: D = dominant, A = abundant, F = few, R = rare, P = present. Preservation: G = good.

Table T6. Benthic foraminifer range chart, Hole U1339B. (See table notes.)

Core, section	Abundance		Preservation															Observations					
	D	A	Alabaminella weddellensis	Bolivina sp.	Brizalina earlandi	Cibicides lobatulus	Elphidium cf. batialis	Elphidium sp.	Glandulina sp.	Globobulimina pacifica	Islandiella norcrossi	Nodosaria aff. pyrula	Nonionella labradorica	Nonionella turgida digitata	Oridorsalis umbonatus	Pullenia sp. 1	Stairforthia spp.		Triloculina sp.	Triloculina sp. 1	Uvigerina auberiana	Uvigerina cf. peregrina	Valvulineria sp.
323-U1339B-1H-CC	A	G		P					A	F		F	A		P	F		P	P		R		Abundant siliciclastics
2H-CC	F	M					A		A			R	P					P	P		F		Abundant siliciclastics
3H-CC	D	G					F		D	P		A					A						Few siliciclastics
4H-CC	F	M					D		R						R								Abundant siliciclastics
5H-CC	D	G		P		A			F			F	F		D						R		Abundant siliciclastics, yellowish tests
6H-CC	F	G							F			A	R	P				R	D				Few siliciclastics, pyrite tubes
7H-CC	R	M					F		F								F						Few siliciclastics
8H-CC	R	P		P					R	R		R						P	A				Abundant siliciclastics, dominant quartz
9H-CC	R	M					P		P	P		P			A					R			Abundant siliciclastics
10H-CC	R	M					F		F										A				Dominant siliciclastics
11H-CC	A	P					D		R					P	R	P					P		Abundant siliciclastics, wood fragment
12H-CC	F	G					F		P							A					D		Few siliciclastics, dominant quartz
13H-CC	A	G					F		A			A									F		Abundant siliciclastics
14H-CC	D	G					R		A	F		F			F		P				D	F	Abundant siliciclastics
15H-CC	R	G					A		R			R											Dominant siliciclastics
16H-CC	R	G					D	F															Dominant siliciclastics
17H-CC	D	G		R			D		F	R					F						F		Abundant siliciclastics, many broken tests
18H-CC	D	M					D		R				P		F						F		Dominant siliciclastics, many broken yellowish tests
19H-CC	R	G					P		P												R		Dominant siliciclastics
20H-CC	F	G					D		R			R	P		P						R		Dominant siliciclastics
21H-CC	A	G		P		A		P	P	F		R							F	A			Dominant siliciclastics
22H-CC	R	G	P	P		R		P	P														Dominant siliciclastics

Notes: Abundance: D = dominant, A = abundant, F = few, R = rare, P = present. Preservation: G = good, M = moderate, P = poor.





Table T8. Benthic foraminifer range chart, Hole U1339D. (See table notes.)

Core, section	Abundance	Preservation	<i>Alabaminella weadellensis</i>	<i>Brizalina earlandi</i>	<i>Bullimina</i> sp.	<i>Cibicides lobatulus</i>	<i>Elphidium</i> cf. <i>batalis</i>	<i>Elphidium</i> sp.	<i>Epistominella</i> sp.	<i>Glandulina</i> sp.	<i>Globbulimina pacifica</i>	<i>Globocassidulina</i> sp.	<i>Islandiella norcrossi</i>	<i>Lagena</i> sp.	<i>Lenticulina</i> sp.	<i>Melonis barleeaanum</i>	<i>Nonionella labradorica</i>	<i>Nonionella turgida</i>	<i>Nonionella turgida digitata</i>	<i>Oridarsalis umbonatus</i>	<i>Planulina wuellerstorfi</i>	<i>Pullenia</i> sp. 1	<i>Pygmaeistrion</i> cf. <i>hispidus</i>	<i>Stainforthia</i> sp.	<i>Triloculina</i> sp.	<i>Triloculina</i> sp. 1	<i>Uvigerina auberiana</i>	<i>Uvigerina</i> cf. <i>peregrina</i>	<i>Valvulineria</i> sp.	Observations		
323-U1339D-																																
Mudline	R	G					F	A			R		R				F														Dominant siliciclastics	
1H-CC	A	G					A						A				A		F					R	P	P	R	P			Dominant siliciclastics	
2H-CC	R	G	R	P		R	P		P		P		A	P				P						R							Dominant siliciclastics	
3H-CC	R	G					F	R		R			R												P							Dominant siliciclastics
4H-CC	F	G					A	P		P							P	R	P						P		P	F			Dominant siliciclastics	
5H-CC	R	G	R				F						P										P	P							Dominant siliciclastics	
6H-CC	R	G					F			R	R		P												R	A					Dominant siliciclastics	
7H-CC	R	G	P	P			A	R		R	R		R			P	R							R	A						Dominant siliciclastics	
8H-CC	F	M	P	P					P	P			R			P	R	P							P						Dominant siliciclastics	
9H-CC	R	G	P				A	F			P		R	P				P					P						A		Dominant siliciclastics	
10H-CC	F	G	P							P									P				P	P			R				Few siliciclastics	
11H-CC	F	M					R			P													P	P							Few siliciclastics	
12H-CC	F	M					F			P			R				P	P						R							Few siliciclastics	
13H-CC	A	G					A			F			F				F		P					R	P		R	R			Abundant siliciclastics	
14H-CC	A	G		P			D	R			P		P				P	R						P							Abundant siliciclastics	
15H-CC	F	G	P				R	R		P	P		P																			Abundant siliciclastics
16H-CC	F	G	P	P			D	P		P	P		F		P		P		P					F			P	F			Dominant siliciclastics	
17H-CC	F	G	R				R			P			F											R							Dominant siliciclastics, yellow tests	
18H-CC	R	G	R				A				R													F			P				Dominant siliciclastics	
19H-CC	F	G					F	P		R			R				R														Dominant siliciclastics	
20H-CC	F	G	P	R			F	P					F																		Dominant siliciclastics	
21H-CC	R	G					A				R		P					P	P					P			P	P			Dominant siliciclastics	
22H-CC	F	M					F											R							R						Abundant siliciclastics, yellow tests	

Notes: Abundance: D = dominant, A = abundant, F = few, R = rare, P = present, B = barren. Preservation: G = good, M = moderate, P = poor.





Table T10. Diatom range chart, Hole U1339B. (See table note.) (Continued on next page.)

Core, section, interval (cm)	Depth (mbsf)	<i>Actinocyclus curvatus</i>	<i>Actinocyclus ochotensis</i>	<i>Actinocyclus</i> sp. 1	<i>Asteromphalus brookei</i>	<i>Asteromphalus robustus</i>	<i>Azpeitia</i> cf. <i>tabularis</i>	<i>Bacterosira fragilis</i>	<i>Chaetoceros</i> resting spore	<i>Cocconeis costata</i>	<i>Cocconeis placentula</i>	<i>Coscinodiscus marginatus</i>	<i>Coscinodiscus oculus-iridis</i>	<i>Coscinodiscus</i> sp. 1	<i>Cyclotella</i> spp.	<i>Cymbella</i> spp.	<i>Delphineis kippae</i>	<i>Delphineis surirella</i>	<i>Diploneis interrupta</i>	<i>Fragilaria</i> spp.	<i>Fragilariopsis cylindrus</i>	<i>Fragilariopsis oceanica</i>	<i>Gomphonema</i> spp.	<i>Navicula distans</i>	<i>Navicula</i> spp.	<i>Neodenticula seminiae</i>	<i>Nitzschia</i> spp.	<i>Odontella aurita</i>	<i>Paralia sol</i>	<i>Paralia sulcata</i>	<i>Pinnularia gibba linearis</i>	<i>Pinnularia</i> spp.	<i>Porosira glacialis</i>	<i>Proboscia curvirostris</i>	<i>Rhabdonema</i> spp.	<i>Rhizosolenia hebetata</i> f. <i>hebetata</i>					
323-U1339B-																																									
1H-CC	3.91	F R						T F R T									F					T				C	T C														
2H-CC	13.65	C F						C F T									T F					T				A	T T C														
3H-CC	23.36	C T					T T F T										T					C				C	C									T T					
4H-CC	32.91	R			T			C				T T								T		F				A	F	T					T		T T						
5H-CC	42.17	F						C F T										T T				T F				A	C	F									F				
6H-CC	52.23	C						A T														T F				C	C	T										T			
7H-CC	61.50	F						T F T										T				T				A	T											T			
8H-CC	70.85	C T						T T								T						A				T F	T	T T				T T						F			
9H-2, 45	71.58	A						A					T													C	C												F		
9H-4, 45	74.54	A						C A				C														C	F												F		
9H-CC	80.37		F					F A T						T								T				C	C									T T		T			
10H-CC	89.88	F C						F F				F					F T					T			T T	T F	F												T		
11H-CC	99.25	F F						F				F T														A	T F													T	
12H-CC	108.40	C F			T			F				C														F														T	
13H-CC	108.89	C F	F T				T T T					T														C		F					T							T	
14H-CC	120.47	C F						F F T																		C		C													T C T
15H-CC	130.02	F C						F C T				F														F	T	T					T							F	
16H-CC	139.41	C F						T T				T C						T								C	T	T												C	
17H-CC	148.57	C		T			T T C T								T		T T									C	C	T T												T	
18H-CC	158.79	F F						T A						T												C	C													T T	
19H-CC	167.86							T																		A	T	C												C	
20H-CC	177.31	C	T					F				T														A	T														
21H-CC	187.60	C						T																		C														F F	
22H-CC	196.83	R T						C A				F														A														F T	

Note: Abundance: A = abundant, C = common, F = few, R = rare, T = trace.



Table T10 (continued).

Core, section, interval (cm)	Depth (mbsf)	<i>Rhizosolenia hebetata</i> f. <i>hiemalis</i>	<i>Rhizosolenia hebetata</i> f. <i>semispina</i>	<i>Rhizosolenia styliformis</i>	<i>Rhopalodia</i> spp.	<i>Roperia tessellata</i>	<i>Stephanopyxis turris</i>	<i>Thalassionema bacillarum</i>	<i>Thalassionema nitzschioides</i>	<i>Thalassiosira anguste-lineata</i>	<i>Thalassiosira antarctica</i> spores	<i>Thalassiosira decipiens</i>	<i>Thalassiosira eccentrica</i>	<i>Thalassiosira gravida</i>	<i>Thalassiosira hyalina</i>	<i>Thalassiosira jouseae</i>	<i>Thalassiosira latimarginata</i> s.l.	<i>Thalassiosira lineata</i>	<i>Thalassiosira nordenskiöldii</i>	<i>Thalassiosira oestrupii</i>	<i>Thalassiosira pacifica</i>	<i>Thalassiosira</i> spp.	<i>Thalassiothrix longissima</i>	Diatom Zone (NPD) in Yanagisawa and Akiba (1998)	
323-U1339B-																									
1H-CC	3.91																								
2H-CC	13.65																								
3H-CC	23.36																								
4H-CC	32.91																								
5H-CC	42.17		F				T		T																
6H-CC	52.23		F																						
7H-CC	61.50		F																						
8H-CC	70.85																								
9H-2, 45	71.58																								
9H-4, 45	74.54																								
9H-CC	80.37																								
10H-CC	89.88																								
11H-CC	99.25																								
12H-CC	108.40																								
13H-CC	108.89																								
14H-CC	120.47																								
15H-CC	130.02																								
16H-CC	139.41																								
17H-CC	148.57																								
18H-CC	158.79																								
19H-CC	167.86																								
20H-CC	177.31																								
21H-CC	187.60																								
22H-CC	196.83																								



Table T11. Diatom range chart, Hole U1339C. (See table note.) (Continued on next page.)

Core, section, interval (cm)	Depth (mbsf)	<i>Achnanthes</i> spp.	<i>Actinocyclus curvatus</i>	<i>Actinocyclus ochotensis</i>	<i>Actinocyclus vulgaris</i>	<i>Actinopterychus senarius</i>	<i>Arachnoidiscus</i> spp.	<i>Azpeitia</i> cf. <i>tabularis</i>	<i>Bacterosira fragilis</i>	<i>Chaetoceros</i> resting spore	<i>Cocconeis costata</i>	<i>Cocconeis disculus</i>	<i>Cocconeis placentula</i>	<i>Cocconeis scutellum</i>	<i>Coscinodiscus marginatus</i>	<i>Coscinodiscus oculus-iridis</i>	<i>Delphineis kippae</i>	<i>Delphineis surirella</i>	<i>Diploneis bombus</i>	<i>Diploneis smithii</i>	<i>Eunotia</i> spp.	<i>Fragilaria</i> spp.	<i>Fragilariopsis cylindrus</i>	<i>Fragilariopsis olearica</i>	<i>Gomphonema</i> spp.	<i>Grammatophora arcuata</i>	<i>Navicula</i> spp.	<i>Neodenticula seminiae</i>	<i>Nitzschia</i> spp.	<i>Odontella aurita</i>	<i>Paralia sol</i>			
323-U1339C-1H-CC	9.68	T	F						F	R			F				F				R	T	F				C		F					
2H-CC	19.42		C	F					T	F	R												F				A		T	C				
3H-CC	29.09		F						T	F	F							R									C		R	C				
4H-CC	38.86	T	F				T	T		C	T					R							T	T		T	C		R	R				
5H-CC	48.39		C						R						T	T											C			F				
6H-CC	57.84		F						T	F	F					R	T	R					R		T	C			T	F				
7H-CC	66.55		A																								C			F				
8H-CC	76.53											C															A							
9H-CC	85.24		A																											A				
10H-1, 25	86.05		A						T						C												C			C				
10H-2, 2	86.55		A																				R				C			C				
10H-CC	95.01		C						F				T		R												C			C				
12H-CC	114.36		C						F						T	T											C			C				
13H-CC	123.71		R	F		T			T	F							F										A	T	T	T	T			
14H-CC	133.99		F						F		F																A		R	R				
15H-CC	142.92		C	R					F	F	R				F	T	R										A		F	T				
16H-CC	146.52		C												C	T														T				
17H-CC	157.02		C							F	T				F	T		T									C			F				
18H-CC	165.92		C						T						F	F											A			T				
19H-CC	176.38		F												F										T		A		R	F				
20H-CC	185.75		C		T										F												A			A				
21H-CC	195.24		C						F	F							T						T				A			R				

Note: A = abundant, C = common, F = few, R = rare, T = trace.



Table T11 (continued).

Core, section, interval (cm)	Depth (mbsf)	<i>Paralia sulcata</i>	<i>Porosira glacialis</i>	<i>Proboscia curvirostris</i>	<i>Rhabdonema</i> spp.	<i>Rhizosolenia hebetata</i> f. <i>hebetata</i>	<i>Rhizosolenia hebetata</i> f. <i>hiemalis</i>	<i>Rhizosolenia hebetata</i> f. <i>semispina</i>	<i>Stephanopyxis turris</i>	<i>Thalassionema bacillaris</i>	<i>Thalassionema nitzschioides</i>	<i>Thalassiosira antarctica</i> spore	<i>Thalassiosira decipiens</i>	<i>Thalassiosira eccentrica</i>	<i>Thalassiosira hyalina</i>	<i>Thalassiosira jouseae</i>	<i>Thalassiosira latimarginata</i> s.l.	<i>Thalassiosira lineata</i>	<i>Thalassiosira lucustris</i>	<i>Thalassiosira nordenskiöldii</i>	<i>Thalassiosira oestrupii</i>	<i>Thalassiothrix longissima</i>	Diatom Zone (NPD) in Yanagisawa and Akiba (1998)
323-U1339C-																							
1H-CC	9.68	F	F		F	T		F	A		F	A		F		R		C					
2H-CC	19.42								A			A				R				C			
3H-CC	29.09		R		F	T	T	T	A		F	A	T	T		R		T					
4H-CC	38.86	T			F				C		T	C	F			R				C			
5H-CC	48.39	F			F				A			A	F	T		R				C			
6H-CC	57.84	C			R				A			A	R			R				T	C	T	
7H-CC	66.55					C			A			A				R							
8H-CC	76.53				C				A			A				R							
9H-CC	85.24								A			A				R						A	
10H-1, 25	86.05		F		F	T			C		C	C				R	R					C	
10H-2, 2	86.55		C		R	R			C		C	A				R	F					R	
10H-CC	95.01		T	R		C	C		A		R	A		R	F				T				
12H-CC	114.36		R				T	T	A			A		R		C				T	T		
13H-CC	123.71	F		T	R		T		C			C		T	C	F				C	T		
14H-CC	133.99	F			R				C			C		R	A	F							
15H-CC	142.92	T	T	F					A			A		T	C	C					C	T	
16H-CC	146.52	T		C	R	R	R	T	A			A			R	C							
17H-CC	157.02	F					R	R	A		T	A		T	C	F	T				C		
18H-CC	165.92		T	T	T	T	R	F	A		R	A		T	C	F			F			R	
19H-CC	176.38					T	R		A		R	A	T	T	C	C		T				F	
20H-CC	185.75	T	F		T	T	T		C			C		T	F	F					R		
21H-CC	195.24	R				T	C		C			C	T	R	F	C			T	F			



Table T12. Diatom range chart, Hole U1339D. (See table note.) (Continued on next page.)

Core, section	Depth (mbsf)	<i>Actinocyclus curvatulus</i>	<i>Actinocyclus ochotensis</i>	<i>Aspetia nodulifera</i>	<i>Aspetia cf. tabularis</i>	<i>Bacterosira fragilis</i>	<i>Chaetoceros</i> resting spore	<i>Cocconeis costata</i>	<i>Cocconeis placentula</i>	<i>Coscinodiscus marginatus</i>	<i>Coscinodiscus oculus-iridis</i>	<i>Delphineis surirella</i>	<i>Detonula confervacea</i>	<i>Diploneis interrupta</i>	<i>Diploneis</i> spp.	<i>Eunotia praerupta</i>	<i>Fragilaria cylindrus</i>	<i>Fragilaria oceanica</i>	<i>Grammatophora arcumata</i>	<i>Navicula distans</i>	<i>Navicula</i> spp.	<i>Neodenticula seminiae</i>	<i>Nitzschia</i> spp.	<i>Odontella aurita</i>	<i>Paralia sol</i>	<i>Paralia sulcata</i>	<i>Pinnularia</i> spp.	<i>Porosira glacialis</i>	<i>Proboscia curvirostris</i>	<i>Rhabdonema</i> spp.	<i>Rhizosolenia hebetata</i> f. <i>hebetata</i>	
323-U1339D-																																
1H-CC	6.52	C	F			F					T				T							C	T	C								
2H-CC	16.04	C				T		C									R					A	T	C								
3H-CC	25.59	C				F		C	F		T	T					T					C		F	T					C	T	
4H-CC	33.38	F		F				C	T								R	T				C	R	F		C					T	
5H-CC	43.24	C				F		C	R		F	T	T		T							C	T	T		F					C	
6H-CC	52.97	F				C		C				T				T	C					C	C	C		F		T		F	R	
7H-CC	62.48	F				T		C			F	R				T	T					A		F							F	
8H-CC	71.20	A				R		C	T	T			T				R	F				C					T	F		T		
9H-CC	80.15	F				T		A	T													R		C					T		T	
10H-CC	90.43	C				T		A			C	R	T									C		T		F				T		
11H-CC	100.38	C						A			R											C			F	T		T				
12H-CC	110.15	F	R		T			C	T			T			T		F	C				A		F								R
13H-CC	119.89	F		T	R			C	C	T		T	F				T	C				C			F							
14H-CC	128.83	C	T		R			T	T		T						T	F				C		F					F	T		
15H-CC	137.14	F	F					R			T	T										D			F				T			
16H-CC	147.16	A		T		F		F	T								T					F							F		F	
17H-CC	157.88	C				R		T	T													C							C		T	
18H-CC	167.18	C									R	T										C							C			
19H-CC	176.77	C	F		T			C	T		T	R										A	T		T					T	T	T
20H-CC	185.99	C											T									A							T	T	F	
21H-CC	194.11	C				T		F	T		T											A			F				R		F	
22H-CC	200.77	C				F		C		F			R									A						T				

Note: D = dominant, A = abundant, C = common, F = few, R = rare, T = trace.



Table T12 (continued).

Core, section	Depth (mbsf)	<i>Rhizosolenia hebetata</i> f. <i>hiemalis</i>	<i>Rhizosolenia hebetata</i> f. <i>semispina</i>	<i>Rhizosolenia styliformis</i>	<i>Stauroneis</i> spp.	<i>Stellarima microtrias</i>	<i>Stephanopyxis turris</i>	<i>Tetracyclus lacustris</i>	<i>Thalassionema nitzschooides</i>	<i>Thalassiosira antarctica</i> spore	<i>Thalassiosira decipiens</i>	<i>Thalassiosira eccentrica</i>	<i>Thalassiosira hyalina</i>	<i>Thalassiosira jouseae</i>	<i>Thalassiosira latimarginata</i> s.l.	<i>Thalassiosira lineata</i>	<i>Thalassiosira nordenskiöldii</i>	<i>Thalassiosira oestrupii</i>	<i>Thalassiosira pacifica</i>	<i>Thalassiosira</i> spp.	<i>Thalassiothrix longissima</i>	Diatom Zone (NPD) in Yanagisawa and Akiba (1998)
323-U1339D-																						
1H-CC	6.52	R	T						R	C	T	R	C				F	F				
2H-CC	16.04						T		T	C		T	C				F	F			T	
3H-CC	25.59								T	A			C	T								
4H-CC	33.38			C			F		C	C			T	C				F				<i>Neodenticula seminae</i> (NPD12)
5H-CC	43.24			R					T	C			C	C				C	C			
6H-CC	52.97			F					R	A			C	C				C	C		F	T
7H-CC	62.48			C					F	C			T	C			T	C	C		T	R
8H-CC	71.20								F	F			C	C				C				R
9H-CC	80.15	T							R	C		T	C	F								
10H-CC	90.43								T	C			T	T							F	
11H-CC	100.38	T							F	C	T	R	F	T			T					R
12H-CC	110.15			F					T	C	T		T	C				F				T
13H-CC	119.89			F			T		C	C			T	C	T			R				F
14H-CC	128.83						T		T	A			F	C				R				T
15H-CC	137.14			F					F	C			T	C	F			F				<i>Proboscia curvirostris</i> (NPD11)
16H-CC	147.16						R	T	F	C			T	C				C				F
17H-CC	157.88			T			R		T	A			T	C	C			R				F
18H-CC	167.18						T		A			R	T	F								
19H-CC	176.77						F		C			T	T	C	C			C				R
20H-CC	185.99	F	T				C		C	A			T	R								T
21H-CC	194.11		R						C				T	F	F	R		R				
22H-CC	200.77			T		T	R		F				T	C			T	R				F



Table T13. Silicoflagellate and ebridian range chart, Holes U1339A, U1339B, U1339C, and U1339D. (See table notes.)

Core, section	Abundance	Preservation	Silicoflagellates						Ebridians	
			Aberrant forms <i>Dictyocha subarctios</i>	<i>Distephanus boliviensis boliviensis</i>	<i>Distephanus medianocticol</i>	<i>Distephanus medianocticol</i> *	<i>Distephanus octangulatus</i>	<i>Distephanus octonarius</i>		<i>Distephanus speculum</i>
323-U1339A-										
2H-CC	B	G								T
3H-CC	B	G				R				F
4H-CC	B	G				T				
323-U1339B-										
2H-CC	B	G			T					R
4H-CC	B	G					R		R	
5H-CC	B	G	T			T	T		R	A
6H-CC	B	G				T		T		T
7H-CC	B	G			T			T	R	T
9H-CC	B	G						T		T
11H-CC	B	G	T		T	R		T	F	C
13H-CC	B	G				T		F	R	F
15H-CC	B	M			T			T		
17H-CC	B	M								T
18H-CC	B	M			R		T		T	R
19H-CC	B	M		T			T			R
20H-CC	B	M	T		R	F	R	T	T	
21H-CC	B									
22H-CC	B	G			F		T	F		R
323-U1339C-										
5H-CC	B	G							T	F
6H-CC	B	G								F
7H-CC	B	G								F
8H-CC	B	M				T		T		
9H-CC	B									
10H-CC	B	M				R			R	F
12H-CC	B	M					T			T
14H-CC	B	M								T
16H-CC	B	M			R					T
18H-CC	B	M					T			R
19H-CC	B	M		T			T			R
20H-CC	B	M					T			
21H-CC	B	M								T
323-U1339D-										
4H-CC	B	M					T		T	
5H-CC	B	M								R
6H-CC	B	M						R		
7H-CC	B	M				R		T		C
8H-CC	B	M								
10H-CC	B	M				R	T		R	F
20H-CC	B	M			F	T	R	T		
21H-CC	B	M	T						T	T
22H-CC	B	M	F					R		R

Notes: \* = with short radial spines. Abundance: A = abundant, C = common, F = few, R = rare, T = trace, B = barren. Preservation: G = good, M = moderate.



Table T14. Radiolarian range chart, Holes U1339A, U1339B, U1339C, and U1339D. (See table notes.) (Continued on next page.)

Core, section	Depth (mbsf)		Abundance	Preservation	<i>Actinomma boreale</i>	<i>Amphimelissa setosa</i>	<i>Axoprunum acquilonium</i>	<i>Botryostrobus aquilonaris</i>	<i>Ceratospyrus borealis</i>	<i>Cycladophora cornutoides</i>	<i>Cycladophora davistiana</i>	<i>Dictyophimus hirundo</i>	<i>Larcopele buetschlii</i>	<i>Lychnocanoma nipponica sakaii</i>	<i>Sphaeropyle langii-robusta</i> group	<i>Spongodiscus</i> sp. (Ling, 1973)	<i>Spongopyle osculosa</i>	<i>Spongotrochus glacialis</i>	<i>Spongurus pylomaticus</i>	<i>Stylatractus universus</i>	<i>Stylochlamydidium venustum</i>	<i>Stylocictya validispina</i>
	Top	Bottom																				
323-U1339A-																						
1H-CC	4.82	4.94	F	G					F	C	F										F	F
2H-CC	14.64	14.74	F	G	F				F	C	F	F									F	F
3H-CC	24.23	24.33	F	G	F				F	F			F								F	F
4H-CC	33.79	33.89	C	G	F			F	C	F			C								F	F
323-U1339B-																						
1H-CC	3.91	4.01	F	G						F						F					F	F
2H-CC	13.65	13.75	F	G					F	C	F	F					F				F	F
3H-CC	23.36	23.36	F	G					F	F	F		F				F				F	F
4H-CC	32.91	33.01	C	G				F	F	F	F	F	C					F			F	F
5H-CC	42.17	42.27	F	G	F			F		F	F		C					F			F	F
6H-CC	52.23	52.33	F	G	F			F		C	F	F	F								F	F
7H-CC	61.50	61.60	F	G						F			F									
8H-CC	70.85	70.95	F	G	F					C	F		F									
9H-CC	80.37	80.47	F	G	F	F				C			F	F	C		F				F	F
10H-CC	89.88	89.98	F	G	F			F		F				F	F			F			F	F
11H-CC	99.25	99.35	F	G						F					F							F
12H-CC	108.40	108.48	F	M	F			F						F	F							
13H-CC	108.89	108.99	F	G	F			F		C		F		F	F							F
14H-CC	120.47	120.57	F	G						F	F	F		F	F		F					
15H-CC	130.02	130.12	F	G		F				C	F	F			F		F					
16H-CC	139.41	139.51	F	G		F																
17H-CC	148.57	148.67	F	G	F			C		F		F		F	C							
18H-CC	158.79	158.89	F	G	F	F	F	F		C	F			F	F	F	F				F	F
19H-CC	167.86	167.96	C	M	F	F	F	C		F				F	F	F	F			F	F	F
20H-CC	177.31	177.41	C	G	C	F		C	F	C	C			F	C	F	F				F	F
21H-CC	187.60	187.70	F	G	C			F	F	A	F	F		C	F	F	F	F	F	F	F	F
22H-CC	196.83	196.93	F	G		F		F	F	A	F			F	F		F			F		
323-U1339C-																						
1H-CC	9.68	9.78	C	G	F			C		C	F	F		F		F					F	F
2H-CC	19.42	19.52	C	G	F			F		C	F	F	C			F					F	F
3H-CC	29.09	29.19	C	G	F		F	F		C	F	F	F									F
4H-CC	38.86	38.96	F	G	F	F		F		C			F				F					
5H-CC	48.39	48.39	C	G		F		F		C	F	F	C	F			F					F
6H-CC	57.84	57.94	C	G		F		C		C	F	F	F									F
7H-CC	66.55	66.65	F	G				F		F		F	F				F				F	F
8H-CC	76.53	76.63	F	G	F	F		F		F	F	F	F	F			F	F			F	F
9H-CC	85.24	85.34	C	M	F			F		F	F	F			C		F					F
10H-CC	95.01	95.11	F	G		F	F	F							C							F
11H-CC	104.43	104.53	C	G	F		F	F		C					C			F				
12H-CC	114.36	114.46	F	G	F	F		F		C				F	F		F			F	F	F
13H-CC	123.71	123.81	C	G	C	F		C				F	F		F	F	F					F
14H-CC	133.99	134.09	F	G	F			F						F	F		F					F
15H-CC	142.92	143.02	F	G						F	F				F						F	
16H-CC	146.52	146.62	C	G	F	F		F		F					C							
17H-CC	157.02	157.12	C	G	F	F		F	F	F	A	F		F	F							
18H-CC	165.92	166.02	F	G	F	F		F		F	F	F										
19H-CC	176.38	176.48	F	G		F				F												
20H-CC	185.75	185.85	C	G	F	F		C	F	C	F	C		F	F	F	F			F	F	F
21H-CC	195.24	195.34	C	G				F	F	F	C				F	C						
323-U1339D-																						
1H-CC	6.52	6.62	F	G	F			F		C												F
2H-CC	16.04	16.14	C	G				C		C	F		F									C
3H-CC	25.59	25.69	C	G				F	F	A	F	F	F									F
4H-CC	33.38	33.48	F	G		F		C					F	F								F
5H-CC	43.24	43.34	F	G				F		C	F		F	F	F							F



Table T14 (continued).

Core, section	Depth (mbsf)		Abundance	Preservation	<i>Actinomma boreale</i>	<i>Amphimelissa setosa</i>	<i>Axoprunum acqilonium</i>	<i>Botryostrobus aquilonaris</i>	<i>Ceratospyrus borealis</i>	<i>Cycladophora cornutoides</i>	<i>Cycladophora davisiana</i>	<i>Dictyophimus hirundo</i>	<i>Larcopyle buetschlii</i>	<i>Lychinocanoma nipponica sakaii</i>	<i>Sphaeropyle langii-robusta</i> group	<i>Spongodiscus</i> sp. (Ling, 1973)	<i>Spongopyle osculosa</i>	<i>Spongotrochus glacialis</i>	<i>Spongurus pylomaticus</i>	<i>Stylatractus universus</i>	<i>Stylochlamydidium venustum</i>	<i>Stylocictya validispina</i>
	Top	Bottom																				
6H-CC	52.97	53.07	C	G	F				C	F	A	F	F	F	F						F	C
7H-CC	62.48	62.58	F	G						F	F				F		F			F	F	F
8H-CC	71.20	71.30	F	G	F			F		F	C		F	F			F				F	F
9H-CC	80.15	80.25	C	G	F		F	C		F	C	F	F	F		C					F	F
10H-CC	90.43	90.53	F	G				F		F						F						
11H-CC	100.38	100.48	F	G	F			F								F						
12H-CC	110.15	110.25	F	G	F			F		F		F				F		F				
13H-CC	119.89	119.99	C	G		F		F		F		F			F	F		F				
14H-CC	128.83	128.93	C	G		F		F		C					F	F		F				
15H-CC	137.14	137.24	A	G	F	C	C	C		F		F			C	C		F		F	C	
16H-CC	147.16	147.26	C	G	F	F	F	F		F					F	C		F			F	
17H-CC	157.88	157.98	C	G	F	F		F		F	C				F	C					F	F
18H-CC	167.18	167.28	F	G	F	F		F		F					F	F		F			F	
19H-CC	176.77	176.87	C	G	F	F		F		F	C		F		F			F				
20H-CC	185.99	186.09	F	G	F	F		F		C					F		F					
21H-CC	194.11	194.21	F	G		F		F				F			F	F						F
22H-CC	200.77	200.83	F	G		F		F		F		F			F							F

Notes: Abundance: A = abundant, C = common, F = few. Preservation: G = good, M = moderate.

**Table T15.** Radiolarian datum events, Holes U1339A, U1339B, U1339C, U1339D. (See table note.)

Zone	Marker species	Age (Ma)	Hole U1339A				Hole U1339B			
			Core, section		Depth (mbsf)		Core, section		Depth (mbsf)	
			Top	Bottom	Top	Bottom	Top	Bottom	Top	Bottom
<i>Botryostrobus aquilonaris</i>	T <i>Lychnocanoma nipponica sakaii</i>	0.05	2H-CC	3H-CC	14.74	24.23	2H-CC	3H-CC	13.65	23.36
	T <i>Amphimelissa setosa</i>	0.08–0.10					4H-CC	5H-CC	32.91	42.27
	T <i>Spongodiscus</i> sp.	0.28–0.32					8H-CC	9H-CC	70.85	80.47
	T <i>Axoprunum acqulonium</i>	0.25–0.43					14H-CC	15H-CC	120.47	130.12
<i>Stylatractus universonus</i>	T <i>Stylatractus universonus</i>	0.41–0.51					18H-CC	19H-CC	158.79	167.96

Note: T = top.

**Table T15 (continued).**

Zone	Marker species	Age (Ma)	Hole U1339C				Hole U1339D			
			Core, section		Depth (mbsf)		Core, section		Depth (mbsf)	
			Top	Bottom	Top	Bottom	Top	Bottom	Top	Bottom
<i>Botryostrobus aquilonaris</i>	T <i>Lychnocanoma nipponica sakaii</i>	0.05	1H-CC	2H-CC	9.68	19.52	1H-CC	2H-CC	6.52	16.14
	T <i>Amphimelissa setosa</i>	0.08–0.10	3H-CC	4H-CC	29.09	38.96	3H-CC	4H-CC	25.59	33.48
	T <i>Spongodiscus</i> sp.	0.28–0.32	8H-CC	9H-CC	76.53	85.34	8H-CC	9H-CC	71.20	80.25
	T <i>Axoprunum acqulonium</i>	0.25–0.43	9H-CC	10H-CC	85.24	95.11	12H-CC	13H-CC	110.15	119.99
<i>Stylatractus universonus</i>	T <i>Stylatractus universonus</i>	0.41–0.51	11H-CC	12H-CC	104.43	114.46	14H-CC	15H-CC	128.83	137.24



Table T17. Moisture and density, Holes U1339A and U1339B. (See table note.) (Continued on next page.)

Core, section, interval (cm)	Depth (mbsf)	Density (g/cm <sup>3</sup> )			Void ratio	Water content (%)	Porosity (%)
		Dry grain	Wet bulk	Dry bulk			
323-U1339A-							
1H-1, 49-51	0.5	2.52	1.23	0.38	6.38	69.40	86.4
1H-1, 99-101	1.0	2.23	1.22	0.39	5.19	67.99	83.9
1H-2, 49-51	2.0	2.54	1.27	0.44	5.19	65.06	83.8
1H-2, 99-101	2.5	2.50	1.38	0.63	3.18	54.45	76.1
1H-3, 49-51	3.5	2.70	1.38	0.59	3.83	56.95	79.3
1H-3, 99-101	4.0	2.74	1.41	0.64	3.53	54.67	77.9
2H-1, 49-51	5.4	2.54	1.43	0.70	2.78	50.81	73.5
2H-1, 99-101	5.9	2.68	1.40	0.62	3.53	55.21	77.9
2H-2, 49-51	6.9	2.59	1.42	0.69	2.97	51.90	74.8
2H-2, 99-101	7.4	2.74	1.44	0.69	3.16	52.02	76.0
2H-3, 49-51	8.4	2.71	1.46	0.73	2.90	50.29	74.4
2H-3, 99-101	8.9	2.53	1.46	0.76	2.47	48.08	71.2
2H-4, 29-31	9.7	2.41	1.46	0.79	2.17	46.29	68.5
2H-5, 29-31	11.2	2.43	1.39	0.65	2.90	52.93	74.3
2H-6, 29-31	12.7	2.96	1.56	0.84	2.68	46.16	72.8
3H-1, 29-31	14.7	2.75	1.55	0.86	2.32	44.54	69.9
3H-2, 29-31	16.2	2.60	1.50	0.81	2.33	46.02	70.0
3H-3, 29-31	17.7	2.78	1.56	0.87	2.30	44.09	69.7
3H-4, 29-31	19.2	2.57	1.48	0.78	2.40	47.06	70.6
3H-5, 29-31	20.7	2.62	1.48	0.77	2.53	47.82	71.7
3H-6, 29-31	22.2	2.64	1.41	0.65	3.29	53.93	76.7
3H-7, 29-31	23.7	2.65	1.49	0.79	2.50	47.27	71.5
4H-1, 29-31	24.2	2.61	1.36	0.59	3.72	57.07	78.8
4H-2, 29-31	25.7	2.46	1.43	0.72	2.56	49.69	71.9
4H-3, 29-31	27.2	2.62	1.45	0.72	2.81	50.34	73.7
4H-4, 29-31	28.7	2.52	1.46	0.75	2.50	48.44	71.4
4H-5, 29-31	30.2	2.62	1.39	0.62	3.47	55.37	77.6
4H-6, 29-31	31.7	2.61	1.32	0.51	4.43	61.02	81.6
4H-7, 29-31	33.2	2.66	1.38	0.60	3.71	56.56	78.8
323-U1339B-							
5H-1, 59-61	33.1	2.58	1.51	0.82	2.25	45.40	69.2
5H-2, 59-61	34.6	2.66	1.53	0.84	2.30	45.17	69.7
5H-3, 59-61	36.1	2.79	1.57	0.88	2.28	43.81	69.5
5H-4, 59-61	37.6	2.62	1.53	0.85	2.19	44.37	68.6
5H-5, 59-61	39.1	2.73	1.56	0.88	2.21	43.61	68.8
5H-6, 59-61	40.6	2.85	1.56	0.86	2.45	44.97	71.0
5H-7, 59-61	42.1	2.52	1.47	0.77	2.40	47.47	70.6
6H-1, 59-61	42.6	2.70	1.57	0.89	2.13	42.99	68.1
6H-2, 59-61	44.1	2.56	1.52	0.85	2.10	43.98	67.8
6H-3, 59-61	45.6	2.83	1.63	0.97	2.01	40.39	66.7
6H-4, 59-61	47.1	1.27	1.14	0.66	0.96	42.33	48.9
6H-5, 59-61	48.6	2.59	1.55	0.89	2.02	42.75	66.9
6H-6, 59-61	50.1	2.66	1.51	0.82	2.37	45.88	70.3
6H-7, 59-61	51.6	2.58	1.53	0.86	2.11	43.82	67.8
7H-1, 59-61	52.1	2.66	1.46	0.74	2.78	49.71	73.5
7H-2, 59-61	53.6	2.53	1.45	0.75	2.52	48.64	71.6
7H-3, 59-61	55.1	2.55	1.36	0.58	3.65	57.14	78.5
7H-4, 59-61	56.6	2.78	1.66	1.03	1.78	38.05	64.0
7H-5, 59-61	58.1	2.62	1.59	0.96	1.82	40.02	64.6
7H-6, 59-61	59.6	2.70	1.58	0.92	2.03	41.83	67.0
7H-7, 29-31	61.1	2.54	1.49	0.80	2.28	46.15	69.5
8H-1, 59-61	61.6	2.43	1.43	0.73	2.43	48.84	70.9
8H-2, 59-61	63.1	2.65	1.64	1.02	1.68	37.84	62.7
8H-3, 59-61	64.6	2.65	1.52	0.83	2.30	45.23	69.7
8H-4, 59-61	66.1	2.75	1.57	0.90	2.18	43.05	68.5
8H-5, 59-61	67.6	2.57	1.57	0.92	1.87	41.10	65.2
8H-6, 59-61	69.1	2.71	1.65	1.03	1.71	37.74	63.1
8H-7, 59-61	70.3	2.56	1.62	1.01	1.59	37.46	61.4
9H-1, 29-31	70.8	2.78	1.62	0.97	1.95	40.19	66.1
9H-2, 29-31	71.4	2.57	1.54	0.89	1.99	42.62	66.6
9H-3, 29-31	72.9	2.71	1.62	0.98	1.86	39.70	65.0
9H-4, 29-31	74.4	2.49	1.48	0.80	2.21	45.93	68.9
9H-5, 29-31	75.9	2.63	1.49	0.79	2.46	47.06	71.1
9H-6, 29-31	77.4	2.69	1.54	0.85	2.28	44.71	69.5
9H-7, 29-31	78.8	2.53	1.54	0.89	1.93	42.19	65.8
10H-1, 39-41	80.4	2.75	1.49	0.77	2.74	48.59	73.3

Table T17 (continued).

Core, section, interval (cm)	Depth (mbsf)	Density (g/cm <sup>3</sup> )			Void ratio	Water content (%)	Porosity (%)
		Dry grain	Wet bulk	Dry bulk			
10H-2, 39-41	81.4	2.70	1.47	0.75	2.77	49.22	73.5
10H-3, 39-41	82.9	ND	ND	ND	ND	58.34	ND
10H-4, 39-41	84.4	ND	ND	ND	ND	45.21	ND
10H-5, 39-41	85.8	2.98	1.68	1.02	2.01	39.22	66.8
10H-6, 39-41	87.3	ND	ND	ND	ND	41.96	ND
10H-7, 39-41	88.8	2.62	1.68	1.09	1.47	35.06	59.5
11H-1, 29-31	89.8	2.53	1.56	0.92	1.84	41.14	64.8
11H-2, 29-31	90.3	2.77	1.58	0.90	2.19	42.93	68.6
11H-3, 29-31	91.8	2.45	1.49	0.81	2.12	45.17	67.9
11H-4, 29-31	93.2	2.82	1.58	0.89	2.27	43.45	69.4
11H-5, 29-31	94.7	2.65	1.57	0.91	1.99	41.82	66.5
11H-6, 29-31	96.2	2.61	1.48	0.78	2.49	47.63	71.4
11H-7, 29-31	97.7	2.67	1.43	0.69	3.08	52.03	75.5
12H-1, 29-31	99.3	2.57	1.39	0.64	3.26	54.32	76.5
12H-2, 29-31	99.9	ND	ND	0.87	ND	53.60	ND
12H-3, 29-31	101.4	2.45	1.39	0.66	2.90	52.76	74.3
12H-4, 29-31	102.8	ND	ND	1.06	ND	48.69	ND
12H-5, 29-31	104.3	2.67	1.60	0.96	1.88	40.28	65.3
12H-6, 29-31	105.8	ND	ND	ND	ND	39.75	ND
12H-7, 29-31	107.3	ND	ND	ND	ND	37.67	ND
14H-1, 29-31	110.8	2.71	1.59	0.92	2.03	41.76	67.0
14H-2, 29-31	112.1	ND	ND	ND	ND	39.00	ND
14H-3, 29-31	113.6	2.57	1.58	0.95	1.78	39.92	64.0
14H-4, 29-31	115.1	ND	ND	ND	ND	41.66	ND
14H-5, 29-31	116.6	2.97	1.58	0.86	2.58	45.23	72.1
14H-6, 29-31	117.9	ND	ND	ND	ND	46.32	ND
14H-7, 29-31	119.3	2.40	1.60	1.02	1.41	36.19	58.5
15H-1, 29-31	120.3	2.75	1.51	0.79	2.62	47.46	72.4
15H-3, 29-31	122.6	2.57	1.47	0.77	2.48	47.76	71.2
15H-5, 29-31	125.5	2.45	1.51	0.85	1.98	43.60	66.4
15H-7, 29-31	128.5	2.44	1.51	0.87	1.90	42.80	65.5
16H-1, 29-31	129.8	2.68	1.49	0.77	2.62	48.10	72.4
16H-3, 29-31	132.1	2.39	1.44	0.75	2.32	48.06	69.9
16H-5, 29-31	135.1	2.54	1.50	0.81	2.24	45.63	69.1
16H-7, 29-31	137.9	2.28	1.41	0.73	2.25	48.47	69.2
17H-1, 29-31	139.3	2.70	1.44	0.69	3.08	51.80	75.5
17H-3, 29-31	141.2	2.53	1.67	1.10	1.34	33.84	57.2
17H-7, 29-31	147.2	2.57	1.55	0.90	1.95	42.03	66.1
18H-1, 29-31	148.8	2.44	1.58	0.98	1.56	38.20	61.0
18H-3, 29-31	150.9	2.67	1.49	0.78	2.58	47.88	72.1
18H-5, 29-31	153.7	2.35	1.43	0.74	2.29	48.11	69.6
18H-7, 29-31	156.7	2.57	1.53	0.86	2.08	43.59	67.5
19H-1, 29-31	158.3	2.39	1.54	0.93	1.65	39.95	62.3
19H-3, 29-31	160.8	2.60	1.47	0.76	2.54	52.00	71.8
19H-5, 29-31	163.8	2.45	1.52	0.87	1.91	42.77	65.6
19H-7, 29-31	166.8	2.57	1.48	0.78	2.43	47.38	70.9
20H-1, 29-31	167.8	2.49	1.63	1.05	1.44	35.76	59.0
20H-3, 29-31	170.7	2.69	1.60	0.95	1.91	40.45	65.6
20H-5, 29-31	173.7	2.43	1.46	0.78	2.23	46.63	69.0
20H-7, 29-31	176.7	2.64	1.49	0.79	2.49	47.30	71.3
21H-1, 29-31	177.3	1.81	1.32	0.72	1.59	45.81	61.3
21H-3, 29-31	179.3	2.63	1.50	0.80	2.41	46.58	70.6
21H-5, 29-31	182.3	2.38	1.41	0.71	2.51	49.97	71.5
21H-7, 29-31	185.3	2.65	1.62	0.99	1.75	38.75	63.6
22H-1, 29-31	186.8	2.29	1.49	0.87	1.71	41.69	63.0
22H-3, 29-31	187.7	2.73	1.64	1.01	1.77	38.43	64.0
22H-5, 29-31	191.2	2.47	1.50	0.83	2.07	44.53	67.4
22H-7, 29-31	194.2	2.66	1.67	1.06	1.57	36.24	61.1

Note: ND = no data.

**Table T18.** Affine table indicating the amount that each core in each hole needs to be offset in order to construct a continuous record, Site U1339. (Continued on next page.)

Core	Depth (mbsf)		Offset (m)	Depth CCSF-A (m)		Recovered (m)	Recovery (%)
	Top	Bottom		Top	Bottom		
323-U1339A-							
1H	0.00	4.94	0.36	0.36	5.30	4.94	101
2H	4.90	14.74	0.01	4.91	14.75	9.84	104
3H	14.40	24.33	1.17	15.57	25.50	9.93	105
4H	23.90	33.70	1.33	25.23	35.03	9.80	103
323-U1339B-							
1H	0.00	4.01	0.23	0.23	4.24	4.01	100
2H	4.00	13.58	0.38	4.38	13.96	9.58	101
3H	13.50	22.99	1.32	14.82	24.31	9.49	100
4H	23.00	32.73	1.55	24.55	34.28	9.73	102
5H	32.50	42.27	2.30	34.80	44.57	9.77	103
6H	42.00	51.90	2.85	44.85	54.75	9.90	104
7H	51.50	61.60	3.96	55.46	65.56	10.10	106
8H	61.00	70.95	5.52	66.52	76.47	9.95	105
9H	70.50	80.47	5.32	75.82	85.79	9.97	105
10H	80.00	89.98	8.06	88.06	98.04	9.98	105
11H	89.50	99.35	7.81	97.31	107.16	9.85	104
12H	99.00	107.78	7.58	106.58	115.36	9.48	100
13X	108.50	108.99	9.52	118.02	118.51	0.49	24
14H	110.50	120.57	9.74	120.24	130.31	10.07	106
15H	120.00	130.12	11.50	131.50	141.62	10.12	107
16H	129.50	139.51	13.01	142.51	152.52	10.01	105
17H	139.00	148.67	14.63	153.63	163.30	9.67	102
18H	148.50	158.89	16.51	165.01	175.40	10.39	109
19H	158.00	167.96	18.07	176.07	186.03	9.96	105
20H	167.50	177.74	20.32	187.82	198.06	10.24	108
21H	177.00	187.70	21.89	198.89	209.59	10.70	113
22H	186.50	196.93	22.58	209.08	219.51	10.43	110
323-U1339C-							
1H	0.00	9.78	0.00	0.00	9.78	9.78	100
2H	9.80	19.52	0.30	10.10	19.82	9.72	102
3H	19.30	29.19	1.30	20.60	30.49	9.89	104
4H	28.80	38.96	2.10	30.90	41.06	10.16	107
5H	38.30	48.49	2.75	41.05	51.24	10.19	107
6H	47.80	57.94	5.03	52.83	62.97	10.14	107
7H	57.30	66.65	6.13	63.43	72.78	9.35	98
8H	66.80	76.63	6.65	73.45	83.28	9.83	103
9H	76.30	85.34	7.58	83.88	92.92	9.04	95
10H	85.80	95.11	7.79	93.59	102.90	9.31	98
11H	95.30	104.53	8.38	103.68	112.91	9.23	97
12H	104.80	114.11	9.83	114.63	123.94	9.31	98
13H	114.30	123.81	11.26	125.56	135.07	9.51	100
14H	123.80	134.09	12.41	136.21	146.50	10.29	108
15H	133.30	142.38	14.41	147.71	156.79	9.70	102
16H	142.80	146.62	15.57	158.37	162.19	3.82	85
17H	147.30	157.13	16.18	163.48	173.31	10.31	109
18H	156.80	166.02	18.77	175.57	184.79	9.22	97
19H	166.30	176.48	18.09	184.39	194.57	10.18	107
20H	175.80	185.85	19.98	195.78	205.83	10.05	106
21H	185.30	195.34	20.08	205.38	215.42	10.04	106
323-U1339D-							
1H	0.00	6.62	0.30	0.30	6.92	6.62	100
2H	6.60	16.14	1.50	8.10	17.64	9.54	100
3H	16.10	25.69	1.68	17.78	27.37	9.59	101
4H	25.60	33.48	1.62	27.22	35.10	7.88	100
5H	33.50	43.34	2.01	35.51	45.35	9.84	104
6H	43.00	53.07	3.68	46.68	56.75	10.07	106
7H	52.50	62.58	4.70	57.20	67.28	10.08	106
8H	62.00	71.30	6.77	68.77	78.07	9.30	98
9H	71.50	80.45	6.91	78.41	87.36	8.95	94
10H	81.00	90.53	7.36	88.36	97.89	9.53	100
11H	90.50	100.48	7.60	98.10	108.08	9.98	105
12H	100.00	110.42	8.84	108.84	119.26	10.42	110
13H	109.50	119.99	11.68	121.18	131.67	10.49	110
14H	119.00	128.93	12.79	131.79	141.72	9.93	105
15H	128.50	137.24	16.89	145.39	154.13	8.74	92

Table T18 (continued).

Core	Depth (mbsf)		Offset (m)	Depth CCSF-A (m)		Recovered (m)	Recovery (%)
	Top	Bottom		Top	Bottom		
16H	138.00	147.21	18.24	156.24	165.45	9.21	97
17H	147.50	157.98	19.17	166.67	177.15	10.48	110
18H	157.00	167.28	20.76	177.76	188.04	10.28	108
19H	166.50	176.87	23.14	189.64	200.01	10.37	109
20H	176.00	186.09	25.59	201.59	211.68	10.09	106
21H	185.50	194.21	25.41	210.91	219.62	8.71	92
22H	195.00	200.83	27.03	222.03	227.86	5.83	117

Table T19. Splice table indicating tie points between holes, Site U1339. Sampling along the splice should be used to construct a continuous record.

Hole, core, section, interval (cm)	Depth		Tie to	Hole, core, section, interval (cm)	Depth	
	mbsf	CCSF-D (m)			mbsf	CCSF-D (m)
323-U1339C-1H-7, 3.5	9.04	9.04	Tie to	323-U1339D-2H-1, 93.3	7.53	9.04
U1339D-2H-6, 46.7	14.57	16.07	Tie to	U1339C-2H-4, 147.3	15.77	16.07
U1339C-2H-6, 113.4	18.43	18.73	Tie to	U1339D-3H-1, 95.1	17.05	18.73
U1339D-3H-5, 140.9	23.51	25.19	Tie to	U1339C-3H-4, 8.4	23.88	25.19
U1339C-3H-6, 91.1	27.71	29.02	Tie to	U1339D-4H-2, 29.3	27.39	29.02
U1339D-4H-5, 74.3	32.34	33.97	Tie to	U1339C-4H-3, 6.4	31.86	33.97
U1339C-4H-6, 115.8	37.46	39.56	Tie to	U1339D-5H-3, 104.6	37.55	39.56
U1339D-5H-6, 134.5	42.34	44.36	Tie to	U1339C-5H-3, 31.3	41.61	44.36
U1339C-5H-7, 49.0	47.79	50.54	Tie to	U1339D-6H-3, 85.2	46.85	50.54
U1339D-6H-7, 7.4	52.07	55.76	Tie to	U1339C-6H-3, 99.3	50.73	55.76
U1339C-6H-7, 88.7	56.63	61.65	Tie to	U1339D-7H-3, 145.1	56.95	61.65
U1339D-7H-6, 107.1	61.07	65.77	Tie to	U1339C-7H-2, 84.5	59.65	65.77
U1339C-7H-6, 37.8	65.18	71.30	Tie to	U1339D-8H-2, 106.6	64.54	71.30
U1339D-8H-6, 25.5	69.73	76.49	Tie to	U1339C-8H-3, 4.1	69.84	76.49
U1339C-8H-5, 81.1	73.61	80.26	Tie to	U1339D-9H-2, 35.6	73.36	80.26
U1339D-9H-5, 4.7	77.55	84.45	Tie to	U1339C-9H-1, 57.6	76.88	84.45
U1339C-9H-6, 48.8	84.07	91.65	Tie to	U1339D-10H-3, 28.2	84.28	91.65
U1339D-10H-6, 92.0	89.42	96.78	Tie to	U1339C-10H-3, 119.6	89.00	96.78
U1339C-10H-5, 133.2	92.00	99.79	Tie to	U1339D-11H-2, 141.8	92.19	99.79
U1339D-11H-7, 61.5	98.61	106.21	Tie to	U1339C-11H-2, 103.3	97.83	106.21
U1339C-11H-5, 41.8	101.66	110.03	Tie to	U1339D-12H-2, 79.2	101.19	110.03
U1339D-12H-6, 93.6	107.22	116.06	Tie to	U1339C-12H-1, 142.9	106.23	116.06
U1339C-12H-5, 138.7	112.11	121.94	Tie to	U1339D-13H-1, 75.6	110.26	121.94
U1339D-13H-7, 60.9	118.21	129.89	Tie to	U1339C-13H-4, 4.1	118.63	129.89
U1339C-13H-6, 5.1	121.64	132.90	Tie to	U1339D-14H-2, 74.8	120.11	132.90
U1339D-14H-7, 49.1	127.30	140.09	Tie to	U1339C-14H-4, 4.8	127.68	140.09
U1339C-14H-6, 147.1	132.07	144.49	Tie to	U1339B-16H-2, 116.0	131.48	144.49
U1339B-16H-6, 131.4	137.45	150.46	Tie to	U1339C-15H-2, 124.6	136.05	150.46
U1339C-15H-6, 54.5	141.30	155.72	Tie to	U1339B-17H-3, 18.6	141.09	155.72
U1339B-17H-6, 62.3	146.02	160.66	Tie to	U1339D-16H-3, 145.6	142.42	160.66
U1339D-16H-6, 92.6	146.39	164.63	Tie to	U1339C-17H-2, 3.9	148.45	164.63
U1339C-17H-6, 146.2	155.70	171.88	Tie to	U1339D-17H-4, 146.9	152.71	171.88
U1339D-17H-7, 100.8	156.75	175.92	Tie to	U1339C-18H-2, 3.4	157.14	175.92
U1339C-18H-7, 58.1	165.08	183.85	Tie to	U1339D-18H-5, 63.0	163.09	183.85
U1339D-18H-7, 38.1	165.84	186.61	Tie to	U1339C-19H-3, 50.2	168.51	186.61
U1339C-19H-5, 126.1	172.21	190.30	Tie to	U1339D-19H-2, 4.3	167.16	190.30
U1339D-19H-7, 4.4	174.63	197.78	Tie to	U1339C-20H-2, 49.4	177.79	197.78
U1339C-20H-6, 125.2	184.51	204.49	Tie to	U1339D-20H-3, 73.2	178.90	204.49
U1339D-20H-6, 27.1	182.90	208.49	Tie to	U1339C-21H-3, 11.2	188.41	208.49
U1339C-21H-6, 111.3	193.91	213.99	Tie to	U1339D-21H-3, 10.0	188.58	213.99
U1339D-21H-6, 65.0	193.63	219.04	Extrapolate	U1339D-22H-1, 0.0	195.00	222.03

Table T20. Temperature data, Site U1339. (See table note.)

Core	Depth (mbsf)	$T$ (°C)	$T_s$ (°C)	Remarks
323-U1339A-3H	23.9	NA	2.10	Excessive tool movement, unusable
323-U1339B-3H	23.0	3.65	2.10	Moderate sea
8H	70.5	6.95	2.10	Moderate sea
13H	110.5	9.19	2.10	Moderate sea, unstable decay
18H	158.0	12.83	2.10	Moderate sea

Note:  $T$  = formation temperature,  $T_s$  = seafloor temperature, NA = not applicable.